

**PHASE-FIELD MODELLING OF ABNORMAL GRAIN GROWTH**

by

Ying Liu

B.A.Sc., University of Science and Technology Beijing, 2014

A THESIS SUBMITTED IN PARTIAL FULFILLMENT OF  
THE REQUIREMENTS FOR THE DEGREE OF

MASTER OF APPLIED SCIENCE

in

THE FACULTY OF GRADUATE AND POSTDOCTORAL STUDIES  
(Materials Engineering)

THE UNIVERSITY OF BRITISH COLUMBIA  
(Vancouver)

August 2017

© Ying Liu, 2017

## Abstract

Heterogeneous grain structures may develop due to abnormal grain growth during thermo-mechanical processing of polycrystalline materials ranging from metals to ceramics. This phenomenon must be controlled in practical applications where typically homogeneous grain structures are desired. Recent advances in experimental and computational techniques have, thus, stimulated to revisit the underlying growth mechanisms. Here, phase field modelling is used to systematically evaluate conditions for abnormal grain growth. Grain boundaries are classified into two classes, i.e. high and low mobility boundaries. Three different approaches are considered for having high and low mobility boundaries:

- (i) Critical threshold angle of grain boundary disorientation above which boundaries are highly mobile;
- (ii) Two grain types A and B with either the AB or the AA boundaries being highly mobile;
- (iii) Three grain types A, B and C with AB boundaries being highly mobile.

For these different scenarios, 2D and 3D simulations have been performed to quantify the effect of variations in the mobility ratio, threshold angle and fractions of grain types, respectively, on the potential onset of abnormal grain growth and the degree of heterogeneity in the resulting grain structures. The required mobility ratios to observe abnormal grain growth are quantified as a function of the fraction of high mobility boundaries. The microstructure evolutions during abnormal grain growth are analyzed in terms of the spatial distribution of the highly mobile boundaries.

## **Lay summary**

Many engineering materials (e.g. metals, alloys, ceramics) are polycrystalline, i.e. they consist of many grains where each grain is characterized by a crystallographic orientation. Grains are separated by grain boundaries and different boundaries may have different properties. The grain size critically determines the material properties (e.g. refining the grain size increases the strength). The grain size can be controlled by thermo-mechanical processing (e.g. heat treatment). For instance, grain growth occurs at high temperatures where grain boundaries are mobile. As there are different grain boundaries the mobility of selected boundaries may be higher than that of other boundaries which can result into a phenomenon called abnormal grain growth where a few grains grow rapidly resulting in a heterogeneous grain structure consisting of a few very large and many much smaller grains. Here, computational simulations are conducted to determine conditions where abnormal grain growth can occur (e.g. required magnitude of mobility advantages).

## **Preface**

This simulation work was conducted at the University of British Columbia within the Department of Materials Engineering. I conducted the phase-field simulations using MICRESS and analyzed the output data. The Monte Carlo simulation input data in Chapter 5 has been provided by Dr. Brian DeCost, a postdoctoral researcher in Prof. Liz Holm's group in the Materials Science and Engineering Department at Carnegie Mellon University. Throughout the program, Dr. Matthias Miltzer provided great guidance and support on research direction and manuscript writing.

# Table of Contents

<b>Abstract.....</b>	<b>ii</b>
<b>Lay summary.....</b>	<b>iii</b>
<b>Preface.....</b>	<b>iv</b>
<b>Table of Contents .....</b>	<b>v</b>
<b>List of Figures.....</b>	<b>viii</b>
<b>List of Symbols .....</b>	<b>xiv</b>
<b>List of Abbreviations .....</b>	<b>xvii</b>
<b>Acknowledgements .....</b>	<b>xviii</b>
<b>Chapter 1: Introduction .....</b>	<b>1</b>
<b>Chapter 2: Literature review .....</b>	<b>3</b>
2.1    Experimental observation .....	3
2.1.1    Abnormal grain growth in electrical steels .....	3
2.1.2    Abnormal grain growth in other metallic systems .....	6
2.1.3    Abnormal grain growth in ceramics .....	12
2.2    Theory of abnormal grain growth .....	15
2.3    Computational simulation methods .....	22
2.3.1    Phase field modelling.....	22
2.3.2    Monte Carlo simulation .....	27
2.4    Summary.....	35
<b>Chapter 3: Scope and objectives.....</b>	<b>36</b>
<b>Chapter 4: Methodology.....</b>	<b>37</b>

4.1	Multi-phase field model .....	37
4.2	Simulation approaches .....	39
4.2.1	General simulation setup.....	39
4.2.2	Critical disorientation angle .....	40
4.2.3	Texture components.....	43
4.3	Sensitivity analysis.....	51
4.3.1	Normal grain growth.....	51
4.3.2	Sensitivity analysis of time step.....	53
4.3.3	Sensitivity analysis of anisotropic structure .....	54
4.4	Post data processing.....	56
<b>Chapter 5: Results and discussion.....</b>		<b>57</b>
5.1	Mobility advantages through critical disorientation angle.....	57
5.2	Mobility advantages in two grain type systems .....	65
5.2.1	Fast A-A boundaries .....	65
5.2.2	Fast A-B boundaries .....	69
5.3	Mobility advantages in three grain type systems .....	76
5.4	Comparison with Monte Carlo simulation.....	80
<b>Chapter 6: Conclusions and future work .....</b>		<b>83</b>
<b>Bibliography .....</b>		<b>86</b>
<b>Appendices.....</b>		<b>92</b>
Appendix A.....		92
A.1	Input script of threshold angle approach.....	92
A.2	Input script of two texture components approach with A-A boundary fast.....	97

A.3	Input script of two texture components approach with A-B boundary fast .....	104
A.4	Input script of three texture component approach .....	111
Appendix B .....		119
B.1	Sensitivity analysis of minimal distance between grains.....	119
B.2	Sensitivity analysis of radius distribution range .....	121
B.3	Sensitivity of the radius ratio $r_A$ vs. $r_B$ .....	123
B.4	Sensitivity analysis of initial structure .....	124

## List of Figures

Figure 2.1 EBSD imaging showing grain structure in a sheet-section heating up to 875°C while the secondary recrystallization is about to start (Gray grain is Goss grain). [2] .....	3
Figure 2.2 EBSD microstructure (a) and the internal particle distribution (b) of the sample annealed at 875°C [4].....	4
Figure 2.3 Disorientation angle distribution around Goss grains (880 boundaries, in black) and around primary matrix grains (in white) [7] .....	5
Figure 2.4 Evolution of the austenite grain structure during AGG in an A36 steel at 1000°C. [12] .....	7
Figure 2.5 (a) The optical microstructure of 316L stainless steel specimens heat-treated at 1100°C for 60min; (b) TEM micrograph of grain boundaries. [13] .....	7
Figure 2.6 (a) The optical microstructure of 316L stainless steel specimens heat-treated at 1300°C for 15min; (b) TEM micrograph of grain boundaries. [13] .....	8
Figure 2.7 (a) The optical microstructure of the carburized Ni specimen annealed at 0.55 $T_m$ for 90 min [14]; (b) the TEM microstructure of a faceted grain boundary [14]; (c) the intergranular fracture surface of the specimen heat-treated at 1200°C and (d) at 1300°C for 2h at a high magnification [15].....	9
Figure 2.8 EBSD maps of (a) the initial microstructure and of samples held at 1050°C for 75s (b) full maps (b2) with threshold. [18] .....	11
Figure 2.9 Microstructure stability map of F357 alloy. [17] .....	12
Figure 2.10 (a) A grain boundary from calcia doped alumina containing a 0.6nm intergranular film; (b) a basal plane grain boundary on an abnormal grain with no film. [19] .....	13

Figure 2.11 (a) SEM micrograph (b) grain size distribution after heat treatment at 1800°C of materials containing 3% nuclei. [23] .....	14
Figure 2.12 (a) Microstructure (b) SEM micrograph showing abnormal grains in 0.1 mol% TiO <sub>2</sub> -excess BaTiO <sub>3</sub> sintered at 1250°C for 10h in air. [24] .....	15
Figure 2.13 Relation between average grain size and grain growth process [29] .....	16
Figure 2.14 Rate of inhibition drop and mean radius growth [30] .....	18
Figure 2.15 Grain boundary velocity under the solute drag effect as a function of driving force. (a) Theoretical model; (b) simplified model. [28] .....	20
Figure 2.16 Mechanism map for abnormal grain growth. [32].....	21
Figure 2.17 Improved mechanism map for AGG. [33] .....	22
Figure 2.18 Microstructure evolution of the selected grains in the 2D structure. [41].....	24
Figure 2.19 PFM of grain growth containing second-phase particles at different time steps. (a) 200, (b) 3000 and (c) 30,000 [42].....	25
Figure 2.20 PFM of grain growth with pinning pressure at time of (a) 200, (b) 2000 and (c) 20,000. [46].....	26
Figure 2.21 Microstructure evolution of the polycrystalline system with 5000 particles. [47]....	27
Figure 2.22 An example grain structure represented by a 2D square matrix. [48].....	28
Figure 2.23 (a) Initial microstructure from an experimental result; (b) Evolution of the microstructure after 400MCS when the pinning force for Goss grains is four times smaller than for matrix grains. [49] .....	29
Figure 2.24 A 2D cross-section of a 3D microstructure after 9000 MCS showing irregular shape of the abnormal grain. [50] .....	30

Figure 2.25 Microstructure evolution of (a) a single abnormal grain with $M = 7.5$ [52]; (b) multi abnormal grains with $M = 10$ [53].	31
Figure 2.26 Relative grain radius $\rho$ as a function of time for (a) different $M$ values and (b) different initial $\rho$ values. [52]	32
Figure 2.27 Microstructures of AGG simulations with fractions of type II grains $f_{II} = 0$ (first row), 0.2 (second row), 0.4 (third row), 0.7 (fourth row), and 1.0 (fifth row). [55]	34
Figure 4.1 A polycrystalline structure defined by a set of order parameters, $\phi_i$ , associated with each grain. [60]	38
Figure 4.2 The disorientation angle distribution of the initial microstructure.	41
Figure 4.3 Boundary mobility $\mu$ as a function of disorientation angle in the threshold angle $\theta_C$ approach.	42
Figure 4.4 The initial microstructure of (a) 2D simulation and (b) 3D simulation of the threshold angle approach.	43
Figure 4.5 The initial microstructure of $A\% = 20\%$ with fast A-A grain boundaries, before adjustment, $r_A = r_B = 25.0 \mu\text{m}$ .	45
Figure 4.6 The initial microstructure with 20% A grains after adjustment ( $r_A = 29.28 \mu\text{m}$ and $r_B = 24.0 \mu\text{m}$ ). (a) Before a small time step annealing; (b) after a small time step annealing.	46
Figure 4.7 The initial microstructure of 2% B grains in A grains matrix before adjustment, $r_A = r_B = 25.0 \mu\text{m}$ .	47
Figure 4.8 The initial microstructure of 2 % B grains in A grains matrix after adjustment ( $r_A = 20.0 \mu\text{m}$ and $r_B = 26.6 \mu\text{m}$ ). (a) Before a small time step annealing; (b) after a small time step annealing.	48

Figure 4.9 The initial microstructure of 1% B grains in A, C grains matrix (A% = C% = 49.5%)	49
Figure 4.10 The initial microstructure of one B grain in the matrix of A,C grains (A % = C % = 49.5 %)	50
Figure 4.11 The 3D initial microstructure of the two texture components system	51
Figure 4.12 Evolution of $R^2$ for shrinkage of one single grain.	52
Figure 4.13 Ideal grain growth in a multi-grain structure: (a) Evolution of $\bar{R}^2$ ; (b) Grain size distribution at different simulation times.	53
Figure 4.14 Time evolution of $\bar{R}^2$ using automatic time step and fixed time step of 0.02s.	54
Figure 4.15 The time evolution of $\bar{R}^2$ for grain structure (a) with and without crystallographic orientations; (b) with and without texture components; (c) grain size distribution at 2000s with and without texture components.	55
Figure 5.1 Evolution of 2D grain structure for $\mu_2/\mu_1 = 1000$ and $\theta_C = 40^\circ$ , highlighted fast boundaries from slow boundaries.	58
Figure 5.2 Time evolution of cumulative grain area distribution. ( $\mu_2/\mu_1 = 1000$ and $\theta_C = 40^\circ$ ).	59
Figure 5.3 (a) Cumulative grain area distribution and (b-d) grain structures for the widest grain size distributions for different initial structures when $\theta_C = 40^\circ$ and $\mu_2/\mu_1 = 1000$ .	60
Figure 5.4 Cumulative grain area distribution for the widest grain size distributions: (a) Effect of threshold angle when $\mu_2/\mu_1 = 100$ ; (b) Effect of mobility ratio when $\theta_C = 40^\circ$ ...	62
Figure 5.5 2D grain structure for the widest grain size distribution when $\theta_C = 40^\circ$ and (a) $\mu_2/\mu_1 = 10$ ; (b) $\mu_2/\mu_1 = 100$ ; (c) $\mu_2/\mu_1 = 1000$ .	63

Figure 5.6 The 3D grain structure (a) and the cross section (b) when  $\mu_2/\mu_1 = 1000$  and  $\theta_C = 45^\circ$ .  
The 3D grain structure (c) and the cross section (d) when  $\mu_2/\mu_1 = 10$  and  $\theta_C = 45^\circ$ .  
..... 64

Figure 5.7 Time evolution of cumulative grain area distribution for 3D simulations setting  $\theta_C = 45^\circ$ : (a)  $\mu_2/\mu_1 = 1000$ ; (b)  $\mu_2/\mu_1 = 10$ ..... 64

Figure 5.8 Microstructure evolution of A-B system with fast A-A boundaries when  $\mu_2/\mu_1 = 100$  and 50% A grains in the initial structure. .... 66

Figure 5.9 Time evolution of cumulative grain area distribution in the A-B system with fast A-A boundaries..... 67

Figure 5.10 Widest area distribution curves in A-B system to investigate the influence of initial A grain percentage when  $\mu_2/\mu_1 = 100$ . .... 67

Figure 5.11 The 3D cubic structure (a) and the cross section images (b) when initial A% = 50% and  $\mu_2/\mu_1 = 100$ ..... 68

Figure 5.12 Time evolution of cumulative grain volume distribution with fast A-A boundaries. 68

Figure 5.13 Microstructure evolution of A-B system with fast A-B boundaries when  $\mu_2/\mu_1 = 1000$  and 0.67% growing B grains in the initial structure. .... 70

Figure 5.14 Time evolution of cumulative grain area distribution in the A-B system ( $\mu_2/\mu_1 = 1000$ , growing B=0.67%)..... 72

Figure 5.15 Widest area distribution curves in the A-B system to study the effect of mobility ratio when growing B % = 0.44 % ..... 73

Figure 5.16 Microstructure of the most abnormal position of (a) growing B % = 0.67 %; (b) growing B % = 1.5 % when  $\mu_2/\mu_1 = 1000$ . (c) Widest area distribution curves in A-B system to study the effect of growing B grain percentage when  $\mu_2/\mu_1 = 1000$ .. 74

Figure 5.17 The 3D grain structure (a) and the cross section (b) when growing B% = 1% and $\mu_2/\mu_1 = 1000$ .	75
Figure 5.18 Widest volume distribution curves of 3D A-B systems to investigate the influence of growing B grain percentage when $\mu_2/\mu_1 = 1000$ .	75
Figure 5.19 Typical grain structure in a three grain type system with an initial composition of B% = 1%, A% = C% = 49.5% and a mobility ratio of 1000.	77
Figure 5.20 Structure of rapidly growing B grain in three grain type systems with a mobility ratio of 1000 when (a) A=30%; (b) A=50%; (c) A=70%; (d) A=90%.	78
Figure 5.21 The rapidly growing B grain starting from different initial structure with a mobility ratio of 1000 when (a,b) A=50%, t = 135 s; (c,d) A=70%, t = 108 s.	79
Figure 5.22 Comparison between PFM and MC model. Both simulations start from the same initial microstructure.	81
Figure 5.23 Comparison of the size evolution of the abnormal grain obtained in PFM and MC simulations.	82

## List of Symbols

$d$	Average diameter of second-phase particles
$d_A$	Distance between two A grains
$d_B$	Distance between two B grains
$d_C$	Distance between two C grains
$\bar{D}$	Average diameter of normal matrix grains
$\bar{D}_{ab}$	Average diameter of abnormal grain
$\bar{D}_{Lim}$	Limiting grain diameter
$F$	Helmholtz free energy
$f$	Volume fraction of second-phase particles
$f_{II}$	Fraction of type II grains
$G_f$	Free energy of new element f
$G_i$	Free energy of element i
$\Delta G_{ij}$	External driving pressure of grain growth
$I_z$	Inhibition factor of particle pinning
$k$	Grain growth constant for parabolic rule
$L$	Kinetic coefficient
$M$	Grain boundary mobility ratio
$Q_f$	Crystallographic orientation of new element f
$Q_i$	Crystallographic orientation of element i
$r$	Average radius of second-phase particles

$r_A$	Radius of A grains
$r_{A,max}$	Maximum grain radius of A grains
$r_{A,min}$	Minimum grain radius of A grains
$r_B$	Radius of B grains
$r_{B,max}$	Maximum grain radius of B grains
$r_{B,min}$	Minimum grain radius of B grains
$r_C$	Radius of C grains
$r_{max}$	Minimum grain radius value
$r_{min}$	Maximum grain radius value
$R$	Average grain radius
$R_0$	Initial grain radius
$R_{ab}$	Radius of abnormal grain
$R_{Cr}$	Critical grain radius in Hillert's theory
$\bar{R}$	Mean equivalent radius
$t$	Time
$T$	Temperature
$T_m$	Melting temperature
$X$	Grain size ratio
$X_{max}$	Maximum size ratio once grain growth is complete
$X_{min}$	Size ratio of the smallest grain that can grow abnormally
$z$	Pinning parameter

$Z$	Pinning force
$\alpha$	Geometric factor
$\beta$	A constant for inhibition factor
$\kappa$	A constant parameter to match phase field time and Monte Carlo step
$\mu$	Grain boundary mobility
$\mu_{ij}$	Grain boundary mobility between grain i and grain j
$\mu_2$	High grain boundary mobility value
$\mu_1$	Low grain boundary mobility value
$\gamma$	Grain boundary energy per unit of area
$\rho$	Relative grain radius
$\eta$	Grain boundary thickness
$\theta$	Misorientation angle
$\theta_C$	Critical misorientation angle or threshold angle
$\sigma$	Grain boundary energy
$\sigma_{AA}$	Grain boundary energy between two adjacent A grains
$\sigma_{AB}$	Grain boundary energy between A grains and B grains
$\sigma_{BB}$	Grain boundary energy between two adjacent B grains
$\sigma_{ij}$	Grain boundary energy between grain i and grain j
$\phi_i$	Order parameters of grain i
$\phi_j$	Order parameters of grain j

## List of Abbreviations

AGG	Abnormal grain growth
CF	Continuum-field
CSL	Coincidence site lattice
EBSD	Electron backscatter diffraction
EQAD	Equivalent area diameter
FSP	Friction stir processed
GB	Grain boundary
HE	High energy
MC	Monte Carlo
MCPM	Monte Carlo Potts Model
MCS	Monte Carlo step
MICRESS	Microstructure evolution simulation software
MPF	Multi-phase-field
MPFM	Multi-phase field model
NGG	Normal grain growth
PFM	Phase field model
PFT	Phase field time
SEM	Scanning electron microscopy
TEM	Transmission electron microscopy

## **Acknowledgements**

First and foremost, I owe my sincere gratitude to Dr. Matthias Militzer, for guidance, support, and understanding throughout the study. Thank you for giving me the chance to work in this project. It is a great honor and pleasure to be a student of yours.

Many thanks to members of microstructure group of the Department of Materials Engineering. I am very grateful to Dr. Benqiang Zhu for his expertise and willingness to tutor me on the use of MICRESS. I also appreciate Mr. Jingqi Chen for his guidance on the use of TSL OIM Analysis software. I would like thank Dr. Thomas Garcin and Mr. Brian Tran for their advice and support.

I have benefited a lot from the discussion with Dr. Michel Perez in France that promoted this project a further.

Special thanks are owed to my parents for their constant encouragement and love. I also want to thank my friends in Regent College, especially Jennifer, Joyce, Peter and Luke. Without you I would not have gone this far.

Lastly, I would like to thank the Natural Sciences and Engineering Research Council of Canada for their financial support of my research.

## Chapter 1: Introduction

Grain growth refers to an increase in the size of grains in polycrystalline materials during heat treatment. It occurs to lower the free energy by reducing the grain boundary area and thus grain boundary energy per unit volume. The grain structure and grain size of a polycrystalline material critically affect its mechanical properties, such as strength, toughness, hardness etc. For instance, in metals and ceramics, finer grains will result in high strength and toughness. Besides, the orientations of the grains will strongly influence the electrical and magnetic properties as well. In electrical steels, grains with  $\{110\}\langle 001\rangle$  orientation in the shear plane will reduce the hysteresis loss significantly. Those physical properties in turn govern the applications of these materials. Therefore, grain growth processes have to be carefully controlled.

Grain growth can be classified into two categories. The first type is normal grain growth (NGG) which is a self-similar coarsening process. NGG occurs in a uniform manner and most grains are equiaxial in shape. The second one is abnormal grain growth (AGG) resulting in fast grain growth stages when only a few grains (abnormal grains) grow rapidly within a matrix of fine grains. An abnormal grain has a significant size advantage over the matrix grains, leading to a bimodal grain size distribution, the size of the abnormal grain as least to be 5 times larger than the average grain size. In addition, the abnormal grain often has a complex shape, sometimes even including island grains. In many aspects, AGG is often undesired since it may lead to heterogeneous microstructures with adverse effects on properties, e.g. in heat treatment of superalloys. However, sometimes AGG is preferred to promote selective grain growth, e.g. development of Goss or cube texture in electrical steels. Therefore, to investigate the reasons and mechanisms for AGG is of

great importance. Many studies have been done to explore the reasons for AGG. While there are in detail different mechanisms of AGG, they all are associated with mobility advantages of selective grain boundaries. These mobility advantages may be caused by many factors, such as particle pinning, solute segregation, phase transformation etc.

Recently with the development of computer technology, many numerical models have been built to simulate microstructure evolution processes, including the phase field model (PFM) and Monte Carlo Potts model (MCPM). One of the most prominent advantages of computer simulations is their ability for systematic parameter studies. The phase field method is a versatile modelling technique and especially suitable for grain growth simulations with the evolution of complex grain shapes like in AGG. Different from sharp interface models like MCPM, PFM utilizes a continuum field and there is no need to track the position of interfaces explicitly. However, each method has its merits and demerits. In most cases, MCPM is much more time efficient than PFM. In this research, PFM is chosen to study the influence of mobility advantages during grain growth.

This thesis is divided into six chapters. The general introduction in Chapter 1 is followed by Chapter 2 where the current state of knowledge about AGG is reviewed, including experimental observations, theories and computer simulation results. Chapter 3 covers the objectives of this research while Chapter 4 describes the simulation methodology. Chapter 5 deals with the simulation results after introducing mobility advantages through different approaches, as well as the comparison between PFM and MCPM. In addition, both 2D and 3D simulations are discussed in Chapter 5. Lastly, Chapter 6 provides conclusions and suggestions for future work.

## Chapter 2: Literature review

### 2.1 Experimental observation

#### 2.1.1 Abnormal grain growth in electrical steels

The magnetic properties of electrical steel are related to the texture, and large grains with desired crystallographic orientation, such as  $\{110\}\langle 001\rangle$ , will decrease the hysteresis loss. [1] AGG can be used to promote the formation of large grains with the preferred  $\{110\}\langle 001\rangle$  orientation, also called Goss grains, in electrical steels. One example of a Goss grain is shown as the gray grain in Fig. 2.1. Sometimes the size of Goss grains can even reach several millimetres. [2] However, the reasons causing AGG in electrical steels are still under debate.

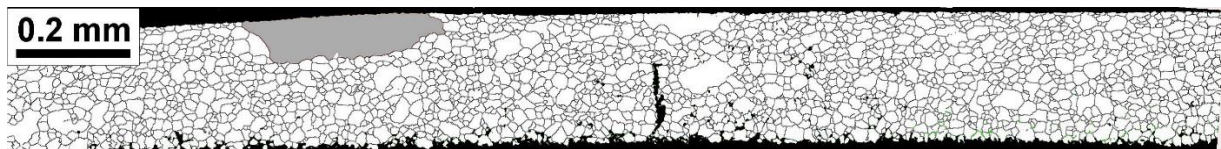


**Figure 2.1** EBSD imaging showing grain structure in a sheet-section heating up to 875°C while the secondary recrystallization is about to start (Gray grain is Goss grain). [2]

Mao et al. [2-4] state that AGG in electrical steels is caused and further enhanced by different precipitate densities. As shown in Fig 2.2(a), initially the Goss grain does not have an obvious size advantage, but eventually it grows abnormally. If comparing the precipitate density within the Goss grain and within its neighboring grains, as indicated in Fig 2.2(b), one can find that the precipitate density in the Goss grain is much higher than that in its neighbors. The grain boundary is much more mobile in the direction with lower particle density, since the boundary migration will experience less pinning effect. Therefore, with a higher particle density, the Goss grain can hardly be consumed even by an otherwise larger neighboring grain. In the early stage of AGG

which is also known as secondary recrystallization, the Goss grain will firstly consume some smaller neighboring grains and thereby increase its size. As the Goss grain keeps growing, its precipitate density is gradually decreasing. When its grain sizes is large enough, the effect of grain size advantages becomes dominant rather than particle density. The Goss grains will then reversely consume the initially larger neighboring grains.

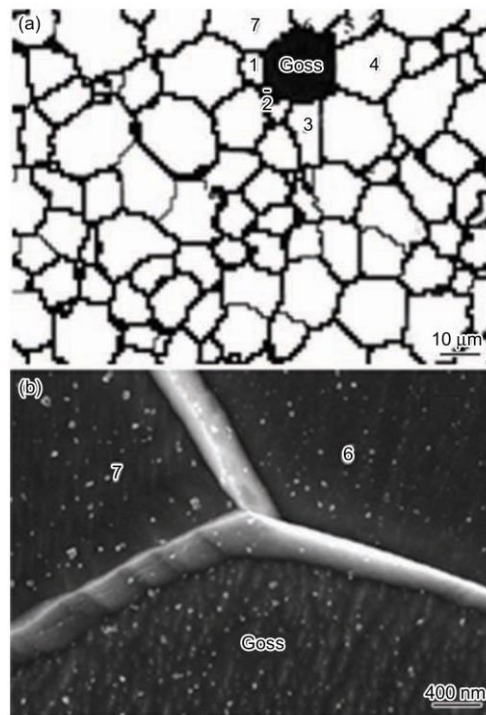


**Figure 2.2** EBSD microstructure (a) and the internal particle distribution (b) of the sample annealed at 875°C [4]

Other studies [5-7] emphasize the crucial role of high energy (HE) boundaries, i.e. grain boundaries which have disorientation between  $\sim 20^\circ$  and  $\sim 45^\circ$ , for AGG. It has been found that the average growth rate of precipitates located at HE boundaries is faster than that of the precipitates located at low energy grain boundaries. [6] When the precipitates on the HE boundaries coarsen to some critical size, it will reduce grain boundary pinning by precipitates sufficiently for migration

of the grain boundary to occur. Thus, at the early stage of annealing, only the HE boundaries can move and the others cannot. Since the Goss grains are surrounded by a large number of HE boundaries, as indicated in Fig. 2.3, therefore it is easier for the Goss grains to grow faster and gain prominent size advantages.

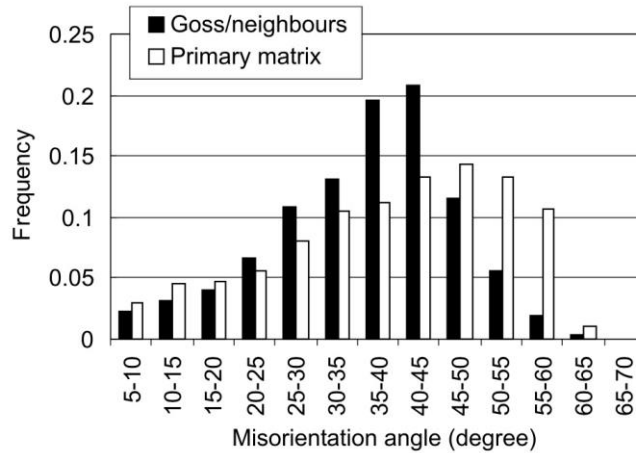


**Figure 2.3** Disorientation angle distribution around Goss grains (880 boundaries, in black) and around primary matrix grains (in white) [7]

Another possible explanation of AGG is due to the presence of coincidence site lattice (CSL) boundaries. It is argued that CSL boundaries have higher mobility than other grain boundaries and are responsible for AGG. [5-7] Harase et al. [8] found that among various CSL boundaries,  $\Sigma 9$  is crucial for the development of the  $\{110\}\langle 001\rangle$  texture. It has been found that the  $\Sigma 5$  ( $36.86^\circ$ ),  $\Sigma 7$  ( $38.21^\circ$ ), and  $\Sigma 9$  ( $38.94^\circ$ ) boundaries are especially mobile in the presence of precipitates [5-6]. The boundaries of Goss grains are more frequently CSL boundaries than for other grains, therefore they are more likely to grow abnormally. However, recently some studies [7,9] have indicated that the role of CSL boundary should be treated with skepticism.

In addition to the above, there are some other hypotheses to explain AGG phenomenon in electrical steels. One involves the formation of colonies, which will coalesce into one large Goss grain during annealing. [10] Further, solid-state wetting was found to change the interfacial energy, and, therefore, may lead to AGG. [11] All the mentioned hypotheses may account for AGG but are still open to further discussion.

### **2.1.2 Abnormal grain growth in other metallic systems**

Besides electrical steels, AGG has been observed in other metallic systems such as low carbon steels [12], stainless steels [13], Nickel and Ni-based superalloys [14-15], Al alloys [16-18] etc. In an Al-killed A36 low-carbon steel containing 0.17 wt% carbon abnormal austenite grain growth has been observed during holding at 1000 °C. [12] Micrographs for holding times of 10s, 120s, and 600s at 1000 °C are presented in Fig. 2.4 to illustrate AGG. [12] After 10s as shown in Fig. 2.4(a), uniform fine grains are observed while after 600s uniform coarse grains are found in Fig. 2.4(c). When the sample was isothermally held for 120s, a combination of fine and coarse grains are observed as shown in Fig. 2.4(b). This AGG is caused by the dissolution of AlN precipitates. [12] Initially, because of the presence of AlN precipitates, the grain growth is strongly pinned thus most grains have a fine grains size. Gradually, as dissolution of precipitates occurs, part of the grain boundaries become unpinned and these unpinned grain boundaries can move much faster than the pinned grain boundaries. As a results, some grains can grow rapidly leading to AGG with a non-homogeneous microstructure and a bimodal grain size distribution. Finally, most of the AlN precipitates are dissolved and NGG of the coarse grains proceeds essentially unpinned.

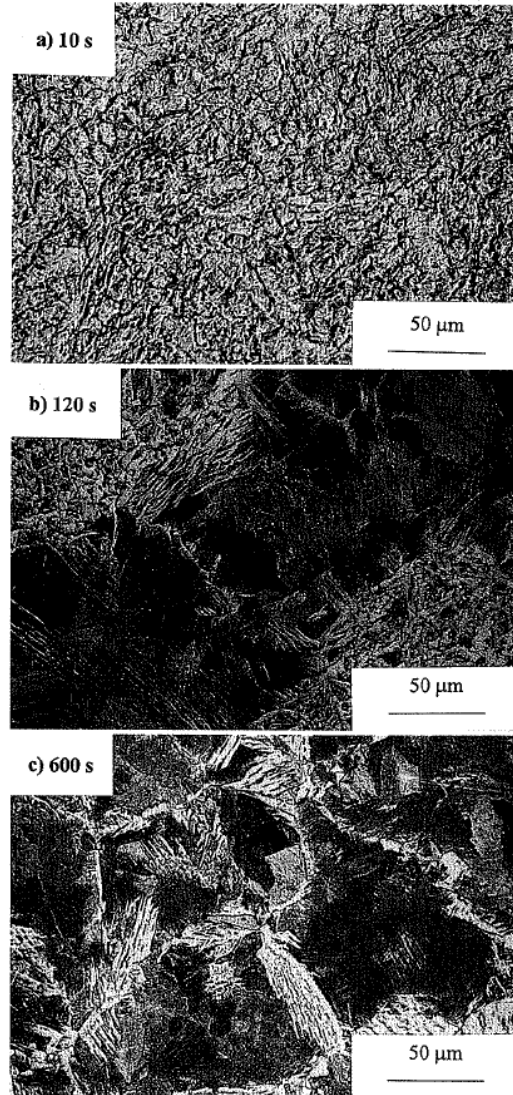


**Figure 2.4** Evolution of the austenite grain structure during AGG in an A36 steel at 1000°C. [12]

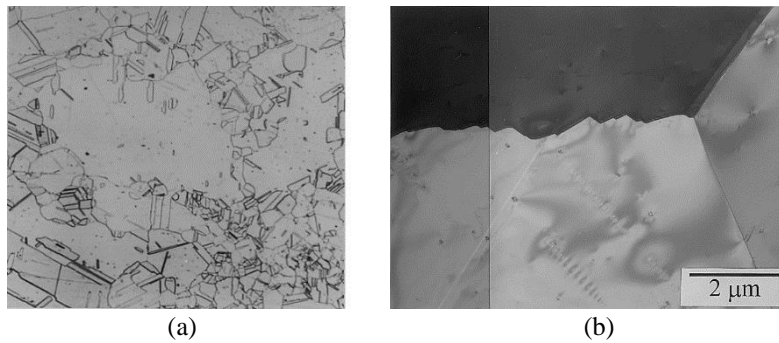


**Figure 2.5** (a) The optical microstructure of 316L stainless steel specimens heat-treated at 1100°C for 60min; (b) TEM micrograph of grain boundaries. [13]

Some scientists [13-15] put forward a possible mechanism for linking the AGG behavior to the grain boundary structure. Choi et al. [13] observed a prominent AGG phenomenon when 316L stainless steels were heat treated at 1100°C for 60min, as shown in Fig. 2.5(a). When looking at the grain boundary structure through transmission electron microscopy (TEM), 6 out of 30 boundaries [13] showed faceted structure with hills and valleys, as illustrated in Fig. 2.5(b). However, if the heat treatment temperature is increased to 1300°C, NGG will replace AGG. After heat treatment for 15min at 1300°C, the optical microstructure and the grain boundary structure is presented in Fig. 2.6 (a) and (b), respectively. The faceted structure disappeared and the grain boundaries are smoothly curved, as presented in Fig. 2.6(b). The results also show that grain growth pattern is temperature-related. A defaceting of grain boundaries will occur as the temperature increases, changing the growth mode from AGG to NGG.

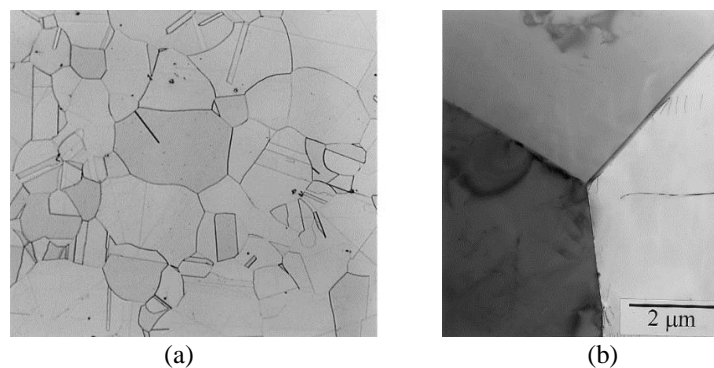


**Figure 2.6** (a) The optical microstructure of 316L stainless steel specimens heat-treated at 1300°C for 15min; (b) TEM micrograph of grain boundaries. [13]

Similar faceted boundaries have also been found in Nickel [14] and Ni-based superalloys [15]. For example, AGG was observed in commercial grade Ni (Ni 270) with 99.97 wt pct purity and without any texture. [14] After the Ni specimens were annealed at  $0.55T_m$  (677°C) for 90 min in a

carburizing atmosphere, a large grain exceeding 1000  $\mu\text{m}$  is surrounded by small matrix grains, as shown in Fig. 2.7(a). In the specimen showing AGG, all or a fraction of the grain boundaries show a faceted structure as illustrated in Fig. 2.7(b). In a Ni-based superalloy with a composition of Ni-24Co-4Al-4Ti-5Cr-5Mo (by wt%) [15], a faceted grain structure is observed when AGG occurs at 1200°C, as shown in Fig. 2.7(c). When the temperature is increased to 1300°C, the defaceting transition occurred and grain boundaries have a smooth structure as illustrated in Fig. 2.7(d). Then NGG will take place instead of AGG. Therefore, all these studies suggest that the formation of facet grain boundaries may lead to AGG in many metallic systems.

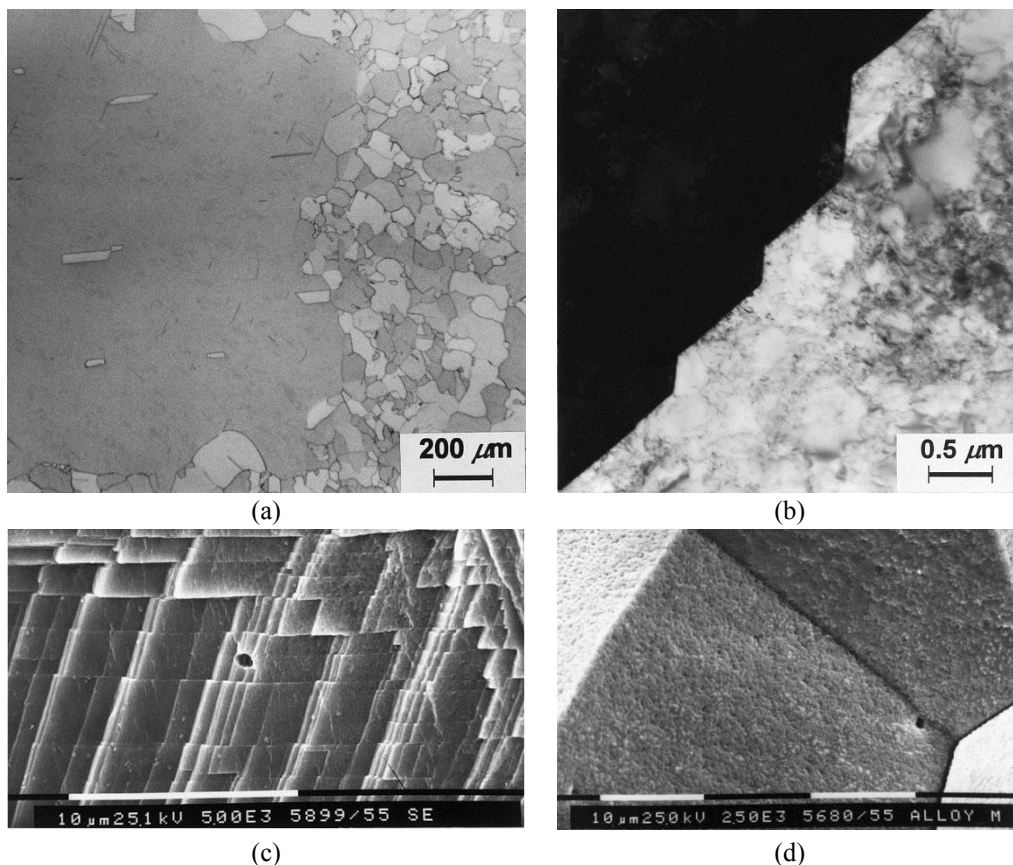


**Figure 2.7** (a) The optical microstructure of the carburized Ni specimen annealed at 0.55  $T_m$  for 90 min [14]; (b) the TEM microstructure of a faceted grain boundary [14]; (c) the intergranular fracture surface of the specimen heat-treated at 1200°C and (d) at 1300°C for 2h at a high magnification [15].

Another type of nickel-based superalloy, Inconel 718, is widely used in aircraft engines. During heat treatment, AGG has also been reported in Inconel 718 superalloy. Different from faceted grain boundaries, here the AGG is related to the dissolution of  $\delta$ -phase precipitates. More specific, Garcin et al. [18] used the laser ultrasonic technique to monitor the grain size evolution in Inconel 718 alloy. In the laser ultrasonic technique, the ultrasound attenuation is related to the mean grain size, thus this technique can be used to quantify the onset and completion of AGG. [18] The measurements are carried out during heterogeneous grain growth by isothermally holding the samples in the super- $\delta$ -solvus temperature (1050 °C) followed by Helium quench. Laser ultrasonic shows a rapid growth stage and samples quenched at this temperature have a bimodal structure. The EBSD maps of the initial microstructure is presented in Fig. 2.8(a) where all grains are of a similar size. After heat treating for 75s some grains are growing at a faster rate and the microstructure is illustrated in Fig. 2.8(b1). To quantify the area of the clusters of large grains, the maximum grain diameter in the initial structure is used as a threshold value. The EBSD map depicting only the large grains is shown in Fig. 2.8(b2). After heat treatment for 75s, some large grains are surrounded by small grains, and this bimodal size distribution is a typical characteristic of AGG.

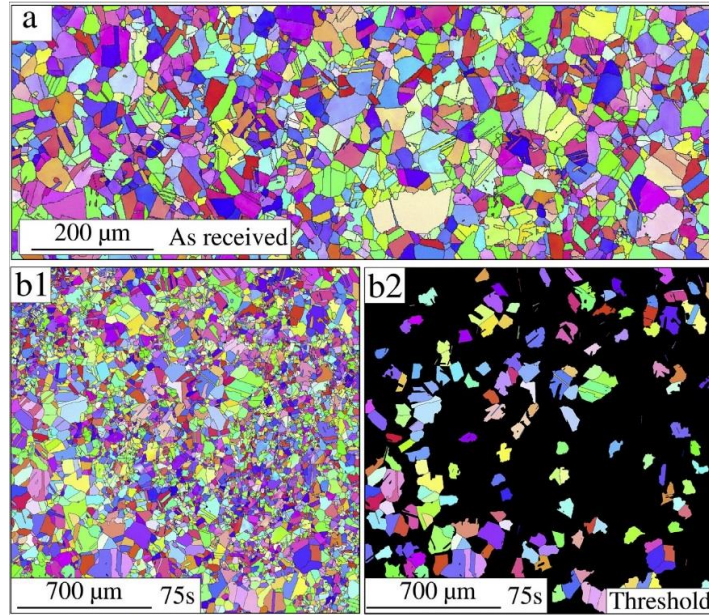


**Figure 2.8** EBSD maps of (a) the initial microstructure and of samples held at 1050°C for 75s (b1) full maps (b2) with threshold. [18]

Based on the experimental observations, Jana et al. [17] tried to summarize the role of pinning into a stability map. Their research about AGG used friction stir processed (FSP) alloys as experimental samples, e.g. cast F357 Al alloy [17]. A dimensionless parameter  $z(= 3 f \bar{R}/d)$  is introduced to describe the influence of second phase particles, where  $f$  and  $d$  are the volume fraction and diameter of the second phase particles and  $\bar{R}$  represents the mean equivalent radius of the matrix grains. [17] After introducing parameter  $z$ , Jana et al. [17] derived an equation to identify the bounds between stable and unstable growth. By plotting the bounds into the same graph, one can obtain a stability map as presented in Fig. 2.9, in terms of  $z$  and the size ratio  $X(= R_{ab}/\bar{R})$  where  $R_{ab}$  is the size of the abnormal grain. The lower bound  $X_{\min}$  is the size ratio of the smallest grain that can grow abnormally, and  $X_{\max}$  is the maximum value once the growth is complete. According to such a map, the grain growth mode can be summarized as [17]

$z = 0$  normal grain growth

$0 < z < 0.1$  broadening of grain size distribution

- 0.1 < z < 0.25 abnormal grain growth and normal grain growth
- 0.25 < z < 1 abnormal grain growth but no normal grain growth
- z > 1 no growth

Apart from FSP cast Al alloys, particle pinning has also been proved to be a potential trigger of AGG in some other Al alloys. For instance, in Al-3.5 wt % Cu alloy, some grain boundaries were pinned by CuAl<sub>2</sub> particles thus leading to AGG. [16]

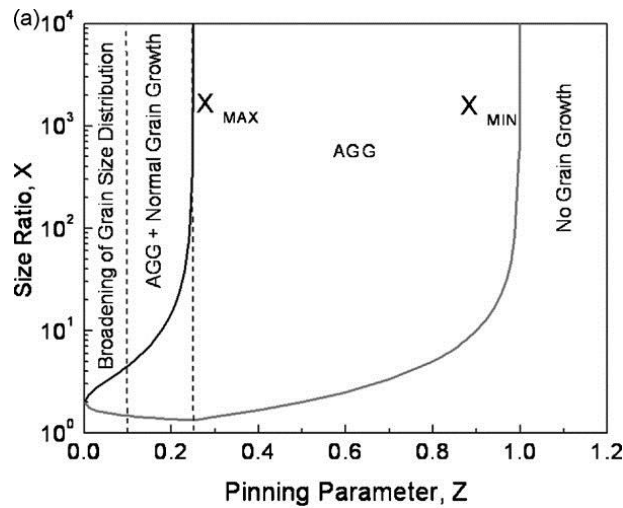
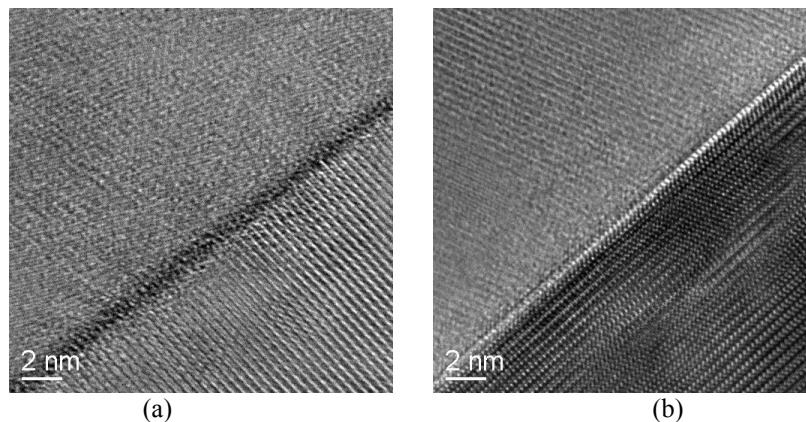


Figure 2.9 Microstructure stability map of F357 alloy. [17]

### 2.1.3 Abnormal grain growth in ceramics

AGG has been observed in alumina ceramics during sintering processes. [19-21] The prevention of AGG in the final stage of densification is of great importance if one choose sintering to obtain high-density ceramics. [20-21] Thus to investigate the conditions and mechanisms for AGG to occur is helpful to control AGG in ceramics fabrication. One possible explanation is that AGG in alumina ceramics is associated with the formation of intergranular films. Those intergranular films have been proved to enhance the grain boundary velocity by orders of magnitude. [19-20] In calcia doped alumina, the grain boundaries contained thin intergranular films (Fig. 2.10a) often migrate faster than the slow growing basal planes without such films (Fig. 2.10b). Shen et al. [19] also

argued that faceting is not important any more for the grain growth kinetics in calcia-doped alumina ceramics, but the intergranular films play a more critical role. In addition, the presence of  $\text{SiO}_2$  and  $\text{CaO}$  impurities in alumina ceramics will induce AGG as well through the formation of intergranular glass films. [20] During sintering at  $1900^\circ\text{C}$ , if the concentration of  $\text{SiO}_2$  or  $\text{CaO}$  exceeds its solubility limit, a liquid phase should form along grain boundaries as aluminosilicate-glass or calcium aluminate-glass, respectively. [20] This uneven distribution of a small amount of liquid phase can be the primary cause of AGG, since it changes the grain boundary structure and thus may lead to the variation of boundary mobility.



**Figure 2.10** (a) A grain boundary from calcia doped alumina containing a 0.6nm intergranular film; (b) a basal plane grain boundary on an abnormal grain with no film. [19]

Apart from alumina, silicon nitride ( $\text{Si}_3\text{N}_4$ ) is another kind of ceramic material exhibiting excellent mechanical properties but is sensitive to AGG. [22-23] However, the low fracture toughness of  $\text{Si}_3\text{N}_4$  limits their engineering applications. [22] One toughening strategy is the development of bimodal microstructures through AGG. [22-23] At the early stage of consolidation, a local liquid phase is formed as well, however this intergranular liquid phase does not lead to AGG as in alumina ceramics since a rapid homogenization occurs in a short time. Rather than grain boundary

structure, the composition of starting powders plays a more important role during AGG in silicon nitride. Dressler et al. [22] found that AGG is more likely to occur when initially  $\text{Si}_3\text{N}_4$ -powders possess a narrow  $\beta$ - $\text{Si}_3\text{N}_4$ -grain-size distribution with faceted elongated  $\beta$ - $\text{Si}_3\text{N}_4$ -crystals. Emoto et al. [23] studied the grain growth behavior of  $\beta$ - $\text{Si}_3\text{N}_4$  by annealing fine-grained  $\beta$ - $\text{Si}_3\text{N}_4$  ceramics with different amount of  $\beta$ -nuclei and AGG was observed with a low nuclei fraction (0.1-10 wt%). The SEM micrograph after heat treatment at 1800°C of fine-grained  $\beta$ - $\text{Si}_3\text{N}_4$  powders containing 3% nuclei is illustrated in Fig. 2.11(a) while its grain-size distribution showed a bimodal feature as presented in Fig. 2.11(b). In the SEM micrograph, several elongated large grains are located in the fine grain matrix, and the size of the elongated grains are several times larger than that of the matrix grains. The distinct size advantage is reflected in the bimodal grain size distribution shown in Fig. 2.11(b). The first peak is the population of the finer matrix grains while the second peak represents the existence of the elongated large grains.

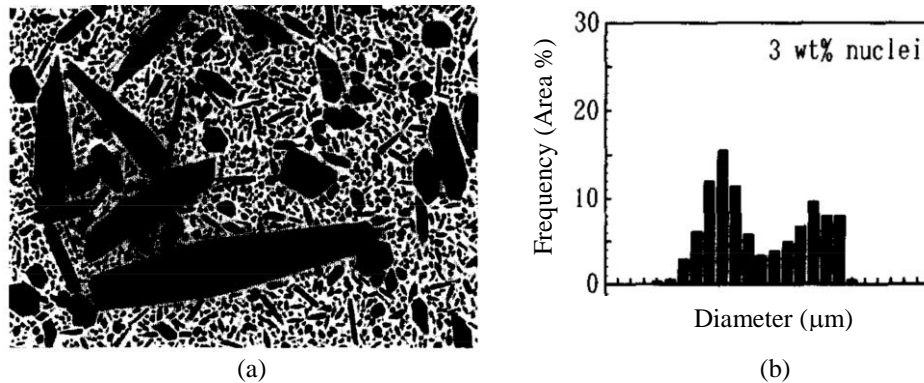


**Figure 2.11** (a) SEM micrograph (b) grain size distribution after heat treatment at 1800°C of materials containing 3% nuclei. [23]

Barium titanate ( $\text{BaTiO}_3$ ) is another typical ceramic material exhibiting AGG, and its electrical properties are considerably affected by grain size and distribution, thus the grain size of this ceramics need to be carefully controlled. [24] During heat treatment, the AGG in  $\text{BaTiO}_3$  ceramics

is highly related to the grain boundary faceting. When grain boundary faceting occurs, the {111} twins will enhance the growth of abnormal grains in a direction parallel to the twin plates. [24] This {111} twins are not necessary for AGG but beneficial for AGG when grain boundaries are faceted. Fig. 2.12(a) shows the microstructure of 0.1 mol% TiO<sub>2</sub>-added BaTiO<sub>3</sub> sintered at 1250°C for 10h in air. When looking at the micrograph with a high magnification in Fig. 2.12(b), one can easily find an abnormally large grain surrounded by the finer matrix grains. After a longer time, the abnormal grains grow further to impinge upon each other while the growth of the fine matrix grain is not appreciable.

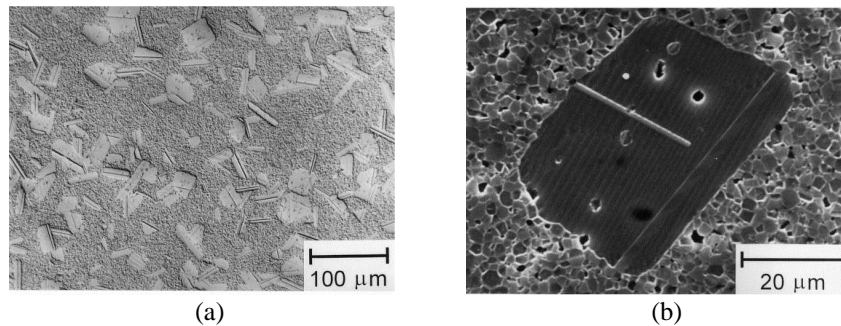


**Figure 2.12** (a) Microstructure (b) SEM micrograph showing abnormal grains in 0.1 mol% TiO<sub>2</sub>-excess BaTiO<sub>3</sub> sintered at 1250°C for 10h in air. [24]

## 2.2 Theory of abnormal grain growth

During the past few decades, many hypotheses have been proposed to describe the process of AGG. It is generally accepted that AGG may be caused by anisotropy in grain boundary energy (wetting phenomenon) and/or anisotropy in grain boundary mobility. [25-26] Such anisotropy in grain boundary mobility may be attributed to selective unpinning of grain boundaries due to dissolution of precipitates [27-28] and transitions in grain boundary structures with associated mobility changes [9]. In essence, all these mechanisms produce highly mobile boundaries that promote AGG.

In 1965, Hillert [29] put forward a model to describe AGG as shown in Fig. 2.13 for a system with second-phase particle pinning. In this model, Hillert introduced a pinning parameter  $z (= 3f/4r)$ , where  $f$  and  $r$  represent the total volume fraction and the uniform size of the second-phase particles. As indicated in Fig. 2.13, there exist two grain size limits. The lower limit is located at  $1/3z$  below which the driving force is larger than pinning force. Thus, all grain boundaries can move and NGG occurs. The upper limit is situated at  $1/2z$  above which the driving force is less than pinning force. All grain boundaries are pinned and no grain growth of any kind can take place. AGG will take place only if the pinning parameter is between  $1/3z$  and  $1/2z$ , within which for some grain boundaries, but not for all, the driving force is larger than pinning force. When some grain boundaries start to move while others are pinned, AGG is much more likely to occur. Even though the average grain size cannot exceed  $1/2z$ , the final grain size of an abnormal grain can be much higher than the upper limit  $1/2z$ . In this model, increasing the distance between these two limits will benefit the AGG process.

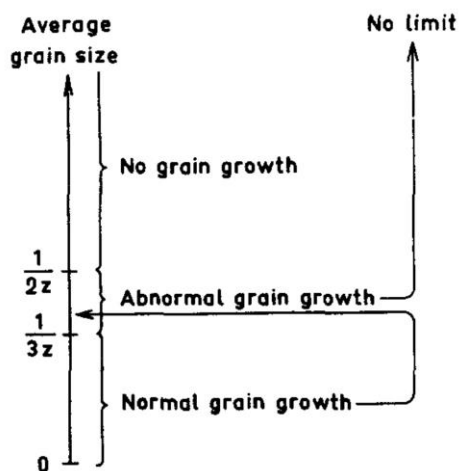


**Figure 2.13** Relation between average grain size and grain growth process [29]

Taking Hillert's formalism [29] as a starting point, Rios [27] derived a deterministic criterion for abnormal growth of a candidate grain in a matrix with unstable particles. Many theoretical models normally assume the pre-existence of a grain with some sort of "advantages" for AGG to occur, however, in Rios's theory, AGG can develop from a matrix without initial size advantage that on its own would lead to AGG. This means the initial size advantage is not a necessary condition of AGG, but itself will benefit AGG. If a "candidate grain" grows into a region where the pinning force is lower,  $Z-\Delta Z$ , than the average pinning force,  $Z$ , then this grain will grow abnormally provided it is adjacent to a region where the pinning force is less than the average pinning force by a sufficient high amount, i.e.

$$\frac{\Delta Z}{Z} > R_{Cr}^3 \frac{n^3}{(n-1)^2} \left( -\frac{d(Z/\alpha)}{dt} \right) \frac{1}{\mu\gamma\alpha} \quad (2.1)$$

Here  $R_{Cr}$  is a hypothetical critical grain radius in Hillert's Theory, and this  $R_{Cr}$  value is related to the curvature of the grains. [29]  $\mu$  is the grain boundary mobility,  $\gamma$  is the grain boundary energy per unit area and  $\alpha$  is a geometric factor. Parameter  $n$  ( $= R_{max}/R_{Cr}$ , where  $R_{max}$  is the maximum grain radius) is related to grain size distribution. According to Eq. 2.1, [27] AGG is influenced by many factors, such as distribution width, rate of decreasing in pinning force, boundary mobility and boundary energy etc.

Knowing that the decrease in pinning force will affect AGG [27], Abbruzzese [30] and Novikov [31] did a systematic study on the influence of unstable inhibitors (Zener drag etc.). Abbruzzese et al. [30] introduced an inhibition factor  $I_Z$  ( $= \beta \cdot f/r$ , where  $\beta$  is a constant) to describe the

pinning effect of second phase particles, and  $I_Z = 0$  in NGG. In systems with dissolving second phase particles, the inhibition factor  $I_Z$  decreases continuously but with a different rate ( $dI_Z/dt$ ). While the decreasing rate ( $dI_Z/dt$ ) is changing from  $0.02 \text{ cm}^{-1}/\text{s}$  to  $0.4 \text{ cm}^{-1}/\text{s}$ , the results are plotted into a double logarithmic graph shown in Fig. 2.14. [30] This graph mainly shows the variation of average equivalent grain area radius versus time. The dashed line describing NGG ( $I_Z = 0$ ) is used as a reference line to measure the abnormality of other grain growth processes. The decreasing trend of the inhibition factor is plotted as thin solid curves. Meanwhile, the thick solid curves ranging from (A) to (E) representing the evolution of mean grain radius with increasing inhibition decay rates. When the pinning particles dissolving at a slower rate, the deviation from the dashed line becomes larger. Thus, the decay of the inhibition is responsible for the AGG kinetics. [30] In addition, a lower drop rate enlarges the size of the final abnormal grains and amplifies the presence of a bimodal grain size distribution. [30-31]

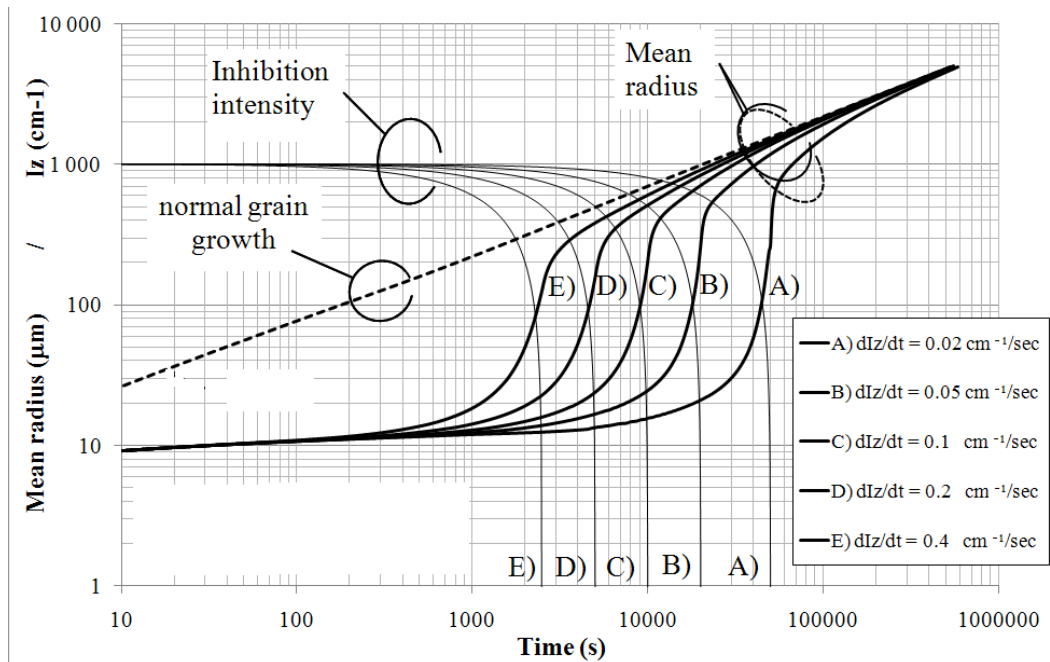


**Figure 2.14** Rate of inhibition drop and mean radius growth [30]  
 $(\mu = 1.93 \times 10^{-2} \text{ cm}^4/\text{J}/\text{sec}, \gamma = 6 \times 10^{-5} \text{ J}/\text{cm}^2: \text{ from Fe-3\% Si at } 980^\circ\text{C})$

Apart from particle pinning, the solute drag effect and grain boundary segregation can also induce AGG. [28] In systems with solute drag, the relationships between grain boundary velocity and driving force is depending on solute diffusivity as well, as seen in Fig. 2.15(a). [28] The straight black line represents the velocity where the grain boundary is free from segregation. For various solute diffusivities:  $3 \times 10^{-14}$  m<sup>2</sup>/s (green),  $1 \times 10^{-13}$  m<sup>2</sup>/s (red), and  $3 \times 10^{-13}$  m<sup>2</sup>/s (magenta), there exist an inflection point, where the grain boundary velocity jumps discontinuously. After that, the grain boundary almost frees itself from the solute drag. This jump in velocity is indicated by a vertical red arrow in Fig. 2.15(a). When diffusivity is large enough, such as  $1 \times 10^{-12}$  m<sup>2</sup>/s in blue, the transition becomes continuous. For the convenience of description, the complicated relationships in Fig. 2.15(a) can be simplified into Fig. 2.15(b), showing a direct jump regardless of the diffusivity. In this simplified model, the kinetics of grain growth is dependent on whether grain boundaries can break away from the segregation atmosphere. In Fig. 2.15(b), when the driving force reaches a critical value, the grain boundaries break away and undergo a discontinuous jump from a low-velocity regime to a high-velocity regime. [28] There are two necessary conditions for AGG accompanying segregation. First, a critical driving force must exist where the grain boundary velocity jumps discontinuously. [28] Second, only a minor portion of the grain boundaries break away from the segregated solute atoms. [28]

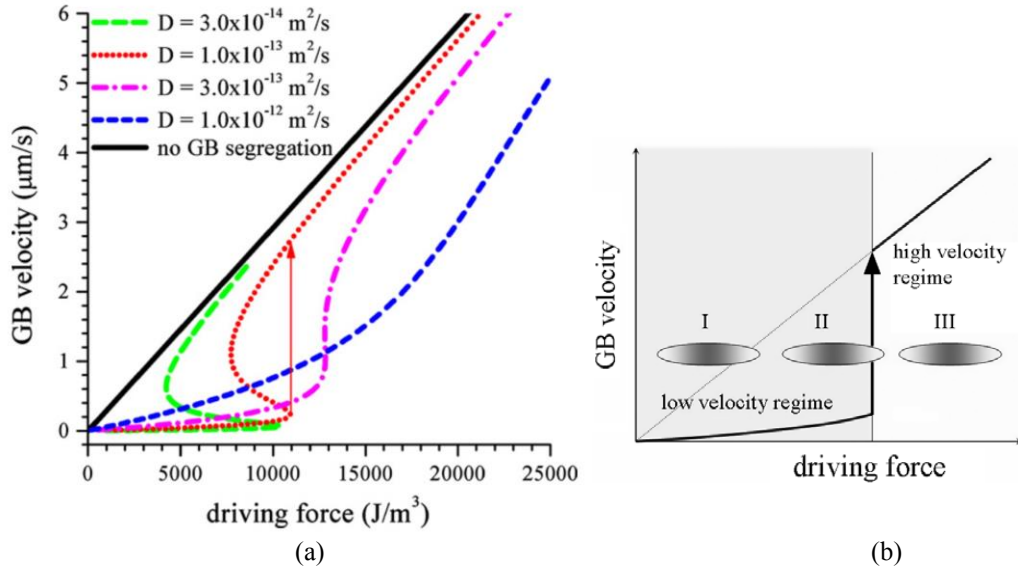


**Figure 2.15** Grain boundary velocity under the solute drag effect as a function of driving force. (a) Theoretical model; (b) simplified model. [28]

Knowing the conditions under which AGG is most likely to occur, one can plot a mechanism map to describe AGG. Anderson et al. [32] derived a series of equations describing the behavior of grain growth to develop a mechanism map shown in Fig. 2.16, revealing the boundary dividing NGG and AGG. It is assumed that one candidate grain is initially surrounded by a normal grain matrix with particle pinning. Here  $\bar{D}$  and  $\bar{D}_{ab}$  refer to the average diameter of the normal matrix grains and the abnormal grain, respectively.  $\bar{D}_{Lim} \{= k(r/f)\}$  is the limiting average grain size, where  $k$  is a constant, meanwhile  $r$  and  $f$  represent the mean radius and total volume fraction of the pinning particles, respectively. This limiting average grain size is related to the presence of pinning particles. As indicated in Fig. 2.16, in the limiting case where the  $(\bar{D}/\bar{D}_{Lim})$  ratio approaches to 1, all grains with a size advantages larger than 1.4 will grow in an abnormal manner. [32] In practice, AGG occurs under conditions where the matrix grain boundaries are strongly pinned by second phase particles. [32] In contrast, NGG occurs under conditions where  $(\bar{D}/\bar{D}_{Lim})$  ratio approaches to 0, where the grain boundaries can move virtually unhindered.

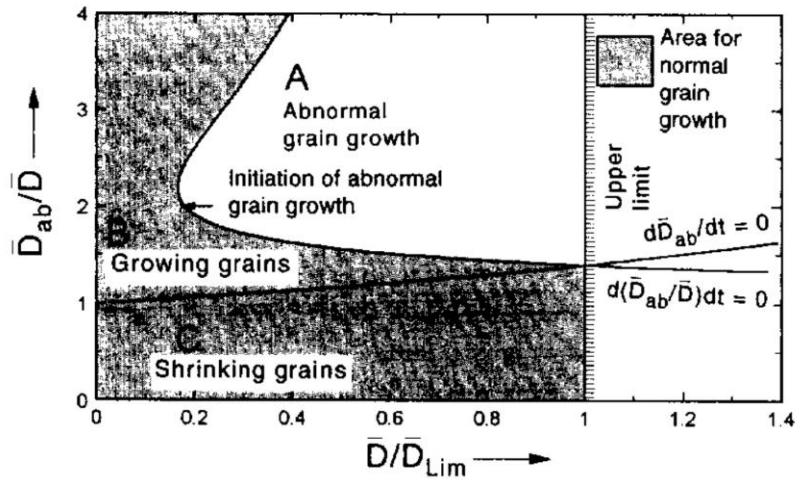


Figure 2.16 Mechanism map for abnormal grain growth. [32]

The mechanism maps plotted by Anderson et al. [32] describe the situations where the mean matrix grain size  $\bar{D}$  is less than the limiting grain size  $\bar{D}_{Lim}$ , thus the maximum available  $\bar{D}/\bar{D}_{Lim}$  value is 1.0. Based on Anderson's model [32], Perez et al. [33] extended the available  $\bar{D}/\bar{D}_{Lim}$  value further to nearly 2.0, and the y-scale is valid above the red shaded area in Fig. 2.17 where  $\bar{D}_{ab}/\bar{D}$  is larger than 1.0. The improved mechanism map is presented in Fig. 2.17. This map was successfully tested and validated on a low alloy steel presenting various states of precipitation depending on heat treatments. [33] The map consists of 6 domains:

- ① normal and abnormal grains grow in a stable manner
- ② normal grains can grow
- ③ normal grains are pinned
- ④ both abnormal and normal grains are pinned
- ⑤ normal grains are pinned, whereas the abnormal grain grows
- ⑥ normal and abnormal grains grow in an unstable manner

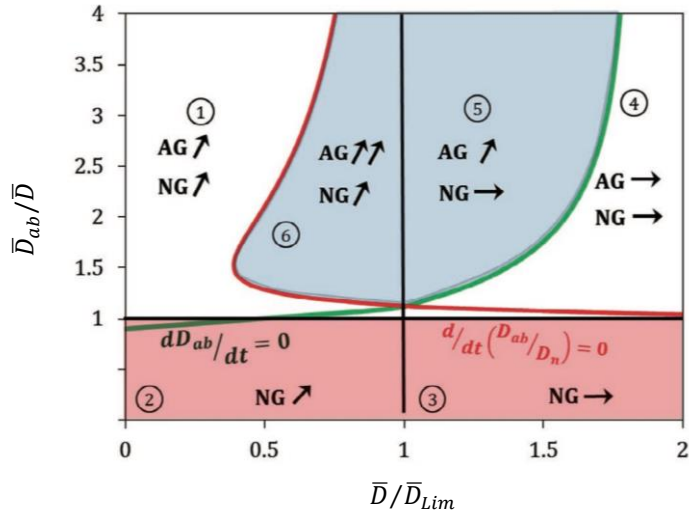


Figure 2.17 Improved mechanism map for AGG. [33]

## 2.3 Computational simulation methods

### 2.3.1 Phase field modelling

The physical and mechanical properties of materials highly depend on the microstructure which can be described in detail with computational models on the mesoscale, i.e. the scale of the microstructure. In these models, the microstructure is in general viewed as a thermodynamic unstable system that evolves with time. [34] Phase field modelling is a meso-scale modelling technique frequently used to simulate microstructure evolution. In addition, PFM is a diffuse-interface approach and does not require to track interfaces explicitly. Besides, PFM is a powerful modelling method especially suitable to describe geometrically complex microstructure features, e.g. abnormal grain growth and solidification (including dendrite formation) [35-36]. Other than grain growth, PFM is also used to study many other metallurgical phenomena, e.g. recrystallization [37-38], phase transformation [39-40] etc.

The grain distribution is represented by phase-field variables that are continuous functions of space and time. Within the grains, the phase-field variables have constant values while across the grain boundaries, the phase-field variables gradually vary between their values in the neighboring grains. The phase-field variables can either be conserved, e.g. composition variables, or non-conserved, e.g. order parameters. The evolution of those variables is governed by a set of partial differential equations, i.e. Ginzburg-Landau equation for non-conserved variables and the Cahn-Hilliard equation for conserved variables. [34] The basic principle is minimizing the free energy of the system. The evolution of the microstructures thus can be described as the evolution of the phase-field variables.

Although there are many commonalities to all phase-field methods, there exist several possibilities to implement the phase field. Here two frequently used PFMs are compared, namely the continuum-field (CF) model and the multi-phase-field (MPF) model. In the CF model, the field variables are treated as being independent. In MPF models, the phase fields are interpreted as volume fractions and therefore subject to the constraint that the sum of the phase field values must be equal to one. [41] Grain growth simulation results of CF and MPF models are compared in Fig. 2.18 for a 2D system with two texture components. Both simulations start from the same initial microstructure as indicated in bold in Fig. 2.18(a) where A grains are shown in green and B grains in red. Grain boundaries between grains of the same type have the same grain boundary energy  $\sigma_{AA} = \sigma_{BB} = 0.2 \text{ J/cm}^2$  while those between different types have  $\sigma_{AB} = 0.25 \text{ J/cm}^2$ . All grain boundaries share the same boundary mobility value of  $\mu = 1.0 \text{ cm}^4/(\text{Js})$ . The microstructure images of different simulation times are captured and presented in sequence from left to right in Fig. 2.18(b). Simulation results of the CF model are plotted in blue solid lines while results of the MPF

model are drawn in green dashed lines. In this figure, the disappearing grains have the tendency to shrink faster in the CF simulations than in the MPF simulations. However, the overall evolution of the grain assembly is the same for both models.

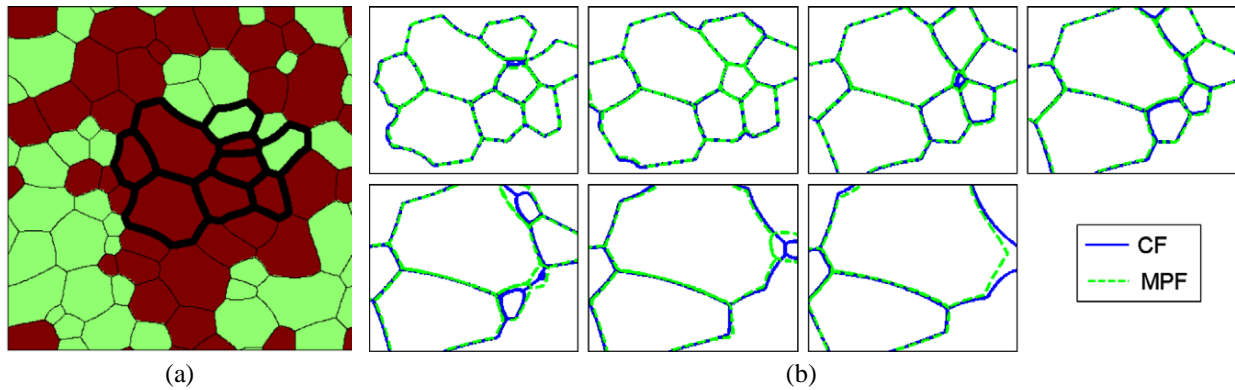


**Figure 2.18** Microstructure evolution of the selected grains in the 2D structure. [41]

- (a) Initial microstructure in 2D system: Grain A in green and Grain B in red;
- (b) comparison between CF and MPF simulation. Images from left to right are for time = 150, 300, 600, 900 (first row) and 1200, 1500, 1800 (second row).

Besides this general comparison, several specific examples of PFM grain growth simulations are described. Inhomogeneous grain growth tend to occur in a system with second phase particles [42-44] due to their ability to affect the motion of grain boundaries. Moelans et al. [42] used PFM to simulate 2D grain growth as shown in Fig. 2.19 to investigate the effect of resolved precipitates. In this model, initially 0.015 area fraction of second-phase particles with a radius of 3 grid points are located at grain boundaries as displayed in Fig. 2.19(a). Due to the presence of these immobile precipitates, some grain boundaries are not affected and can escape from the particles while others can not. As a consequence, some grains, such as Grain K in Fig.2.19(c), may grow faster than other grains. One thing noteworthy is that grain boundaries in PFM easily become straight and therefore lack the driving force to pass the precipitates. [42] Precipitates are located at the grain boundaries because it lowers the free energy.

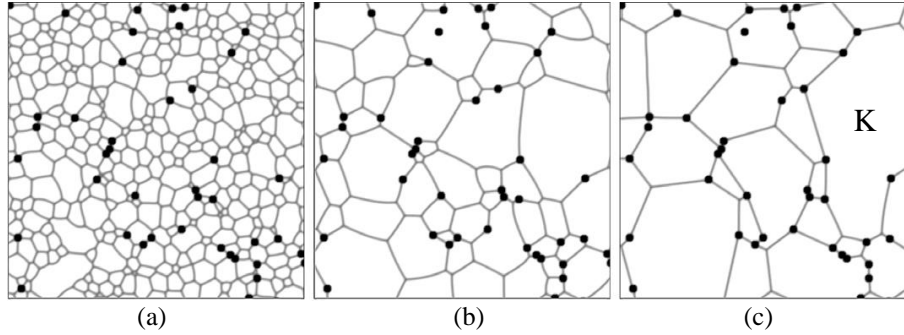


**Figure 2.19** PFM of grain growth containing second-phase particles at different time steps. (a) 200, (b) 3000 and (c) 30,000 [42]

In many polycrystalline materials, other than large precipitates, the drag effect from second-phase particles [42-44] and solute drag [45] also occur on a scale comparable to the particle diameter and interface thickness. [46] MPF model is an effective tool to capture this kind of drag pressure on the interfaces. Shahandeh et al. [46] thus used MPF model to simulate 2D and 3D grain growth under constant and velocity-dependent drag pressure. In their MPF model, this drag pressure is directly introduced as a pinning pressure term in phase-field equations, rather than bringing real particles or solute segregation into the system. Fig. 2.20 displays an example for a 2D grain structure for different simulation times in sequence. [46] In the early stage shown in Fig. 2.20(a), the grain growth occurs in all regions. As the simulation progresses, some grain-boundary segments with a stable topological neighbourhood freeze, as shown within the box in Fig. 2.20(b), while other grains still keep growing. Gradually, the fraction of the growing part reduces with time till eventually all grain boundaries are totally pinned. After 20 000 time steps, the final frozen structure is captured in Fig. 2.20(c). In this 2D PFM simulation, some grain boundaries tend to become straight. Due to the associated loss of boundary curvature, pinning pressure is larger than driving force and gradually grain growth stops. [43,47]

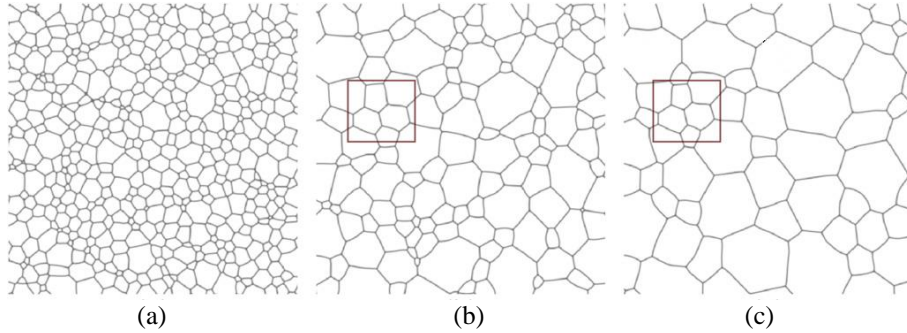


**Figure 2.20** PFM of grain growth with pinning pressure at time of (a) 200, (b) 2000 and (c) 20,000. [46]

Another interesting phenomenon that may induce AGG is inverse pinning. With a large number of precipitates dispersed in the system, in some occasion the surface energy of these precipitates in grains of type A is smaller than that in grain type B. This energy difference leads to different pinning pressure for different grain boundaries making some grain boundaries more mobile than others. [47] This phenomenon is defined as inverse pinning. The possibility of AGG induced by inverse pinning was verified through PFM simulations. For simplicity, the system with several A grains located in a matrix of B grains is considered, and 5000 precipitates (P) are homogeneously distributed in that system. [47] Further, the precipitates (P) have a special boundary relationship with B grains, where only the BP interface has a higher boundary energy and the other interfaces have all the same but smaller boundary energy. As a consequence, the Grain B boundaries will experience a larger pinning force than Grain A boundaries. Thus, A grain boundaries can move faster. Fig. 2.21 depicts the microstructure images after a series of simulation times. This figure indicates that the A grains grow abnormally at the expense of B grains due to the anisotropy of boundary mobility caused by inverse pinning.

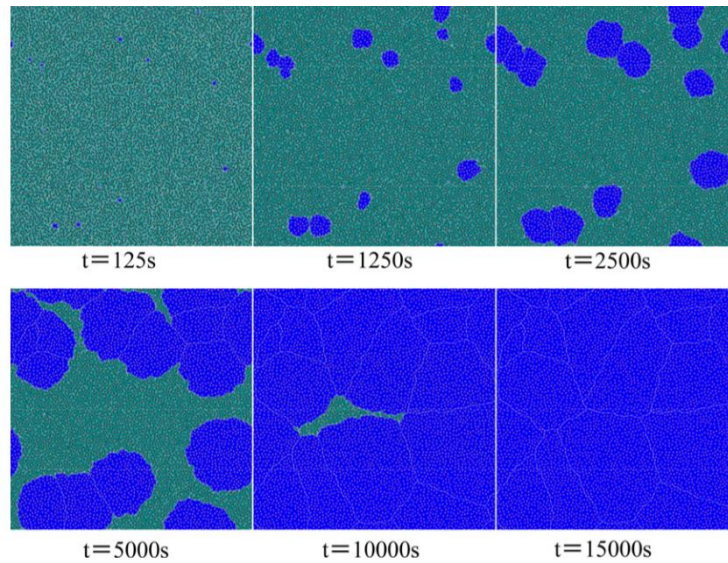


**Figure 2.21** Microstructure evolution of the polycrystalline system with 5000 particles. [47]

### 2.3.2 Monte Carlo simulation

As a typical example for sharp-interface models, Monte Carlo (MC) methods have been widely used in computer simulations of grain growth. [48-55] The concept behind the MC method in grain growth is the thermodynamics of volume site interactions. In MC models, the initial microstructure is represented with a matrix as shown in Fig. 2.22 for a 2D example, in which each site corresponds to a site element. The content of each element represents its crystallographic orientation. After filling the matrix with an initial content, the simulation algorithm consists of four main steps: [48]

- a) Calculation of the free energy ( $G_i$ ) of an element with its crystallographic orientation ( $Q_i$ ) based on its eight neighbor elements in 2D simulation.
- b) Random selection of a new crystallographic orientation ( $Q_f$ ) for that element.
- c) Calculation of the new free energy ( $G_f$ ) with the new crystallographic orientation ( $Q_f$ ).
- d) Comparison of the free energy difference ( $G_f - G_i$ ). Identify the crystallographic orientation that minimizes the free energy.

These four steps are repeated millions of times in random positions of the matrix. Each cycle of these four steps is defined as one Monte Carlo step (MCS). The overall result is the free energy decay in the system.

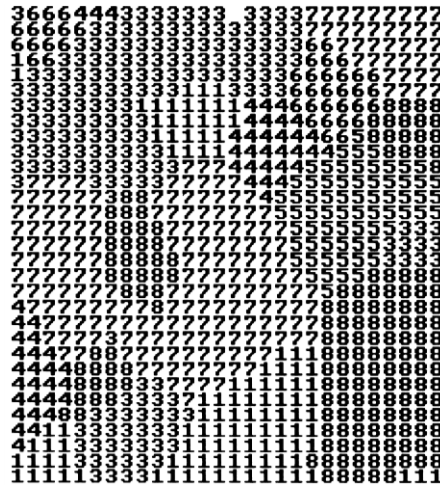
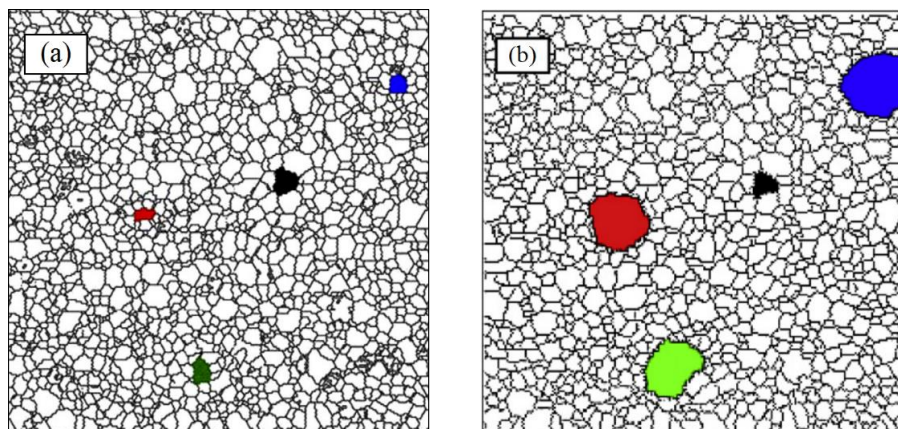


Figure 2.22 An example grain structure represented by a 2D square matrix. [48]

MC simulations have been performed to describe selective growth of Goss grains in textured Fe-3% Si steel [49-51]. In these simulations, the AGG of Goss grains is linked to either mobility advantages due to the presence of precipitates, such as AlN and MnS [49], or due to sub-boundary enhanced solid-state wetting [50, 51]. Maazi et al. [49] conducted 2D MC simulations to consider the role of precipitates by making the assumption that Goss grain boundaries experience less pinning force than the matrix grain boundaries. An example of their simulations is shown in Fig. 2.23. The experimental microstructure shown in Fig. 2.23(a) has been used as starting state. There are four Goss grains in this initial microstructure which are shown in color (blue, red, black and green). All boundaries have the same mobility and energy but the pinning force on the Goss grain boundaries is assumed to be four times smaller than at other boundaries. After 400 MCS, as shown

in Fig. 2.23(b), three of the four Goss grains (Goss grains in blue, red and green) have grown abnormally. AGG of the Goss grains is further promoted when assuming that their grain boundaries have lower energies than the boundaries of the matrix grains. Alternatively, Ko et al. [51] show with 3D MC simulations that AGG of Goss grains can occur due to sub-boundary enhanced wetting provided a significant anisotropy in grain boundary energy of matrix grains exist. Further, Park et al. [50] combine the role of precipitates and sub-boundaries in their 3D MC simulations. They also assume anisotropy of grain boundary energy and further consider that precipitates in triple junctions and quadruple points gradually dissolve thereby enabling solid-state wetting of triple junctions. As the presence of precipitates inhibit normal grain growth of the matrix grains higher energy boundaries cannot be eliminated as would be the case without precipitates. Thus, in the presence of precipitates the degree of grain boundary energy anisotropy remains sufficiently high such that AGG can occur. Grains that undergo AGG under these conditions have highly irregular shapes, as shown in Fig. 2.24. It shows a two-dimensional cross-section of a 3D microstructure after 9000MCS in the presence of precipitates.



**Figure 2.23** (a) Initial microstructure from an experimental result; (b) Evolution of the microstructure after 400MCS when the pinning force for Goss grains is four times smaller than for matrix grains. [49]

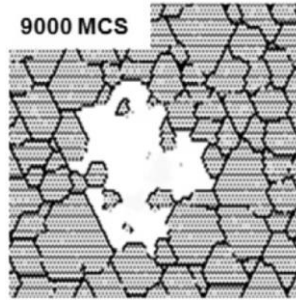


**Figure 2.24** A 2D cross-section of a 3D microstructure after 9000 MCS showing irregular shape of the abnormal grain. [50]

As discussed in section 1.3, anisotropy in grain boundary mobility may lead to AGG. To introduce mobility advantages, Rollett et al. [52] define two types of grains (Type I and Type II) according to the texture of the material. The boundaries between grains of different types (I-II boundaries) have high mobility whereas the grain boundaries between grains of the same type (I-I and II-II boundaries) have low mobility. [52] The mobility ratio  $M$  is the factor between high and low mobility values. Fig. 2.25(a) shows the microstructure evolution for a simulation where a single type I grain was placed in a matrix of type II grains when  $M = 7.5$ . A similar grain growth evolution has been simulated by Lee et al. [53] for  $M = 10$  resulting in multiple abnormal grains (Type I) in the matrix of Type II grains, as shown in Fig 2.25(b). In both cases AGG occurred since the Type I grains grow unambiguously faster than the matrix coarsens. When there is only one single grain in the system, during growth this candidate grain keeps growing in an equiaxial shape. However, if more than one type I grains are in the system, AGG will stop after type I grains impinge on each other.

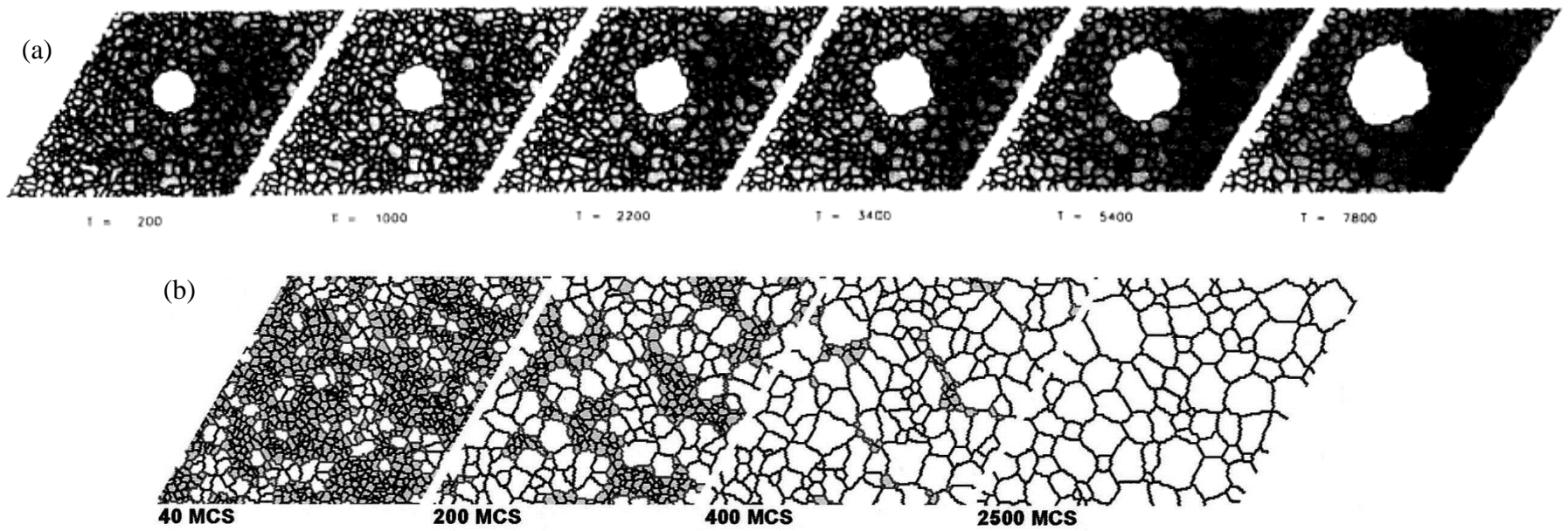


**Figure 2.25** Microstructure evolution of (a) a single abnormal grain with  $M = 7.5$  [52]; (b) multi abnormal grains with  $M = 10$  [53].

In addition, Rollett et al. [52] also used MC methods to investigate the influence of mobility ratio and the initial grain size on AGG. As shown in Fig. 2.25(a), initially one Type I candidate grain is located in the center of a matrix of Type II grains. Relative grain radius  $\rho$  is a parameter reflecting the initial size advantage of the central abnormal grain size. When setting the initial value of  $\rho = 6$  as a starting point and changing the mobility ratio  $M$  from 1.2 to 1000, the results are plotted in Fig. 2.26(a). For  $M \geq 5$ , the large central grain grows at a faster rate than the mean normal grain size, i.e. AGG is occurring. A similar parametric study has been done by Grest et al. [26], and all their results proved that large mobility advantages promote AGG. Apart from the effect of mobility ratio, Fig. 2.26(b) shows the tendency of the relative grain radius  $\rho$  of the abnormal grain when the initial  $\rho$  values were varied between 2 and 12 with  $M = 3$ . In Fig. 2.26(b) when  $M = 3$ , there is no AGG for  $\rho = 6$  and also no AGG for any other  $\rho$  values. This confirms that size advantages alone are insufficient for AGG.

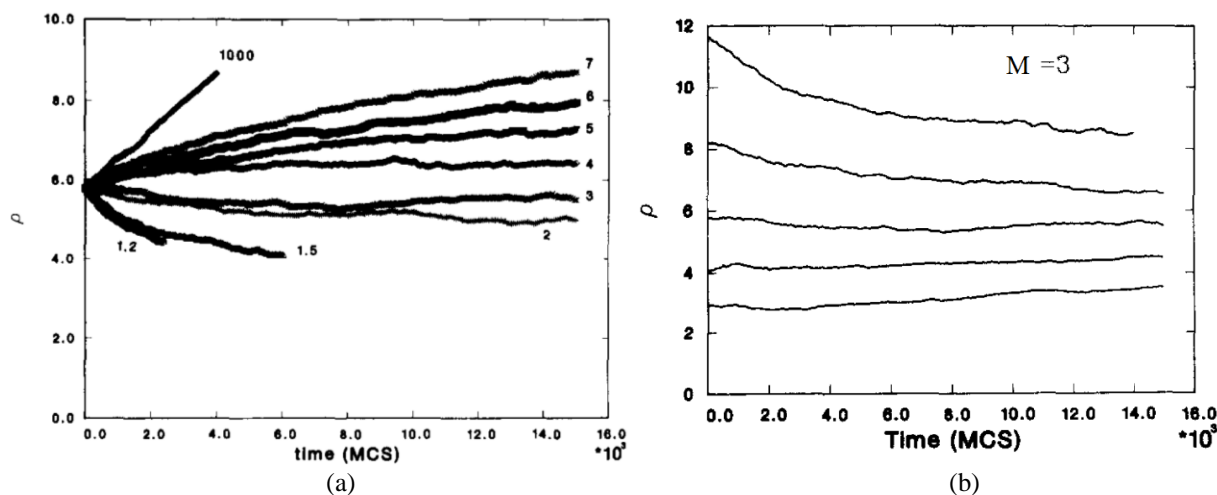


**Figure 2.26** Relative grain radius  $\rho$  as a function of time for (a) different  $M$  values and (b) different initial  $\rho$  values. [52]

The AGG evolution of two grain types is straightforward since all boundaries around Type I grains are fast boundaries. After adding one more grain type (Type III) in the matrix [54-55], only part of the central abnormal grain boundaries are fast mobile boundaries. DeCost et al. [55] made a series of MC simulations to investigate the influence of the fraction of type III grains on AGG. In their MC simulations, initially a white round type I grain is sitting in the center of the domain, whose size is 6 times larger than the matrix grains. Type II and type III grains are in red and in blue, respectively. In the previous two components system, the grain boundaries between Type II grains and the candidate grain (I-II boundaries) have high mobility and the rest of the grain boundaries have low mobility. When setting the mobility ratio  $M = 1000$  and increasing the fraction of Type II grains from 0 to 1, the simulated microstructures are illustrated in Fig. 2.27. The scale bars in the bottom-right corners of each graph mark the width of 100 grid points. When the fraction of II grains  $f_{II}$  is either 0 or 1, the microstructure evolutions in Fig. 2.27 from (a) to (d) and from (q) to (t) are both similar to the results in two components systems done by Rollett et al. [52] In between those two limiting cases, the grain shape becomes irregular when  $f_{II}$  is changing from 0.2 to 0.7. In systems with 0.4 type II grains as presented in Fig. 2.27 (i) to (l), the growth front sweeps red grains quickly and shows a tendency to embrace blue grains by forming inlet-type features. After increasing  $f_{II}$  further to 0.7 as shown in Fig. 2.27 (m) to (p), some blue grains are completely embraced and many island grains are found in the system. Island grain formation is a significant sign of AGG.

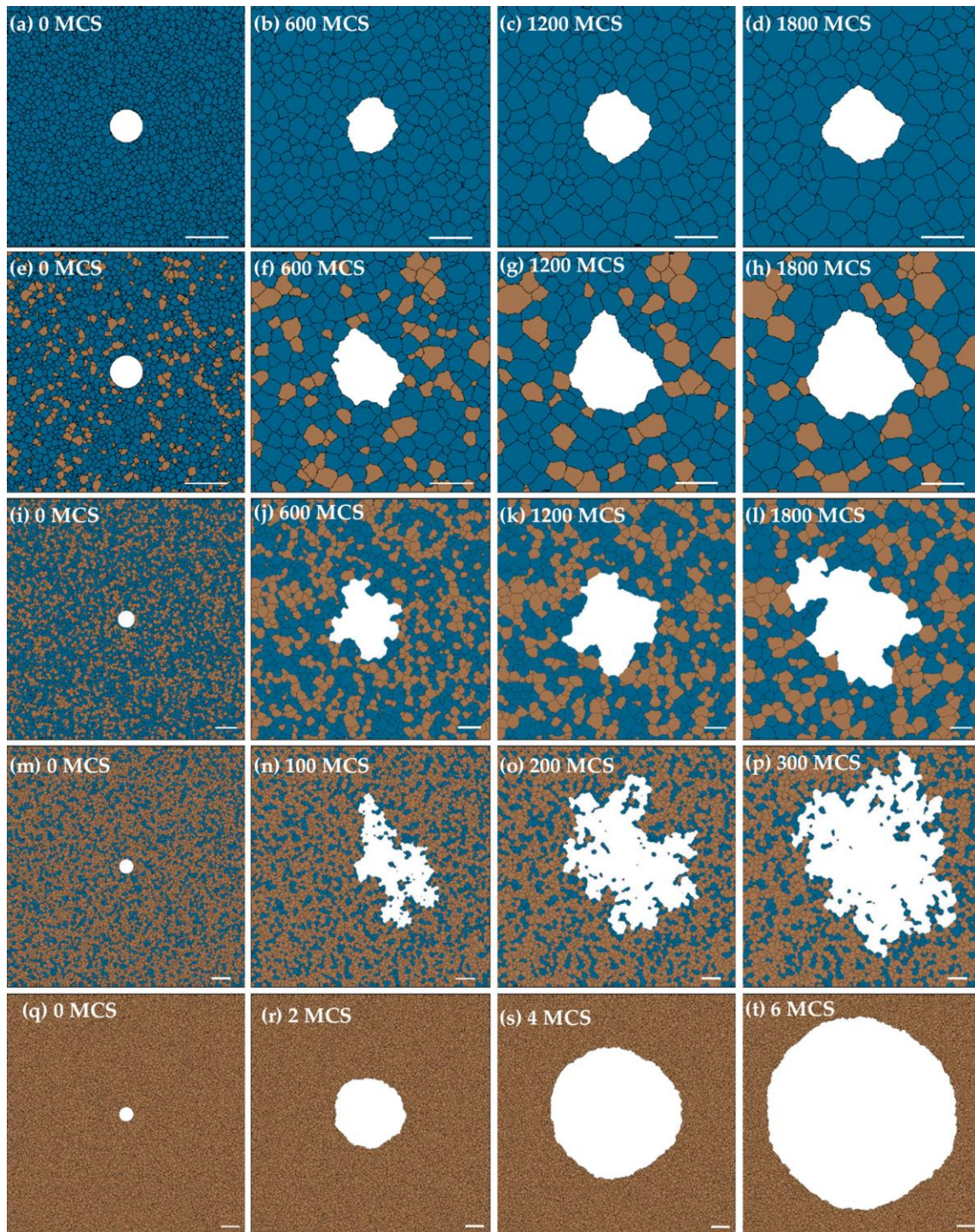


**Figure 2.27** Microstructures of AGG simulations with fractions of type II grains  $f_{II} = 0$  (first row), 0.2 (second row), 0.4 (third row), 0.7 (fourth row), and 1.0 (fifth row). [55]

Apart from anisotropy in grain boundary mobility, in addition MC methods have also been widely used to simulate the grain growth process with anisotropy in grain boundary energy [55-56], particle pinning [56-57] etc. Both two-dimensional [48-58] and three-dimensional [59] simulations have been done with MC methods.

## **2.4 Summary**

AGG is a well explored topic in materials science, both experimentally and numerically. From the experimental observations, one can find that the grain boundary properties highly depend on the grain boundary structures, e.g. disorientation angles, particle pinning, intergranular films etc. These factors often lead to mobility advantages of some selected grain boundaries, and such mobility advantages are one of the potential causes for AGG. Many theoretical models have been developed to describe the AGG processes. Based on those theoretical studies, mechanism maps have been proposed to summarize the conditions for AGG. With the progress of computer techniques, many computer models have been well developed to describe microstructure evolution during grain growth, including PFM and MC methods. In computer simulations, there are many approaches to assign mobility advantages such as introducing texture components and second-phase particles etc. In single phase systems without particle pinning and solute segregation, most simulations are focused on the effect of texture components while the role of disorientation angles are relatively less addressed. In addition, it is worthwhile to summarize the influence of both two and three texture components on AGG. In previous studies, both PFM and MC were used to simulate grain growth processes, therefore, a comparison of those two simulation methods would be of great interests.

### **Chapter 3: Scope and objectives**

In this research, multi-phase field modeling has been used for a parametric study of abnormal grain growth conditions. In particular, the influence of boundary mobility advantages, which is the main potential reason for abnormal grain growth, has been explored. Different approaches have been used to introduce the boundary mobility advantages, such as critical disorientation angles and texture components. Further, phase field simulations were compared with literature data of Monte Carlo simulation of abnormal grain growth.

Overall, the objectives can be summarized as follows:

- Identify the conditions, i.e. mobility ratio and fraction of high mobility boundaries, for abnormal grain growth to occur through multi-phase field simulation for different approaches to introduce mobility advantages:
  - a) Disorientation threshold angle
  - b) Two texture components
  - c) Three texture components
- Evaluate the consistency of different computational models, i.e. Multi-Phase Field Model and Monte Carlo Model, to simulate abnormal grain growth.

## Chapter 4: Methodology

### 4.1 Multi-phase field model

During the past few decades, it has been proven that Multi-Phase Field (MPF) modelling is a powerful computational method to simulate the microstructure evolution in polycrystalline materials, including phase transformation, recrystallization and grain growth. MPF models have two advantages compared to other simulation methods, such as Monte Carlo (MC) techniques. As a diffuse-interface model, MPF models use a finite thickness to describe the interface area, within which the physical properties change continuously. Unlike sharp-interface models such as MC models, diffuse-interface models are characterized by a gradual change of properties through the interface. The other merit is that MPF models provide outputs in a physical time rather than the numerical time of MC models.

In this research, the commercial software MICRESS<sup>®</sup> is used for MPF modeling. In MICRESS<sup>®</sup> phase field parameters  $\phi_i$  are used to describe the microstructure. The phase field parameters  $\phi_i$  are a function of space and time. In a polycrystalline system, each grain  $i$  will be assigned a phase field parameter  $\phi_i$ . As shown in Fig. 4.1,  $\phi_i$  equals 1 within grain  $i$  and its value changes continuously from 1 to 0 across the grain boundary. The grain boundary thickness  $\eta$  is a numerical parameter. By using this method, one can distinguish a number of grains in the initial microstructure.

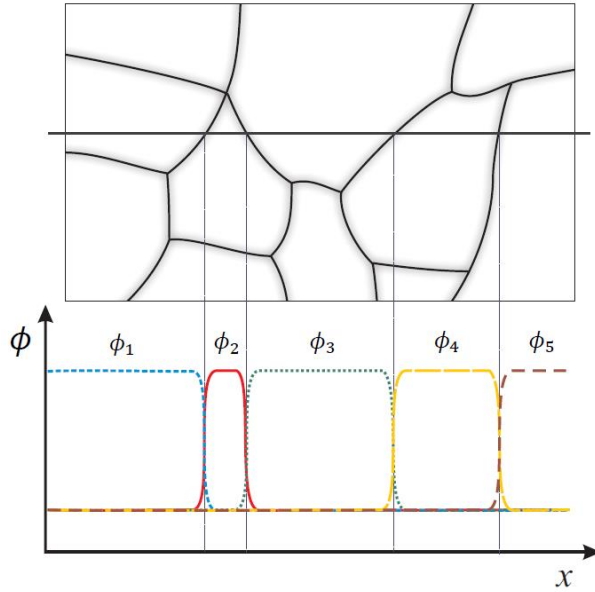


**Figure 4.1** A polycrystalline structure defined by a set of order parameters,  $\phi_i$ , associated with each grain. [60]

The evolution of the grain structure can be described by the evolution of the phase field, which is governed by the phase-field equations. The total free energy of the system can be written as a function of the order parameters, and then the evolution of the phase field parameters is governed by the minimization of the total free energy. According to the Ginzburg-Landau equation [61], the overall evolution principle can be described as:

$$\frac{\partial \phi_i}{\partial t} = -L \frac{\delta F}{\delta \phi_i} \quad (4.1)$$

Here  $L$  is a kinetic coefficient related to the grain boundary mobility.  $F$  represents the Helmholtz free energy of the system, which is the sum of bulk free energy, interface energy, etc. After writing  $F$  as a function of  $\phi_i$  and substituting back into Eq. 4.1, according to the mathematical derivation of Eiken et al. [61], the governing phase field equation used in MICRESS® can be written as:

$$\frac{\partial \phi_i}{\partial t} = \sum_j \mu_{ij} \left( \sigma_{ij} \left[ \phi_i \nabla^2 \phi_j - \phi_j \nabla^2 \phi_i + \frac{\pi^2}{2\eta^2} (\phi_i - \phi_j) \right] + \frac{\pi}{\eta} \sqrt{\phi_i \phi_j} \Delta G_{ij} \right) \quad (4.2)$$

Here  $\mu_{ij}$  and  $\sigma_{ij}$  are the grain boundary mobility and interfacial energy, respectively.  $\phi_i \nabla^2 \phi_j$  and  $\phi_j \nabla^2 \phi_i$  are gradient terms and  $\frac{\pi^2}{2\eta^2} (\phi_i - \phi_j)$  is a stabilizing term.  $\Delta G_{ij}$  represents the driving pressure and for grain growth,  $\Delta G_{ij}$  is 0. However,  $\Delta G_{ij}$  can be used in grain growth simulations to account for pinning pressure and/or solute drag. In the present study on AGG, the driving force is due to grain boundary curvature and this has already included in the gradient terms. Since pinning and drag effects are not considered, thus the governing equation can be simplified as

$$\frac{\partial \phi_i}{\partial t} = \sum_j \mu_{ij} \cdot \sigma_{ij} \left( \phi_i \nabla^2 \phi_j - \phi_j \nabla^2 \phi_i + \frac{\pi^2}{2\eta^2} (\phi_i - \phi_j) \right) \quad (4.3)$$

The simulated grain structure evolution is quantified by measuring, at selected times, the area of each grain  $i$  based on its phase field parameter whereby grid points in the grain boundaries contribute with a fraction that is given by the value of the phase field parameter  $\phi_i$ .

## 4.2 Simulation approaches

### 4.2.1 General simulation setup

In this research, two approaches are used to introduce mobility advantages: one is setting a critical disorientation angle while the other is through texture components. For both scenarios, firstly a series of 2D simulations were conducted, then based on the 2D simulation results, several 3D simulations were performed to further verify the 2D results.

In 2D simulations, all simulations were conducted in square domains, but the domain size varied in different scenarios. In the critical disorientation case, the square domain has a size of  $800 \times 800$  grid points which contained 1800 grains. For simulations of two and three texture components, initially in total 1800 grains were distributed in a larger square domain with a size of  $850 \times 850$  grid points. However, for computational efficiency, a smaller domain was also used in systems containing three texture components with only  $300 \times 300$  grid points and 120 grains. In 3D simulations, initially 600 grains are randomly distributed in a cubic domain with the size of  $130 \times 130 \times 130$  grid points. The grid spacing between two adjacent grid points is  $1 \mu\text{m}$  and the interface thickness  $\eta$  is 4 cells. All grains have a cubic crystal structure, and they are distributed randomly through Voronoi tessellation. Periodic boundary conditions are used for each side of the domain in all simulations. In addition, all grain boundaries have the same grain boundary energy of  $1.0 \times 10^{-5} \text{ J/cm}^2$  and a nominal temperature of  $1000^\circ\text{C}$  is used in all simulations. Both grain boundary energy and temperature are formal parameters needed as MICRESS input but not of any physical significance.

#### **4.2.2 Critical disorientation angle**

Boundary mobility advantages can be introduced through setting a critical disorientation angle. Three Euler angles are used to define grain orientations in both 2D and 3D simulations, and a cubic 3D structure is assumed. Initially, a crystallographic orientation is assigned randomly to each grain such that each boundary can be characterized by a disorientation angle  $\theta$ . The percentage of boundaries with a specific disorientation angle is shown in Fig. 4.2. The y-axis in Fig. 4.2 is the number percentage of the fast grain boundaries. However, in Voronoi it doesn't matter as all grain boundary segments are of similar length.

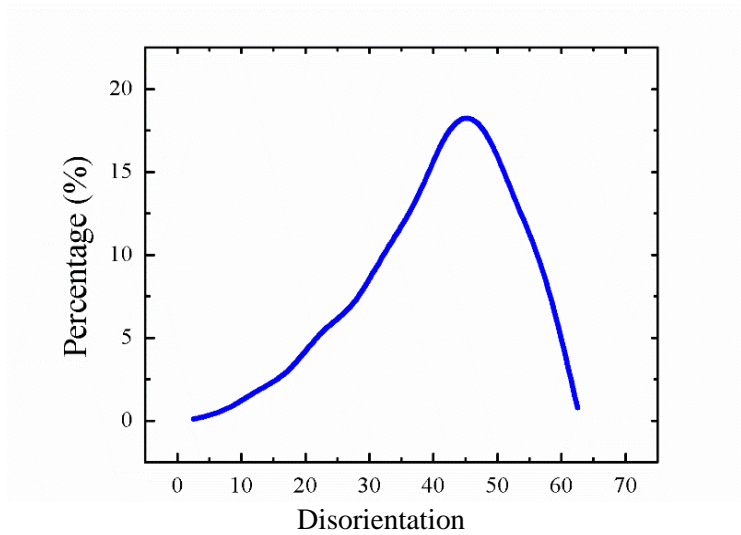


**Figure 4.2** The disorientation angle distribution of the initial microstructure.

The boundary mobility  $\mu$  is related to the disorientation angles between two adjacent grains, i.e. one can write the grain boundary mobility  $\mu$  as a function of the disorientation angle,  $\mu = \mu(\theta)$ . For convenience of description, in this research a simplified model is used as shown in Fig. 4.3. Here a critical disorientation angle, also called threshold angle,  $\theta_C$ , is introduced to select a certain amount of grain boundaries to be fast boundaries, i.e. boundaries with  $\theta > \theta_C$  are highly mobile. Here  $\mu_2$  is the high boundary mobility and  $\mu_1$  is the low boundary mobility. When the disorientation angle  $\theta$  is larger than  $\theta_C$ , the grain boundary mobility equals to  $\mu_2$ , and if the disorientation angle  $\theta$  is less than  $\theta_C$ , the grain boundary mobility equals to  $\mu_1$ . The value of  $\mu_2/\mu_1 = M$  is defined as the mobility ratio. The threshold angle is a numerical parameter which can be directly entered in the MICRESS input file. A complete MICRESS input script with threshold angle of  $40^\circ$  and mobility ratio of 1000 is attached in Appendix A.1.

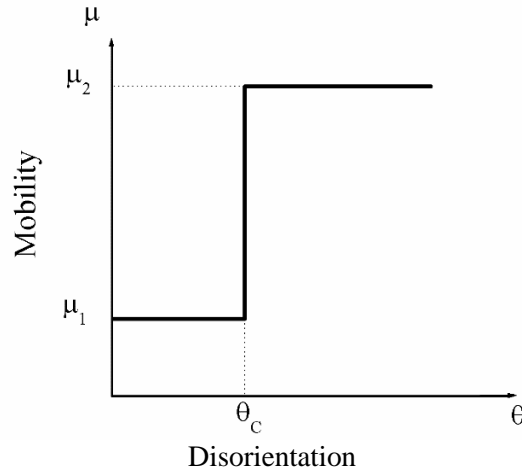


**Figure 4.3** Boundary mobility  $\mu$  as a function of disorientation angle in the threshold angle  $\theta_c$  approach.

After defining the threshold angle, one can construct the initial structures for both 2D and 3D simulations as illustrated in Fig. 4.4. The initial structure for 2D and 3D simulations are shown in Fig. 4.4 (a) and (b), respectively. Starting from the same initial structure, the only difference is either threshold angle or mobility ratio. For the reproducibility of the initial structure, an integer of randomization is used, which acts as a “random seed” for the microstructure initialization. When the same constant is assigned to this integer of randomization, MICRESS will output the same initial microstructure. For both 2D and 3D simulations, initially all grains have a similar grain size, i.e. a grain radius value of 20.0  $\mu\text{m}$  for both 2D and 3D simulations, and all grains are of the same phase. For the boundary mobility, first a constant  $5.0 \times 10^{-2} \text{ cm}^4/(\text{Js})$  is assigned to the mobility value  $\mu_2$  and then a pre-factor is used to define the value of  $\mu_1$ . For instance, if the mobility ratio is 1:1000, then 0.001 is entered as the pre-factor to define the low mobility value. The boundary mobility  $\mu_2$  is an independent numerical parameter directly inputted, as presented in Appendix A.1. A series of sensitivity tests have been done to prove that the initial grain size distribution is not sensitive to the geometry parameters, such as the minimal distance between two adjacent grains. The sensitivity analyses of minimal distance, radius range, and initial structure are attached

in Appendix B (i.e. Appendix B1 for minimal distance between grains, Appendix B2 for radius distribution range, and Appendix B4 for initial structure).

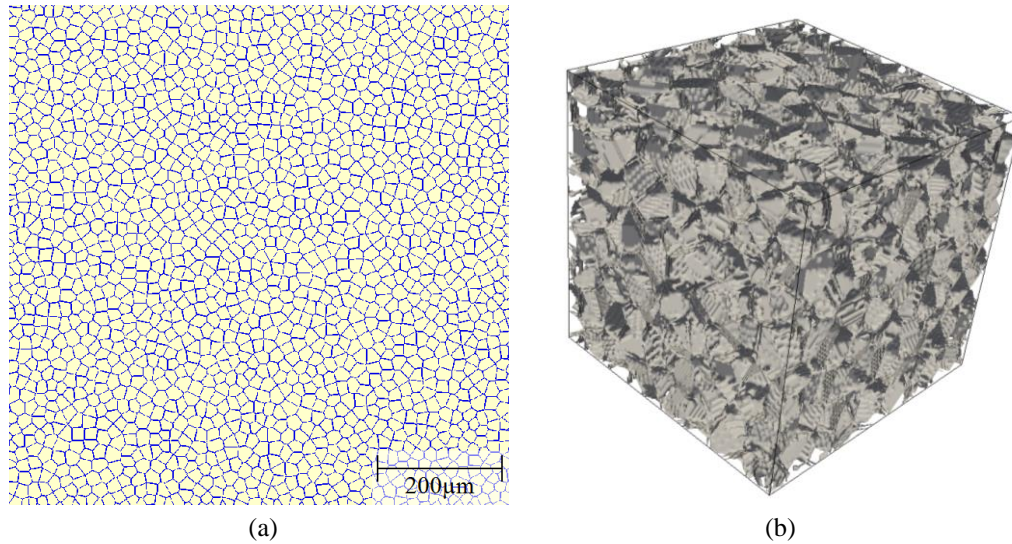


**Figure 4.4** The initial microstructure of (a) 2D simulation and (b) 3D simulation of the threshold angle approach.

### 4.2.3 Texture components

Apart from threshold angle, mobility advantages can also be introduced through different texture components. In this project, both two and three texture components are considered. When two texture components A and B are introduced, there will be three different types of grain boundaries – A-A, B-B and A-B boundary. Either A-A or A-B boundaries are selected to be fast mobile boundaries. Similarly, if one more texture component C is added, then there will be six types of grain boundaries, which are A-A, A-B, A-C, B-B, B-C and C-C boundaries. In this case, only A-B boundaries are defined as high mobility boundaries and all other boundaries are low mobility boundaries.

In MICRESS, texture components can be introduced as two extremely close phases, and mobility advantages are introduced through phase interaction data. Initially one can set two groups of grains and let them belong to two distinct solid phases (Phase A and Phase B). When setting the phase diagram, a negligible small value  $1.0 \times 10^{-7} \text{ J}/(\text{cm}^3\text{K})$  is assigned to the entropy of fusion between those two solid phases. In addition,  $1000^\circ\text{C}$  is used as the equilibrium temperature, since the microstructure evolution is simulated under the temperature of  $1000^\circ\text{C}$ . Consequently, those two phases have the same free energy, i.e.  $\Delta G_{AB} = 0$ , such that the governing phase field equation remains Eq. (4.3). With two extremely close phases in the system, there will be three types of phase interactions (A-A, A-B and B-B interactions). Thus we need to select three constants to be the grain boundary mobility values of the A-A, A-B and B-B phase interactions. These three constants are independent and directly entered into the input script, and there is no pre-factor introduced in the texture components approach. This method is also used to introduce mobility advantages in three-texture-component simulations as well as 3D simulations.

Another important aspect is how to position the two groups of grains in the initial structure. Here the situation of  $A\% = 20\%$  is used as an example for fast A-A boundary simulation in two texture component system. The two components A and B are represented with orange and white grains, respectively, as shown in Fig. 4.5. With 20% A grains in the system, the minimal distance between A grains,  $d_A$ , is set to  $38.5 \mu\text{m}$  while the minimal distance between B grains,  $d_B$ , is set to  $18.5 \mu\text{m}$ . If the same constant of  $25.0 \mu\text{m}$  is assigned to both grain A radius,  $r_A$ , and grain B radius,  $r_B$ , the resulting initial microstructure is shown in Fig. 4.5.

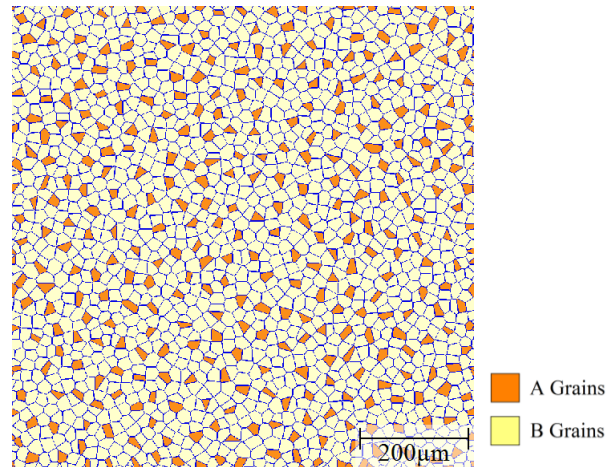


**Figure 4.5** The initial microstructure of A% = 20% with fast A-A grain boundaries, before adjustment,  $r_A = r_B = 25.0 \mu\text{m}$ .

The initial structure in Fig. 4.5 is not suitable as a starting microstructure, since most A grains are smaller than B grains and the shape of A grains is irregular with sharp corners. Therefore some adjustments are required to firstly make A and B grains of a similar size, and secondly make the shape of A grains more regular. When entering the same radius value ( $r_A = r_B = 25.0 \mu\text{m}$ ) into MICRESS, the output A grains are smaller than B grains. These limitations can be attributed to the setting-up methods used in MICRESS beyond users' availability. Therefore, to make the average grain size of A and B texture components match, one possible approach is increasing the numerical value of the A grain radius,  $r_A = 29.28 \mu\text{m}$ , meanwhile reducing the numerical value of the B grain radius,  $r_B = 24.0 \mu\text{m}$ . However, if only the grain radius value is modified, the morphology of A grains is still rather artificial. As shown in Fig. 4.6(a), there are some sharp corners, and even some small round B grains exist within A grains. To optimize the morphology of A grains, a small time step of 1.5s is run with all grain boundary mobility values being the same. After making these modifications, the microstructure is shown in Fig. 4.6(b). In Fig. 4.6(b), both A grains and B grains have a similar grain size and the shape of the A grains are much more regular. Therefore, microstructure in Fig. 4.6(b) can be used as an initial microstructure for the

following simulations. The input script of 20% A grains in the initial structure with mobility ratio of 100 is attached in Appendix A.2.

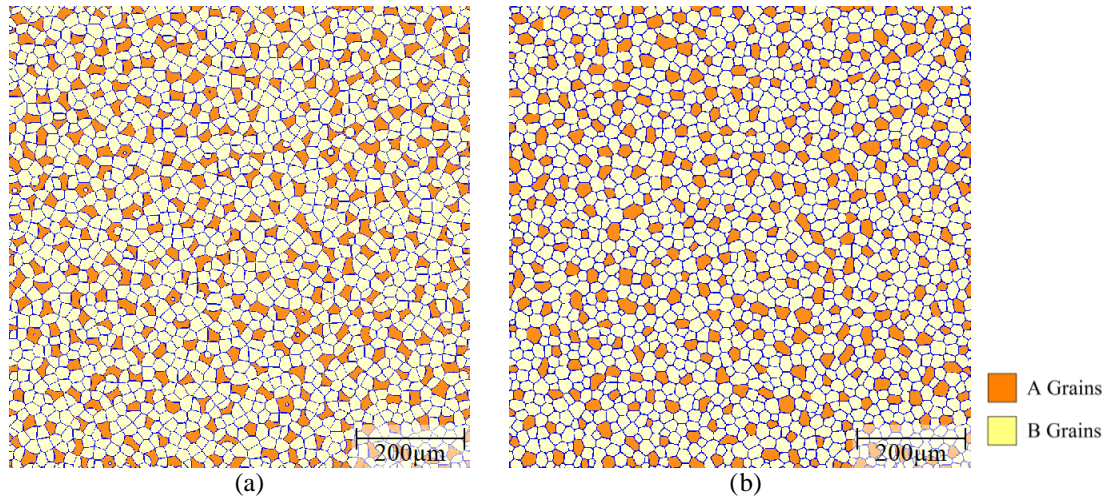


**Figure 4.6** The initial microstructure with 20% A grains after adjustment ( $r_A = 29.28 \mu\text{m}$  and  $r_B = 24.0 \mu\text{m}$ ).  
 (a) Before a small time step annealing; (b) after a small time step annealing.

For the two texture components simulations with A-B boundary fast, the situation of 2% B grains in 98% A grains matrix is used as an example. The two components A and B are represented with white and orange grains, respectively, as shown in Fig. 4.7. The B grains are randomly distributed in the A grain matrix and there are no two B grains adjacent to each other. With 2% B grains in the system, the minimal distance between B grains,  $d_B$ , is set to  $100.0 \mu\text{m}$  while the minimal distance between A grains,  $d_A$ , is set to  $16.6\mu\text{m}$ . If the same constant of  $25.0 \mu\text{m}$  is assigned to both  $r_A$  and  $r_B$ , the resulting initial microstructure is shown in Fig. 4.7.

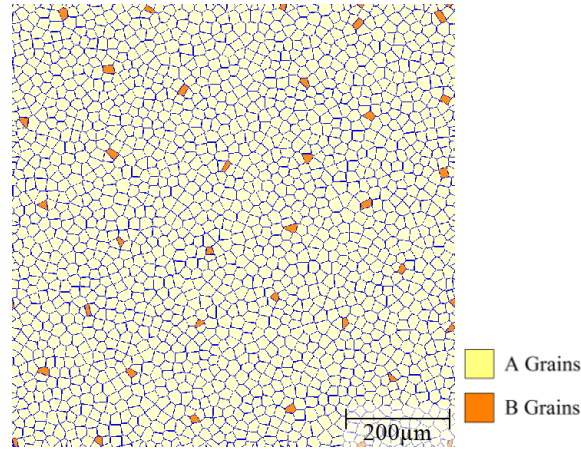


**Figure 4.7** The initial microstructure of 2% B grains in A grains matrix before adjustment,  $r_A = r_B = 25.0 \mu\text{m}$ .

The initial structure in Fig. 4.7 is not suitable as a starting microstructure, since most B grains are smaller than A grains and the shape of B grains is irregular with sharp corners. After increasing the numerical value of the B grain radius,  $r_B = 26.6 \mu\text{m}$  and reducing the numerical value of the A grain radius,  $r_A = 20.0 \mu\text{m}$ , as shown in Fig. 4.8(a), the morphology of B grains is still rather artificial with some small round A grains exist within B grains. To optimize the morphology of B grains, a small time step of 1.5s is run with all grain boundary mobility values being the same. After making those modifications, the microstructure is shown in Fig. 4.8(b). In Fig. 4.8(b), both A grains and B grains have a similar grain size and the shape of the B grains are much more regular. Therefore, microstructure in Fig. 4.8(b) can be used as an initial microstructure for the following simulations. The input script of 2% B grains in the initial structure with mobility ratio of 1000 is attached in Appendix A.3. The sensitivity analyses of minimal distance, radius range and radius ratio are attached in Appendix B (i.e. Appendix B1 for minimal distance between grains, Appendix B2 for radius distribution range, and Appendix B3 for radius ratio).

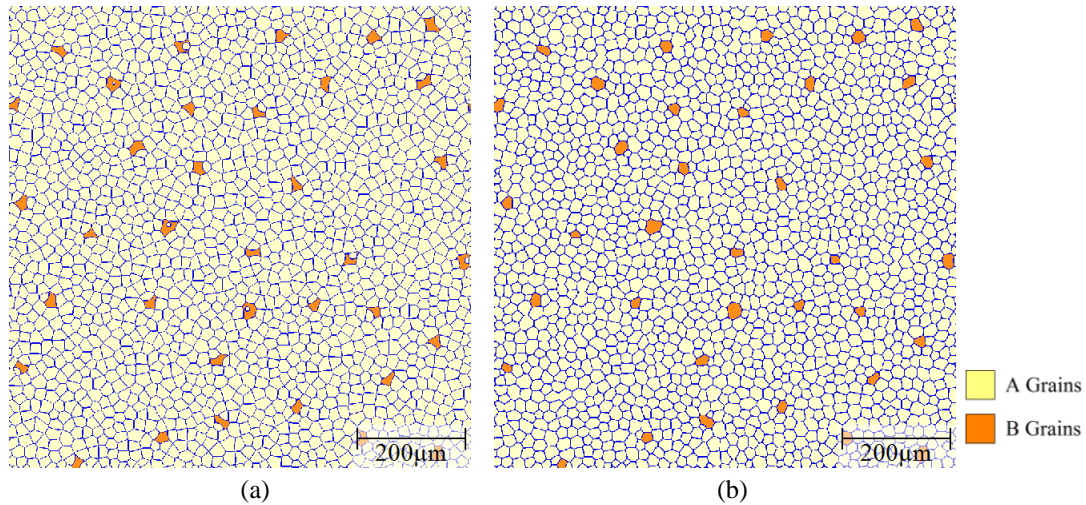


**Figure 4.8** The initial microstructure of 2% B grains in A grains matrix after adjustment ( $r_A = 20.0 \mu\text{m}$  and  $r_B = 26.6 \mu\text{m}$ ). (a) Before a small time step annealing; (b) after a small time step annealing.

When there are only two texture components in the system with a small fraction of B components, initially all B grains are surrounded by fast mobile boundaries. However, if another texture component C is introduced, then only a part of the B grain boundaries is fast mobile boundaries. As shown in Fig. 4.9, the red grains represent B texture components; orange and white grains are defined as A and C texture components. The situation of  $B=1\%$  is used as an example to describe the initialization of three texture components. In the beginning, 18 B grains, 891 A grains and 891 C grains ( $B = 1\%$ ,  $A \% = C \% = 49.5\%$ ) are randomly distributed in a large square domain. A value of  $205.0 \mu\text{m}$  is assigned to  $d_B$  to create a sufficient large distance between two B grains. The distance between A-A grains and C-C grains are equal ( $d_A = d_C = 22.0 \mu\text{m}$ ). Since only A-B boundaries are chosen to be fast boundaries, therefore a value of  $5.0 \text{ cm}^4/(\text{Js})$  is assigned to the mobility of the A-B phase interaction. All the other phase interactions (A-A, A-C, B-B, B-C, C-C phase interactions) have the same but small mobility value, i.e.  $5.0 \times 10^{-3} \text{ cm}^4/(\text{Js})$  for a mobility value of 1000.

A similar modification method as for the A-B texture components system has been applied to produce a proper initial microstructure for three texture components simulations. Modified grain radius parameters ( $r_A = 24.1 \mu\text{m}$ ,  $r_B = 28.42 \mu\text{m}$ ,  $r_C = 24.0 \mu\text{m}$ ) are entered into the MICRESS input file so that MICRESS will output grains with a similar grain size for all texture components. Before annealing, some irregular B grains with sharp corners exist in the microstructure, as shown in Fig. 4.9(a). After running a small step of 1.5s with the same mobility value of  $5.0 \times 10^{-4} \text{ cm}^4/(\text{Js})$  for all grain boundaries, the output microstructure is illustrated in Fig. 4.9(b). After annealing, the sharp corners of B grains are annealed out, and the shape of B grains is much more regular, meanwhile all grains are of a similar size. Thus the microstructure in Fig. 4.9(b) can be used as a starting point for the following three-texture-component simulations.

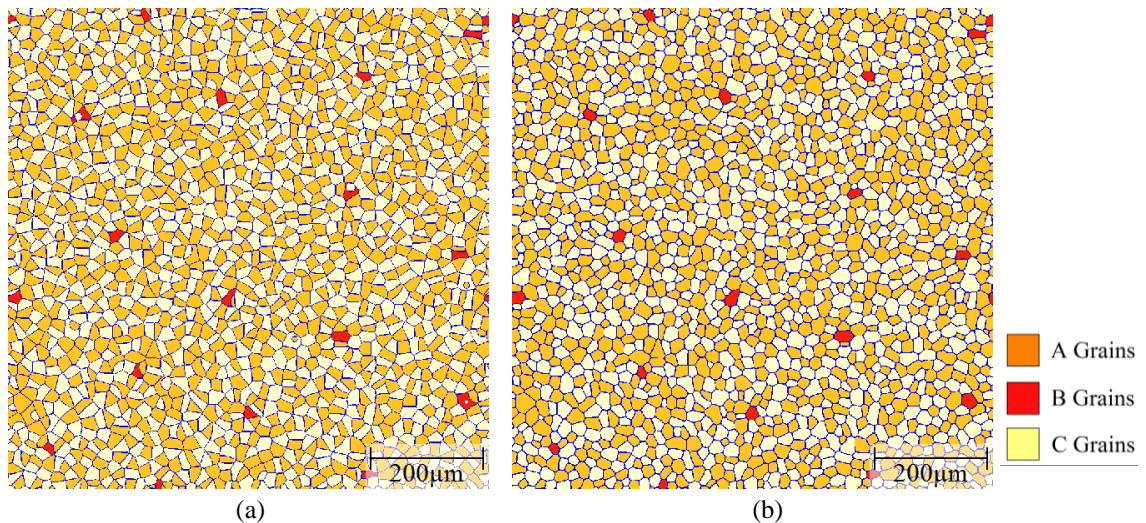


**Figure 4.9** The initial microstructure of 1% B grains in A, C grains matrix ( $A\% = C\% = 49.5\%$ )

The three-texture-component simulations in the large domain are relatively time-consuming. To improve the simulation efficiency, a smaller 2D domain is used to study the behavior of a selected B grain that can grow. In the smaller domain, only one candidate B grain is placed in domain and surrounded by both A grains and C grains. The situation of  $A\% = C\% = 49.5\%$  is used as an

example to describe the initialization of small domain simulations. Initially, some size advantage is given to the B grain through setting a large grain B radius value,  $r_B = 41.0 \mu\text{m}$ , to promote the growth of the B grain. The radius of A and C grains are  $32.0 \mu\text{m}$  and  $32.18 \mu\text{m}$ , respectively; the distance between A-A grains and C-C grains are both  $35.0 \mu\text{m}$  ( $d_A = d_C = 35.0 \mu\text{m}$ ). In order to anneal out the irregular shapes, a short-time simulation of 1.5s is run with all grain boundary mobility values being the same. All the other simulation settings are the same as previously described for large domain simulations. By changing the integer of randomization, one can construct a series of initial microstructures with different morphologies. One possible initial microstructure is shown in Fig. 4.10. The input script of this situation is attached in Appendix A.4.

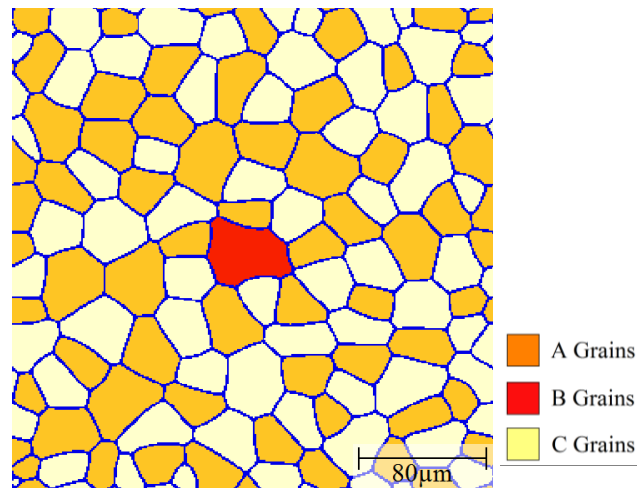


**Figure 4.10** The initial microstructure of one B grain in the matrix of A,C grains ( $A\% = C\% = 49.5\%$ )

Further some 3D simulations are performed to verify the 2D simulation results of two texture components. When setting up 3D simulations in two texture components system, two groups of grains (A and B grains) are randomly distributed in the cubic domain. Modified grain radius parameters ( $r_A = 19.0 \mu\text{m}$ ,  $r_B = 22.0 \mu\text{m}$ ) are entered into the MICRESS input script so that

MICRESS will output grains with a similar grain volume for both texture components. The minimal distance between A-A grains and B-B grains are 14.0  $\mu\text{m}$  and 70.0  $\mu\text{m}$ , respectively, for B% = 2%. A-B grain boundaries have a higher mobility value of  $5.0 \times 10^{-2} \text{ cm}^4/(\text{Js})$  while all the other grain boundaries have a lower mobility value, e.g.  $5.0 \times 10^{-4} \text{ cm}^4/(\text{Js})$ . All the other simulation settings are the same as in the 2D two components simulations. A short-time annealing has been applied to improve the initial morphology. After annealing, the initial 3D structure is shown in Fig. 4.11.

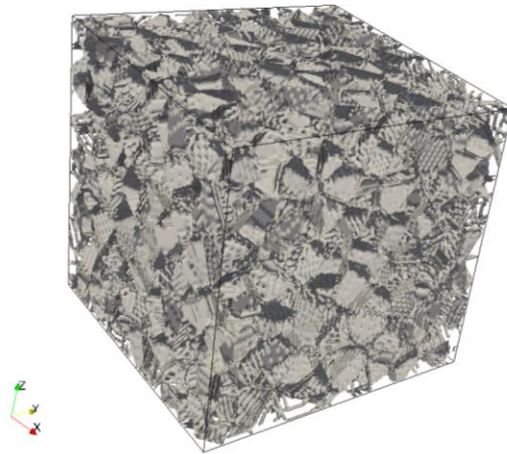


**Figure 4.11** The 3D initial microstructure of the two texture components system.

### **4.3 Sensitivity analysis**

#### **4.3.1 Normal grain growth**

To verify the accuracy of MICRESS simulations, the shrinkage of a single round grain is studied. Initially one circular grain is located in the center of the domain, and this grain will shrink and gradually disappear. The shrinkage rate of one round grain with radius R follows the parabolic rule, i.e. [62]

$$R^2 - R_0^2 = \mu\sigma kt \quad (4.4)$$

Here  $R_0$  is the initial grain size and  $k$  is a constant. Fig. 4.12 shows the evolution of  $R^2$  with time as obtained in the MICRESS simulation confirming the linear relationship according to Eq. 4.4.

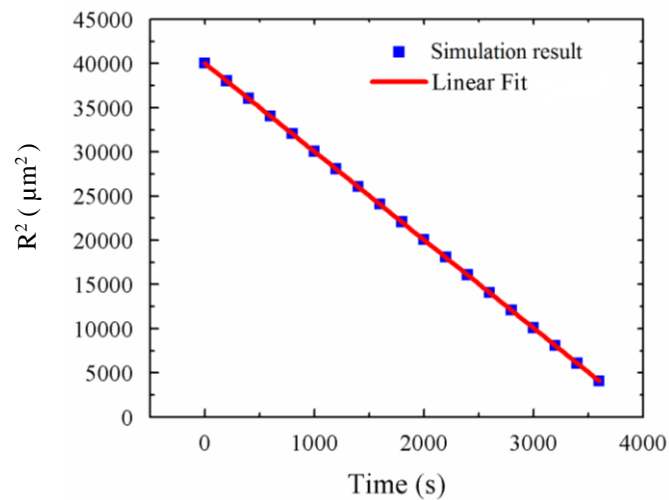


**Figure 4.12** Evolution of  $R^2$  for shrinkage of one single grain.

Another benchmark simulation is the normal ideal grain growth starting from a polycrystalline structure assuming that all grain boundaries have the same mobility and energy. Ideal grain growth of a multi-grain structure follows the parabolic rule as well for the average equivalent area radius,  $\bar{R}$ . MICRESS simulated the normal grain growth of initially 5000 grains. The time evolution of  $R^2$  and the linear fitting results are illustrated in Fig. 4.13(a). When the simulation time is 500s, there is a small deviation from the parabolic law. This small deviation in the early stage is related to the narrow size distribution resulting from Voronoi tessellation. To demonstrate the grain growth model in early stage more clearly, a corresponding grain size distribution is plotted in Fig. 4.13(b).

Within the first 1000s, the grain size distribution is transferring from the initial narrow distribution to the stable scaling distribution. This transfer process will exert a small deviation from the parabolic growth law; however, the initial period has little significance for the long-term grain growth behavior. Therefore, MICRESS can be used as a simulation tool to evaluate the more complex situations with mobility advantages of selected grain boundaries.

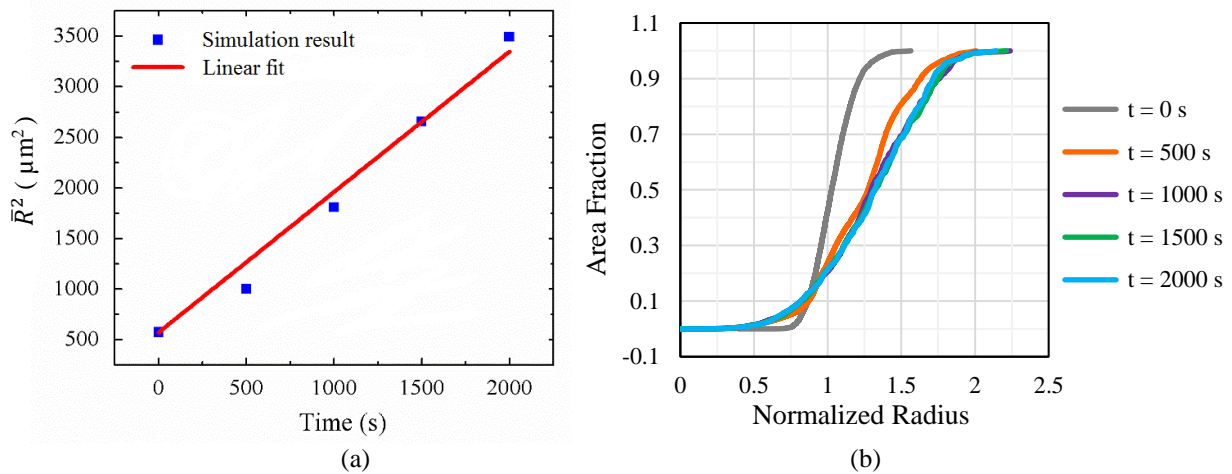


**Figure 4.13** Ideal grain growth in a multi-grain structure: (a) Evolution of  $\bar{R}^2$ ; (b) Grain size distribution at different simulation times.

### 4.3.2 Sensitivity analysis of time step

In multi-phase field simulations, one of the important numerical parameters is time step. Typically, automatic time stepping is chosen in MICRESS for numeric efficiency. Here, the results of automatic time stepping and fixed time steps are compared for NGG. Initially, there are 5000 grains in the domain for which normal grain growth occurs. The only difference between these two simulations is that one is using automatic time steps while in the other simulation time steps are set to be 0.02s. All the other simulation settings are the same. The time evolution of  $\bar{R}^2$  in both simulations is compared in Fig. 4.14 verifying that the results are independent of the time step

selection. Similarly, the cumulative grain size distribution curves are essentially the same in both simulations.

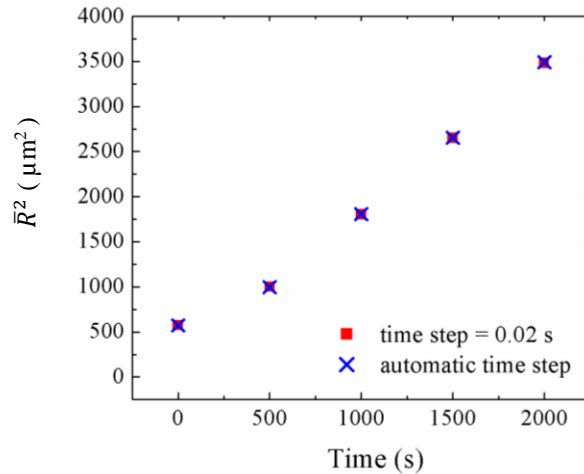


**Figure 4.14** Time evolution of  $\bar{R}^2$  using automatic time step and fixed time step of 0.02s.

### 4.3.3 Sensitivity analysis of anisotropic structure

After assigning each grain a crystallographic orientation or introducing texture components, one might want to know whether these additional attributes will influence the normal grain growth behavior. To verify the effect of crystallographic orientations, the simulations of ideal grain growth are compared in Fig. 4.15(a) with the simulation results shown in Fig. 4.13(a) for grains with random crystallographic orientations but the same boundary mobility. Using the same method, setting the grain boundary mobility being the same for all grain boundaries, simulations of grain growth with and without texture components are conducted as well. The time evolution of  $\bar{R}^2$  and, as an example, the cumulative grain size distribution curves after 2000s are presented in Figs. 4.15 (b) and (c), respectively. Clearly, the results for these three grain growth simulations are the same confirming that introducing different grain types through crystallographic orientations or texture

components does not affect the normal grain growth behavior when all grain boundaries have otherwise the same properties.

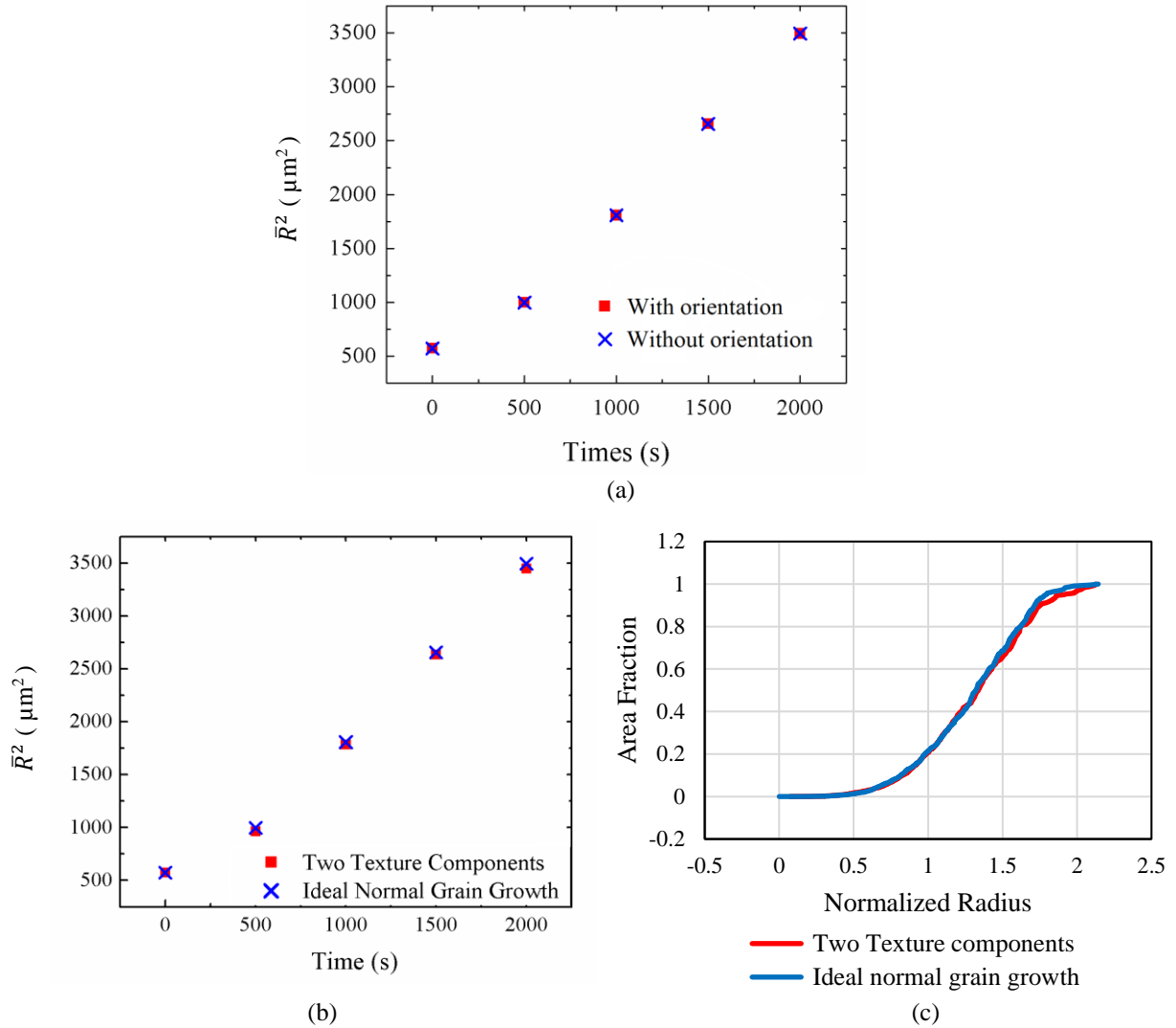


**Figure 4.15** The time evolution of  $\bar{R}^2$  for grain structure (a) with and without crystallographic orientations; (b) with and without texture components; (c) grain size distribution at 2000s with and without texture components.

#### **4.4 Post data processing**

A series of computational tools have been used for post data processing. Display MICRESS software is used to visualize 2D microstructure evolution while ParaView software is employed in displaying 3D simulation results. Apart from microstructure visualization, TSL OIM Analysis software, also used in EBSD processing, is employed to highlight the high mobility boundaries. Python is chosen to write a data conversion code between MICRESS and the TSL OIM Analysis software. Excel is employed to perform data analysis and Origin is used to plot graphs to present data analysis results.

## Chapter 5: Results and discussion

### 5.1 Mobility advantages through critical disorientation angle

As shown in Fig. 4.2, introducing a threshold angle leads to a particular fraction of fast boundaries, e.g. 42% of the boundaries are highly mobile for a threshold angle of  $40^\circ$ . Figs. 5.1(a-d) show the evolution of the grain structure when the threshold angle is  $40^\circ$  and the mobility ratio is 1000, with highlighting the fast boundary in green lines and slow boundaries in red lines. Initially, Fig. 5.1(a), all grains are of a similar size with around 42% green fast mobile boundaries. After 50 s, in Fig. 5.1(b), several grains start to show some size advantages. Slow-growing grains have essentially more than 90% low mobility boundaries whereas those fast-growing grains, e.g. grains M and N, have more than 50% high mobility boundaries. After 190s, in Fig. 5.1(c), the percentage of high mobility boundaries decreases significantly. Meanwhile the size advantage of N and M grains has further increased as these grains have comparatively rapidly consumed their much smaller neighboring grains. In grain M an island grain has formed, which is a characteristic sign of AGG, and all grain boundaries surrounding the island grain are red slow mobile boundaries. After 500 s, Fig. 5.1(d), the fraction of fast mobile boundaries has further decreased. In addition, N and M grains have, at least to some extent, lost their size advantage and the grain structure starts to approach that of a normal grain size distribution.

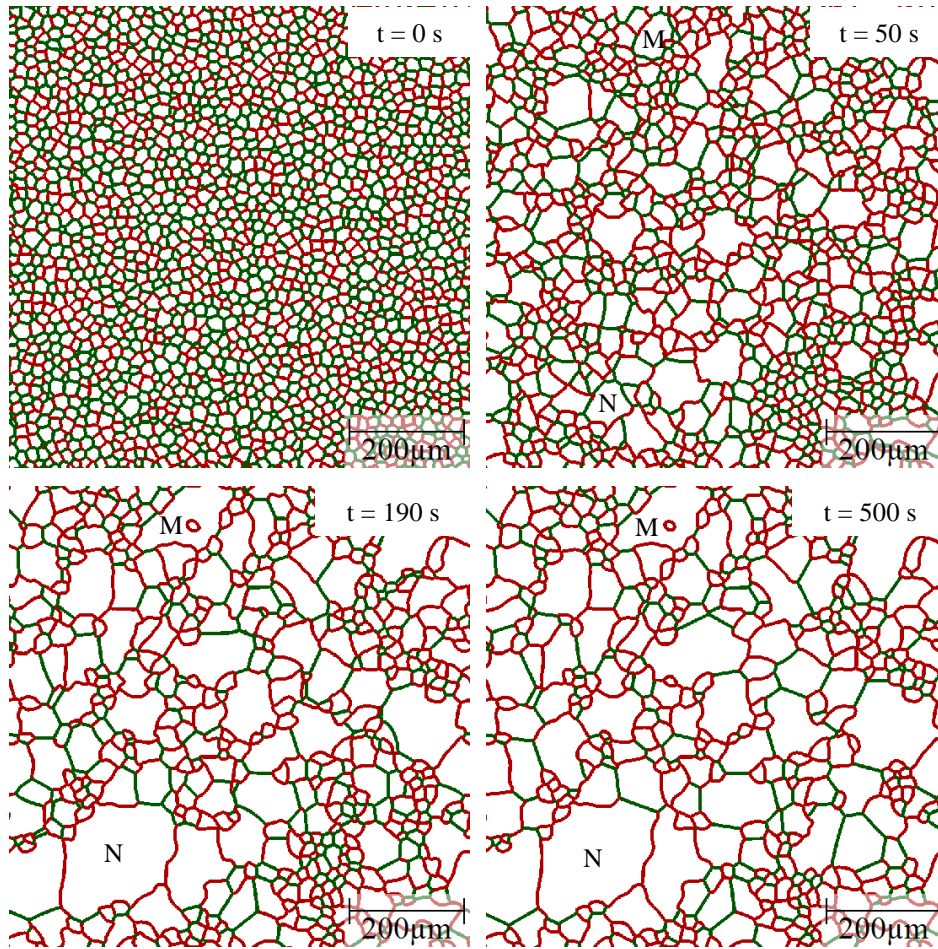


**Figure 5.1** Evolution of 2D grain structure for  $\mu_2/\mu_1 = 1000$  and  $\theta_c = 40^\circ$ , highlighted fast boundaries from slow boundaries.

To more quantitatively analyze the changes in the grain structure with time including AGG stages, the evolution of the cumulative grain area distribution is shown in Fig. 5.2 as a function of the normalized grain diameter. From the grain area, the equivalent area diameter (EQAD) of each grain is determined. The mean EQAD is obtained from the mean grain area while the normalized diameter of a grain is introduced as its EQAD divided by the mean EQAD. The red curve provides as reference the cumulative area distribution of normal grain growth that is obtained when all boundaries have the same mobility (mobility ratio of 1). Since normal grain growth is a self-similar process, the red curve represents the resulting scaling distribution where the maximum EQAD is

about twice as large as the mean EQAD. The scaling distribution is used as a benchmark to measure the abnormality. Initially, the grain area distribution resulting from Voronoi tessellation is much narrower than the scaling distribution but quickly broadens and its width surpasses that of the scaling distribution. After 50 s the maximum EQAD (i.e. that of grain N) is about 3.5 times larger than the mean EQAD. The maximum normalized diameter increases further to 6 at 190 s before it starts to decrease towards a value of 5 for larger times. Thus, there is a particular time (or time period) where the grain area distribution has its broadest range and the maximum normalized diameter obtained for this situation may be taken to assess the abnormality of grain growth for the selected grain growth parameters, i.e. threshold angle and mobility ratio. Therefore, one can find the widest distribution curve for each scenario to quantify the degree of AGG.

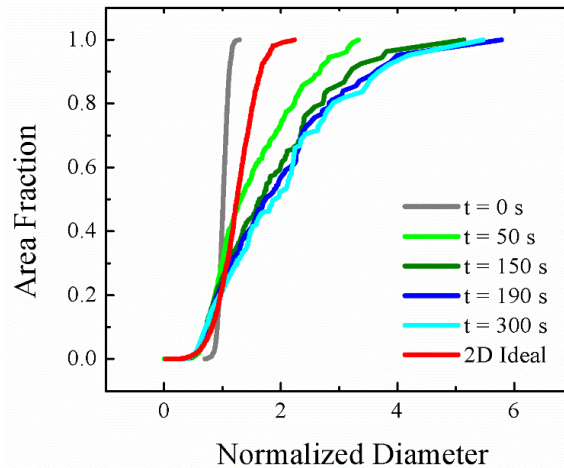


**Figure 5.2** Time evolution of cumulative grain area distribution. ( $\mu_2/\mu_1 = 1000$  and  $\theta_c = 40^\circ$ ).

The above described scenario does show indication of AGG that is based on the presence of one or a few fast-growing grains. To analyze the statistical significance of these simulations, it is thus important to re-evaluate AGG starting from different initial structures, where the grain distribution and the crystallographic orientations of each grain are both changed whereas the average mean

grain size is kept the same. The widest distribution curves resulting from a range of initial structures are shown in Fig. 5.3(a) where the maximum EQAD is varying from 3.5 to 6. With the same amount of high mobile boundaries, their relative positions significantly affect the extent of AGG. Fig. 5.3 (b-d) show examples of grain structures with the widest grain size distributions and maximum EQADs of about 6, 5, and 4 in units of the normalized diameter. While Fig. 5.3 (b) and (c) show cases with at least one abnormal grain, such a grain cannot be observed in Fig. 5.3 (d). This further illustrates that AGG is a rather rare event for the present mobility scenario. For a grain to grow abnormally a sustained mobility advantage is required that for the investigated threshold angle case can only be attained for a few grains and a limited time period.

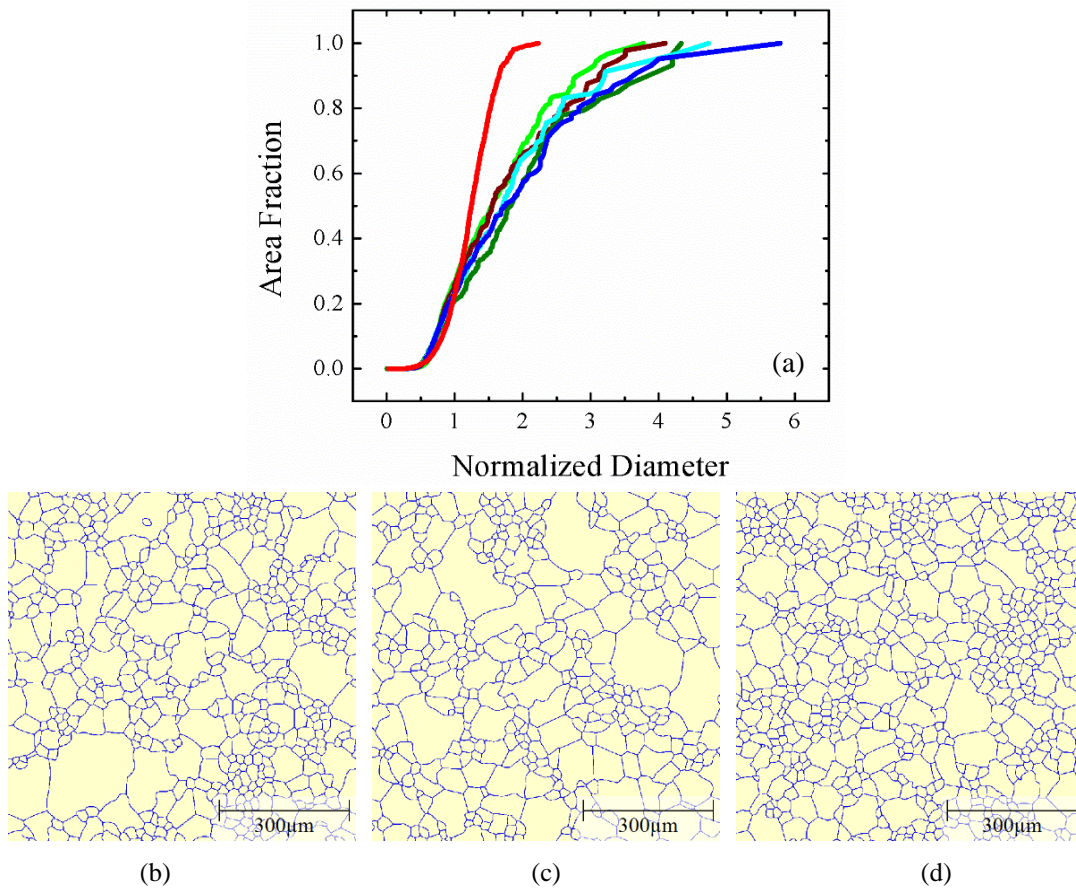


**Figure 5.3** (a) Cumulative grain area distribution and (b-d) grain structures for the widest grain size distributions for different initial structures when  $\theta_c = 40^\circ$  and  $\mu_2/\mu_1 = 1000$ .

To quantify the role of threshold angle and mobility ratio on AGG, we select the initial structure of the above case with the most pronounced AGG structure for a parametric study. The widest distribution curves of each scenario are presented in Figs. 5.4 (a) and (b) to show the effect of threshold angle and mobility ratio, respectively, on growth abnormality. When changing the threshold angle from  $20^\circ$  to  $50^\circ$ , according to Fig. 5.4(a) it is easy to see that for a threshold angle in the range of  $40^\circ - 44^\circ$  the widest grain size distributions are obtained. This comparatively narrow range of threshold angles leads for a mobility ratio of 100 to a maximum normalized diameter of 5 which can be considered as an abnormal grain structure whereas threshold angles of  $30^\circ$  and  $50^\circ$ , respectively, lead to much narrower distributions with a maximum normalized diameter of about 3, i.e. a grain structure that approaches that of normal grain growth. Similarly, when changing the mobility ratio from 5 to 1000 for a threshold angle of  $40^\circ$ , one can conclude from Fig. 5.4(b) that when the mobility ratio is 10 or less, grain growth does not occur abnormally since the distribution curves are sufficiently close to that for normal grain growth. Mobility ratios above 50 lead to AGG where the severity of AGG is augmented when increasing the mobility ratio from 100 to 1000 as the associated maximum normalized diameter increases from 5 to 6.

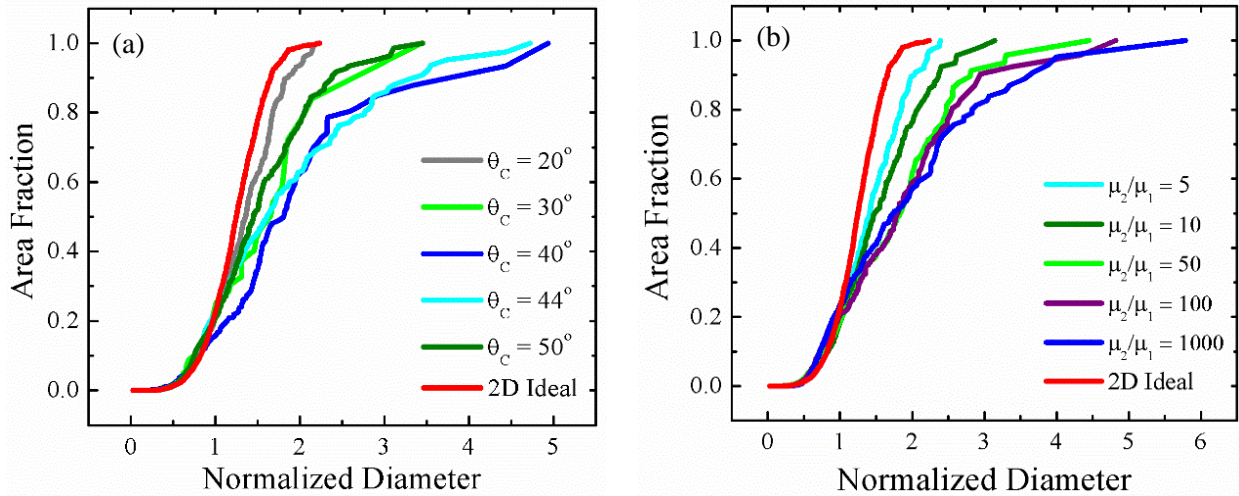


**Figure 5.4** Cumulative grain area distribution for the widest grain size distributions: (a) Effect of threshold angle when  $\mu_2/\mu_1 = 100$ ; (b) Effect of mobility ratio when  $\theta_c = 40^\circ$ .

The influence of mobility ratio is further illustrated in Fig. 5.5 by comparing the most abnormal grain structure images. For a mobility ratio of 10, there are no obvious grain size advantages and no tendency of island grain formation. However, if the mobility ratio is increased to 100, grain N has a clear size advantage over the other grains and the size advantage of grain N becomes even more pronounced when the mobility ratio is further increased to 1000. Meanwhile, with a mobility ratio of 100, grain M shows a tendency to embrace one of its small neighbor grains but an island grain is not formed yet. If the mobility ratio is further increased to 1000, there is an island grain formed within grain M.

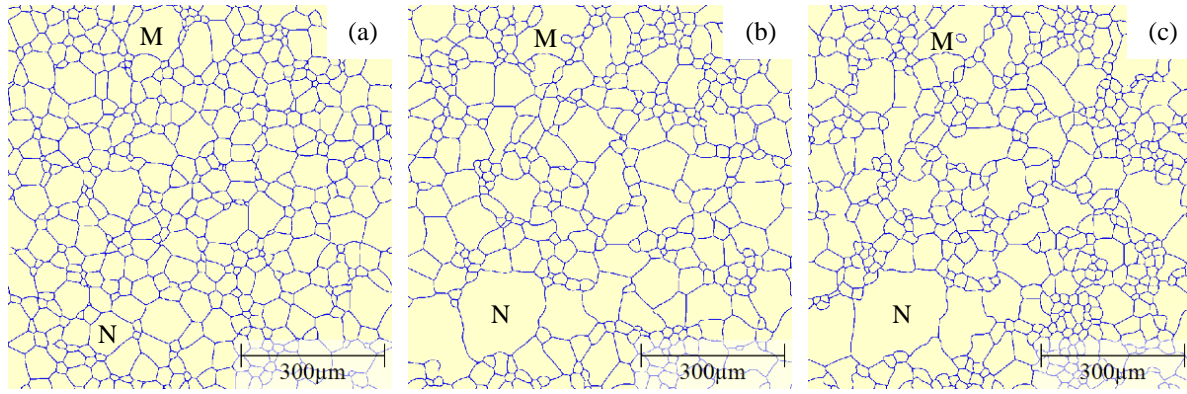


**Figure 5.5** 2D grain structure for the widest grain size distribution when  $\theta_c = 40^\circ$  and (a)  $\mu_2/\mu_1 = 10$ ; (b)  $\mu_2/\mu_1 = 100$ ; (c)  $\mu_2/\mu_1 = 1000$ .

Based on the 2D simulation results, one can further extend the simulations into 3D scale. Setting the threshold angle to  $45^\circ$ , Fig. 5.6 compares the results for mobility ratio changing from 10 to 1000. The 3D cubic microstructure after 110s is shown in Fig. 5.6(a) while corresponding 2D cross section images are presented in Fig. 5.6(b) for the mobility ratio of 1000. It is noteworthy that the large blue regions in 2D cross sections images, i.e. Figs. 5.6(b) and (d), mean that the grain boundary is parallel to the cutting plane. The grain K in Figs. 5.6 (a) and (b) is obviously much larger than its surrounding matrix grains. Thus when  $t=110s$ , the microstructure shows some degree of abnormality. This is more convincing when looking at the time evolution graph as presented in Fig. 5.7(a). After 110s the maximum EQAD is about 4 times larger than the mean EQAD. Therefore, under this conditions ( $\mu_2/\mu_1 = 1000, \theta_c = 45^\circ$ ) AGG is very likely to occur. However, if starting from the same initial structure but reducing the mobility ratio to 10, the situation is different. Fig. 5.6(c) illustrates the 3D cubic microstructure after 15 s with a mobility ratio of 10, and its 2D cross sections images are shown in Fig. 5.6(d). The grains are of a similar size and there are no obvious size advantages, as illustrated with the cumulative volume distribution curves in Fig. 5.7(b), i.e. a mobility ratio of 10 is too small for AGG to occur. The 3D simulation results are consistent with the previous 2D simulation results.

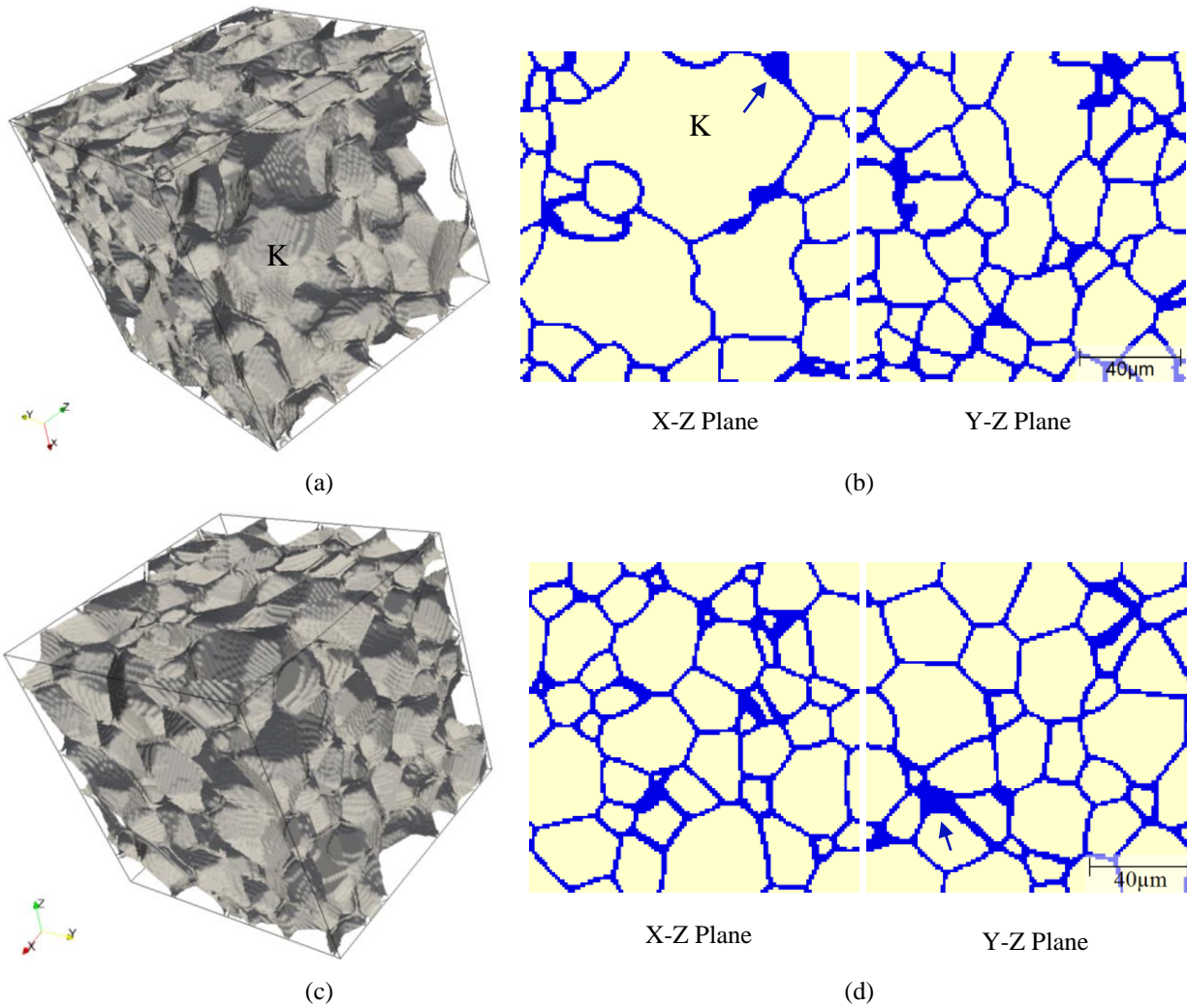


**Figure 5.6** The 3D grain structure (a) and the cross section (b) when  $\mu_2/\mu_1 = 1000$  and  $\theta_c = 45^\circ$ . The 3D grain structure (c) and the cross section (d) when  $\mu_2/\mu_1 = 10$  and  $\theta_c = 45^\circ$ .

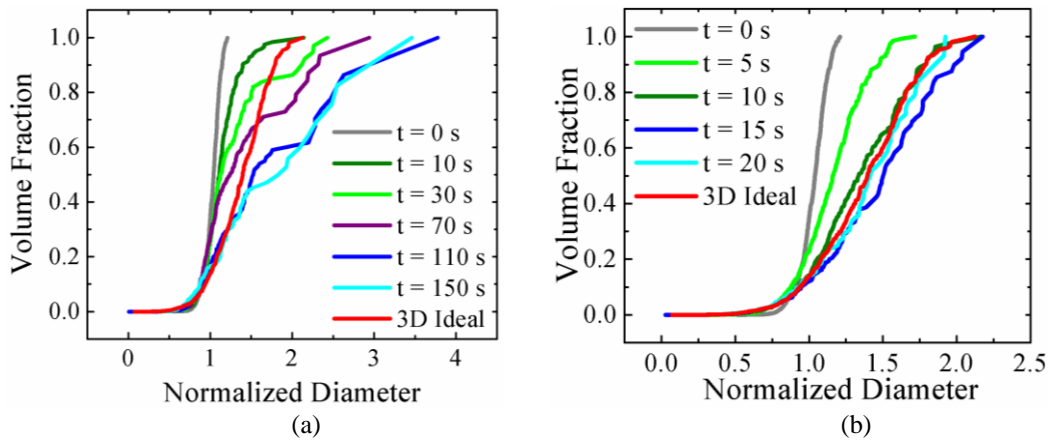


**Figure 5.7** Time evolution of cumulative grain area distribution for 3D simulations setting  $\theta_c = 45^\circ$ : (a)  $\mu_2/\mu_1 = 1000$ ; (b)  $\mu_2/\mu_1 = 10$ .

## 5.2 Mobility advantages in two grain type systems

### 5.2.1 Fast A-A boundaries

Another method to introduce a mobility advantage is through different grain types or texture components. Different grain types are introduced to get different grain boundaries that can subsequently be assigned different mobility values. The A-A boundaries are taken as highly mobile and their fraction is then determined by the fraction of A grains in the initial microstructure. This initial fraction of A grains cannot be too low, since A grains must have A neighbors to obtain highly mobile A-A boundaries. The situation of initially 50% A grains in the system with mobility ratio of 100 is used as an example, and the simulation results are shown in Fig. 5.8. Here, the two components A and B are represented with orange and white grains, respectively. In the beginning when  $t=0$ s in Fig. 5.8(a), all grains have a similar size and the number of A-A fast boundaries is sufficient for some A grains to grow rapidly. After 50s, several A grains, for example grain P in Fig. 5.8(b), start to show a slight size advantage. Since only A-A boundaries are fast mobile boundaries and both A-B and B-B boundaries are low mobility boundaries, several larger A grains will consume their smaller neighboring A grains. Then A grains with their size advantages will coarsen at the expense of B grains in the system. This is clearly seen after 100s in Fig. 5.8(c); some A grains, e.g. grain P, keep growing while the fraction of white B grain drops significantly. The size advantages of grain P is remarkable after 200s in Fig. 5.8(d) and later on the A grains will gradually consume all B grains because of the large driving pressure (size advantages between large A grains and small B grains).

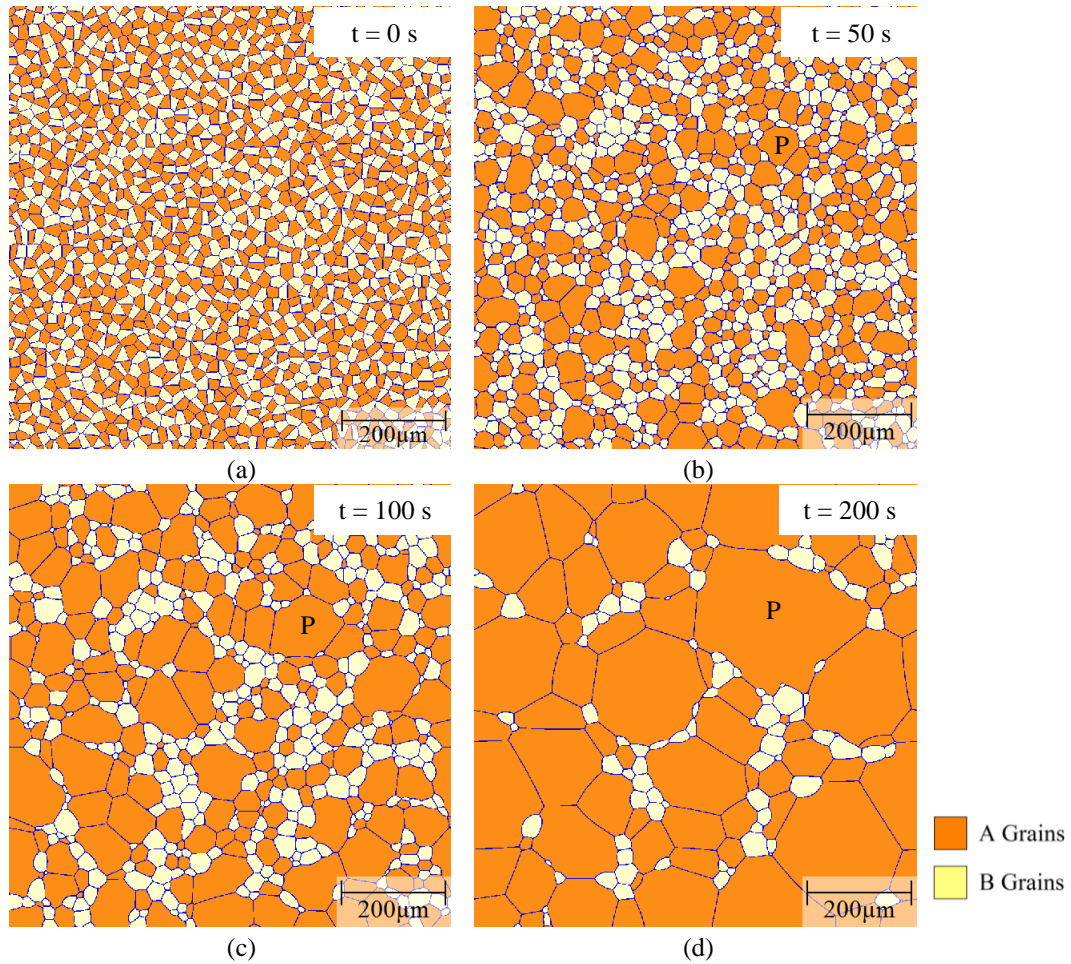


**Figure 5.8** Microstructure evolution of A-B system with fast A-A boundaries when  $\mu_2/\mu_1 = 100$  and 50% A grains in the initial structure.

For a quantitative analysis, Fig. 5.9 provides the time evolution of the cumulative grain area distribution as a function of normalized diameter to further evaluate the AGG. The red curve is the scaling distribution of 2D ideal grain growth as a reference. The initial grain size distribution results from Voronoi tessellation and is very narrow since both A and B grains have a similar size. After 100 s the maximum EQAD (i.e. that of grain P) is nearly 4.5 times larger than the mean EQAD. The maximum normalized diameter increases further to 5.5 after 200s before it starts to decrease towards a value of 4 for longer times. In this scenario the maximum EQAD is larger than 5, the threshold for AGG, therefore AGG may occur when the initial grain A percentage is 50%.

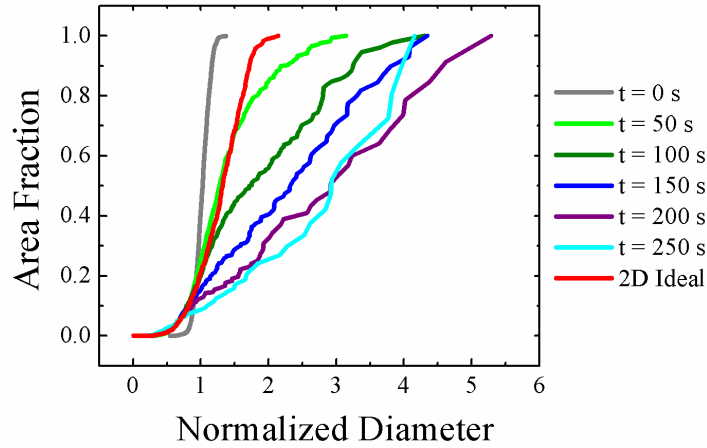


**Figure 5.9** Time evolution of cumulative grain area distribution in the A-B system with fast A-A boundaries. ( $\mu_2/\mu_1 = 100$ , A % = 50 %).

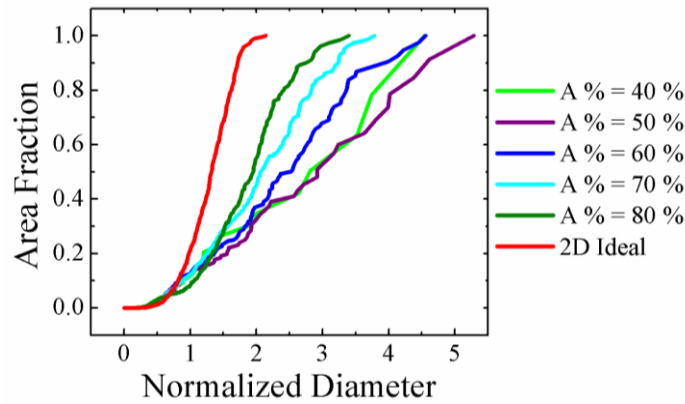


**Figure 5.10** Widest area distribution curves in A-B system to investigate the influence of initial A grain percentage when  $\mu_2/\mu_1 = 100$ .

The effect of the initial fraction of A grains on the widest grain size distribution is presented in Fig. 5.10. The mobility ratio is set to be 100 and the initial area percentage of A grains varies from 40% to 80%, in 10% increments. One can see in Fig. 5.10 that when the initial percentage of A grains is either 40% or 60%, the maximum EQAD is 4.5 times larger than the mean EQAD. When the percentage of initial A grains is relatively low (i.e., 40% or less) or relatively high (i.e., 60% or higher) the maximum EQAD is smaller than the threshold value 5. The maximum EQAD is larger than 5 only when the initial A grains fraction is 50%. This is related to the fact that changing

the fraction of A grains will influence the amount of fast mobile A-A boundaries in the system. This means that too many or too few fast boundaries do not lead to AGG. On the other hand, the 2D simulation results show that AGG is most likely to occur if only an appropriate amount of fast boundaries exists in the system. This situation is similar to the threshold angle approach described in section 5.1.

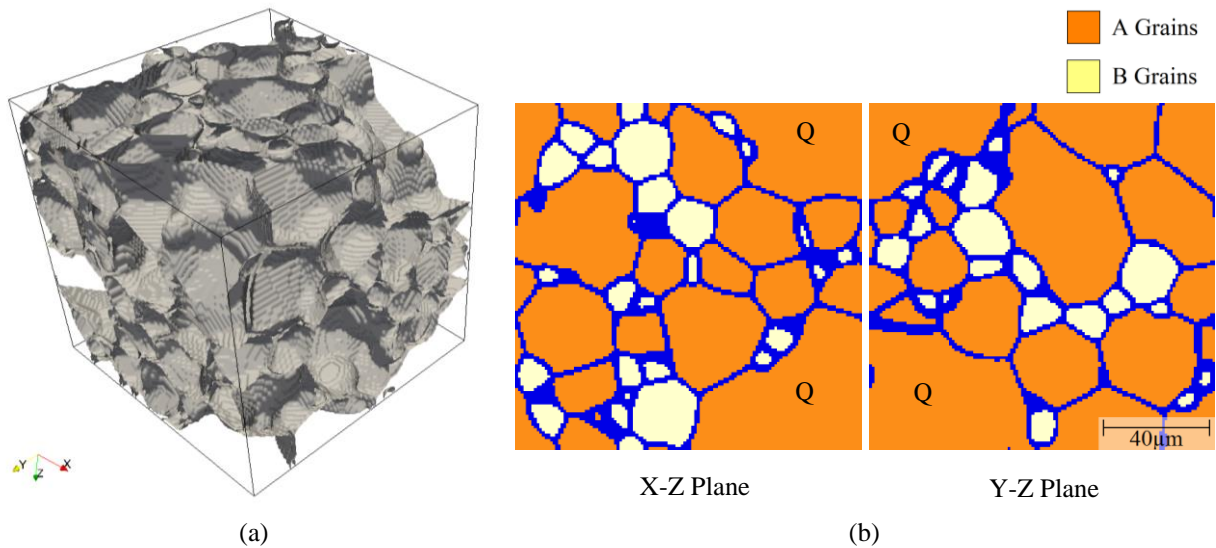


**Figure 5.11** The 3D cubic structure (a) and the cross section images (b) when initial A% = 50% and  $\mu_2/\mu_1 = 100$ .

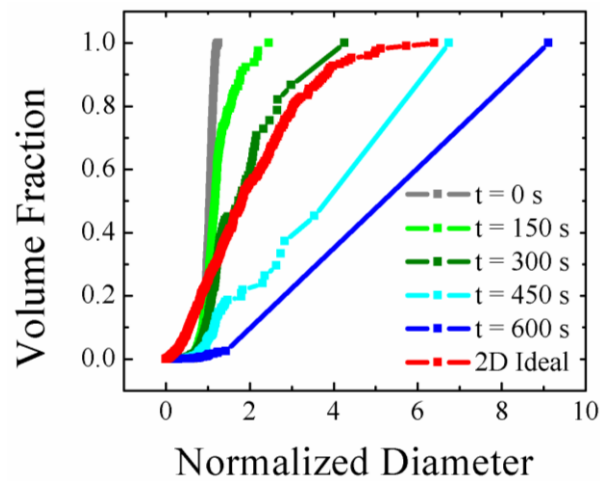


**Figure 5.12** Time evolution of cumulative grain volume distribution with fast A-A boundaries. ( $\mu_2/\mu_1 = 100$ , A % = 50 %).

Based on the 2D simulation results, in order to verify the abnormality under this condition a corresponding 3D simulation with 50% A grains in the initial microstructure were conducted. The 3D cubic microstructure after 300s, as well as the X-Z and Y-Z planes on the surface of the cube are presented in Fig. 5.11 (a) and (b), respectively. From those figures, one can observe that there is a large Q grain located in the corner of the cube surrounded by several small grains. Fig. 5.12 shows that after 300s the maximum EQAD is nearly 4 times larger than the mean EQAD and that it can even reach to 9 after 600s. This typical abnormal microstructure proves that the 3D simulation matches the 2D results very well.

### **5.2.2 Fast A-B boundaries**

Other than defining grain boundaries between same components (A-A boundaries) to be fast boundaries, another method to introduce mobility advantages is to assign boundaries between grains of the different components (A-B boundaries) to be fast mobile boundaries. As in the above, the two components A and B are represented with white and orange grains, respectively. The A-B boundaries are taken as highly mobile and their fraction is then determined by the fraction of B grains in the initial microstructure. An example for the evolution of the grain structure in the A-B system is shown in Fig. 5.13 for a mobility ratio of 1000 and 2% of B grains in the initial structure with a narrow size distribution resulting from Voronoi tessellation. Because of the small fraction of B grains, all of these B grains have initially only A grains as their neighbors as shown in Fig. 5.13(a) and are, thus, surrounded entirely by highly mobile grain boundaries. As a result, there is a rapid evolution of the B grains. Whether or not they grow or shrink depends on their size with respect to their neighbors, i.e. smaller B grains will shrink and larger B grains will grow. After a short time ( $t = 25$  s), about 1/3 of the B grains (e.g. grain III) have shrunk and disappeared very

quickly in the scenario shown in Fig. 5.13(b). Approximately 1/3 of B grains (e.g. grain I) grow rapidly at the expense of the surrounding A grains thereby forming a bimodal grain size distribution that is characteristic for AGG. The remaining 1/3 of B grains with a hexagonal structure (e.g. grain II) form, at least for some time, a stable grain structure with their neighbors that is a specific feature of 2D grain growth which does not exist in 3D. The extent of AGG, i.e. the maximum normalized diameter, depends then primarily on the spacing of the growing B grains which, in the present case, constitute 0.67% of all grains in the initial structure. Impingement of growing grains occurs at later times, see e.g. images at 50 s in Fig. 5.13(c) and 75 s in Fig. 5.13(d).

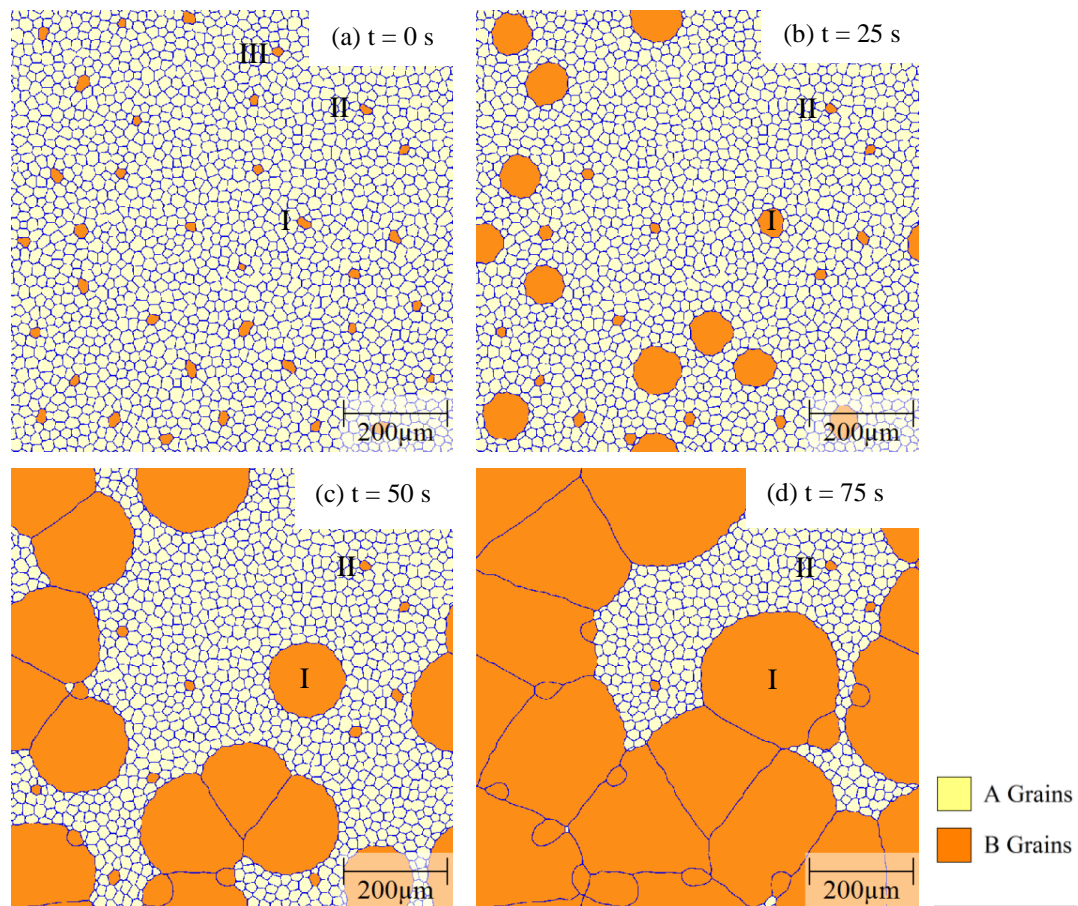


**Figure 5.13** Microstructure evolution of A-B system with fast A-B boundaries when  $\mu_2/\mu_1 = 1000$  and 0.67% growing B grains in the initial structure.

As discussed above for the threshold angle method, one can plot the evolution of the cumulative grain area distribution as a function of normalized diameter to further evaluate the abnormality of grain growth, as seen in Fig. 5.14. The red curve is the scaling distribution of normal grain growth as a reference. The initial grain size distribution resulting from Voronoi tessellation is very narrow before a bimodal distribution emerges quickly due to the rapid growth of a few of the B grains. The bimodality of the distribution is represented by the plateau in the cumulative grain area distribution, i.e. there are two populations of grains in the structure consisting of small grains (here the A grains and B grains that do not grow) and large grains (i.e. the growing B grains) with virtually no size overlap. With time the size of the growing B grains and their area fraction rapidly increases. For example, after 30s the maximum normalized diameter is 5 and the area fraction of the large grains is about 0.1. After 70s the largest normalized diameter of about 11 is reached and the area fraction of the large grains is increased to about 0.7. Eventually, the growing B grains impinge (see Fig. 5.13) and have consumed all A grains. As a result, the overall grain structure approaches that of a normal grain size distribution of the coarse B grains and the maximum normalized diameter starts to decrease at longer times. As a specific feature of the 2D grain growth simulations the initially stable hexagonal B grains are incorporated into the B grain microstructure as shown in Fig. 5.13. These smaller B grains remain almost frozen for some time as their shrinkage requires migration of the low mobility B-B grain boundaries. This retains technically a bimodal structure for some time with, however, an increasingly marginal area fraction of the small grains, e.g. after 90s the area fraction of the small grains is reduced to about 0.1 for the case shown in Fig. 5.14.

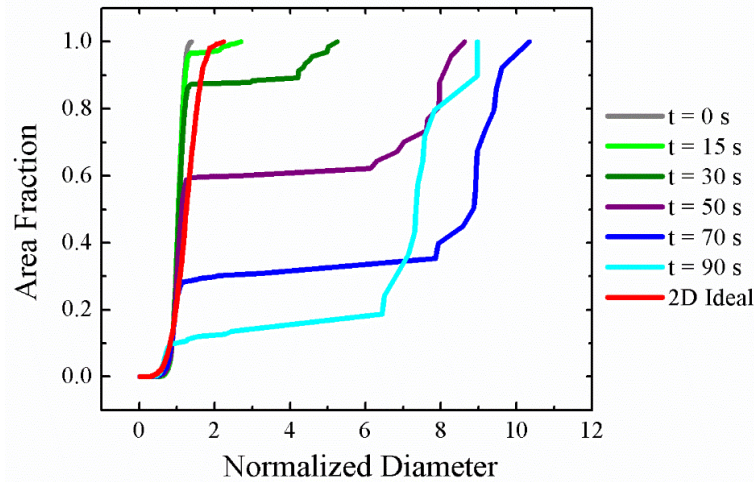


**Figure 5.14** Time evolution of cumulative grain area distribution in the A-B system ( $\mu_2/\mu_1 = 1000$ , growing B=0.67%).

Similar to the threshold angle approach, we performed a systematic parametric study to explore the influence of mobility ratio on AGG. The red line of normal grain growth is used as a benchmark. Taking the scenario with 0.44% of growing B grains in the initial structure the mobility ratio is varied from 5 to 1000, and the widest distribution curves are summarized in Fig. 5.15. For mobility ratios larger than 50, the distribution curves are very close to each other with a maximum normalized diameter of about 14, i.e. the degree of abnormality is not sensitive to mobility ratios larger than 50. For mobility ratios of 5 and 10 AGG is less severe with a maximum normalized diameter of 7 and 9, respectively, i.e. when the mobility ratio is less than 50, AGG is gradually reduced with decreasing mobility ratio.

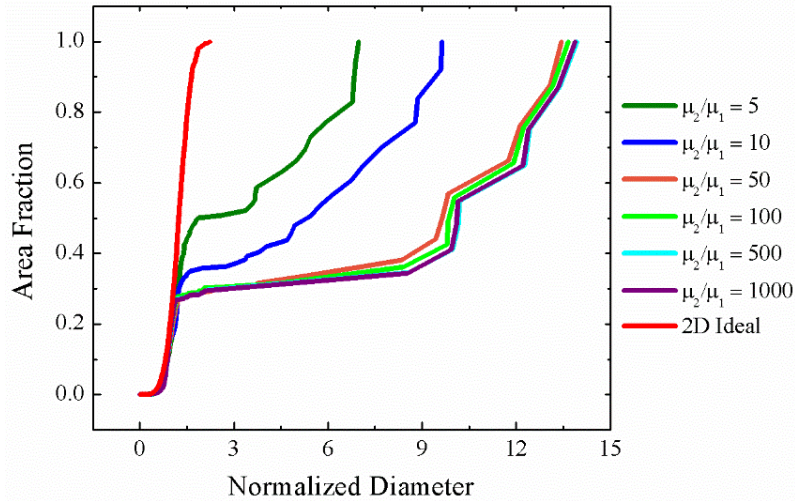


**Figure 5.15** Widest area distribution curves in the A-B system to study the effect of mobility ratio when growing B % = 0.44 %.

The influence of initial percentage of growing B grains on AGG is shown in Fig 5.16. Changing the percentage of growing B grains for a given mobility ratio (here 1000) affects the average distance between these B grains and thus influences the maximum normalized diameter that can be attained, as indicated by the microstructures shown in Figs. 5.16 (a) and (b). There are less growing B grains in Fig. 5.16(a), i.e. about 0.67%, than in Fig. 5.16(b), i.e. nearly 1.5%. As a result, much larger B grains can be found in the situation shown in Fig. 5.16(a) than in Fig. 5.16(b). Less growing B grains lead to a wider grain size distribution, as presented in Fig. 5.16(c), and thus a more abnormal grain structure. Therefore, a lower percentage of growing B grain facilitates more pronounced AGG as long as the mobility ratio is at least 50. For a growing B grain percentage of about 3.33% the maximum normalized diameter is reduced to 5 which may be taken as threshold for AGG.

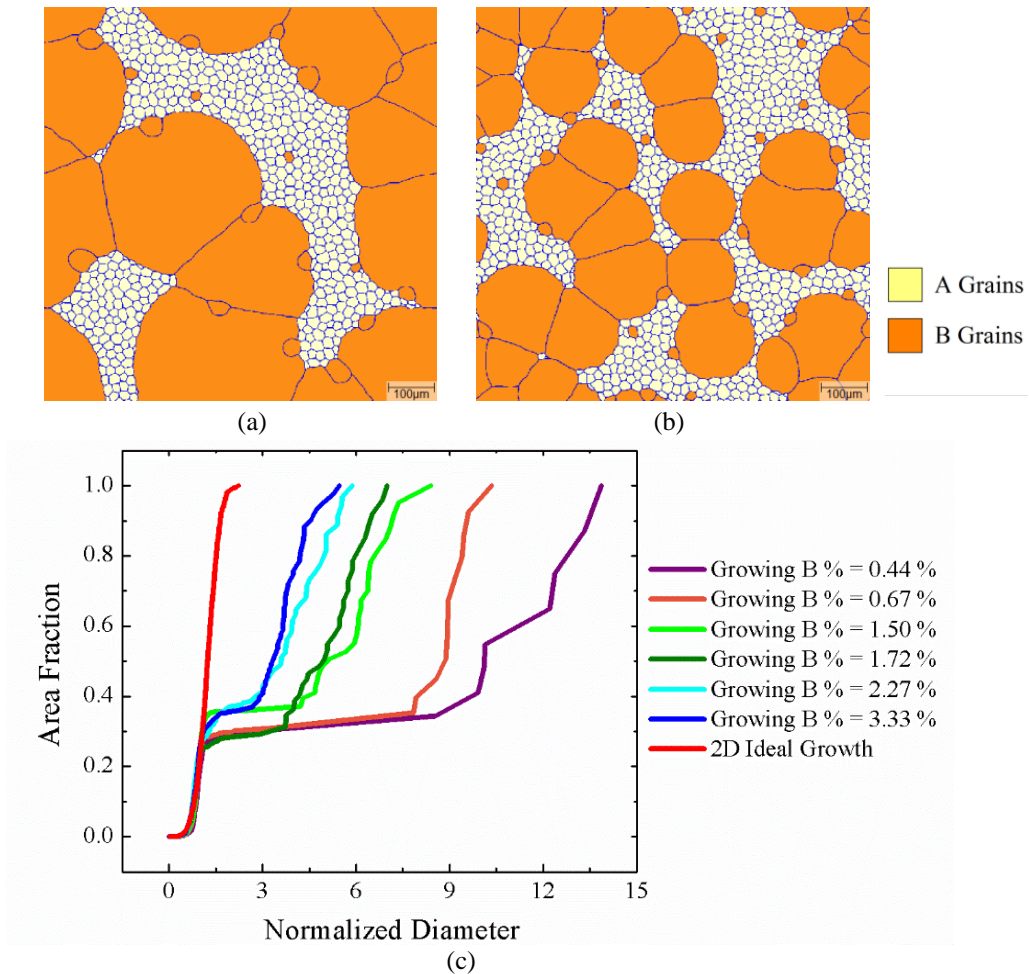


**Figure 5.16** Microstructure of the most abnormal position of (a) growing B % = 0.67 %; (b) growing B % = 1.5 % when  $\mu_2/\mu_1 = 1000$ . (c) Widest area distribution curves in A-B system to study the effect of growing B grain percentage when  $\mu_2/\mu_1 = 1000$ .

With a mobility ratio of 1000, the corresponding 3D simulation in A-B system are implemented. An example of the 3D simulation are shown in Fig. 5.17 where initially 2% B grains (1% growing B grains) are randomly positioned in the A grain matrix. When some B grains start to grow abnormally and before too many B grains impinged, the 3D cubic structure and its corresponding cross section planes are illustrated in Figs. 5.17(a) and (b), respectively. Both grain IV and grain V in Fig. 5.17(b) are obviously much larger than the surrounding matrix A grains, indicating that AGG occurs. Changing the percentage of growing B grains with the same mobility ratio of 1000,

the widest grain size distributions curves are presented in Fig. 5.18. Similar to 2D results, less growing B grains leads to a wider grain size distribution with a more dominant bimodal character. Therefore, AGG is promoted. The 3D microstructure simulations are similar to 2D results, other than that there are no “stable” grains that are neither growing nor shrinking in 3D simulations.

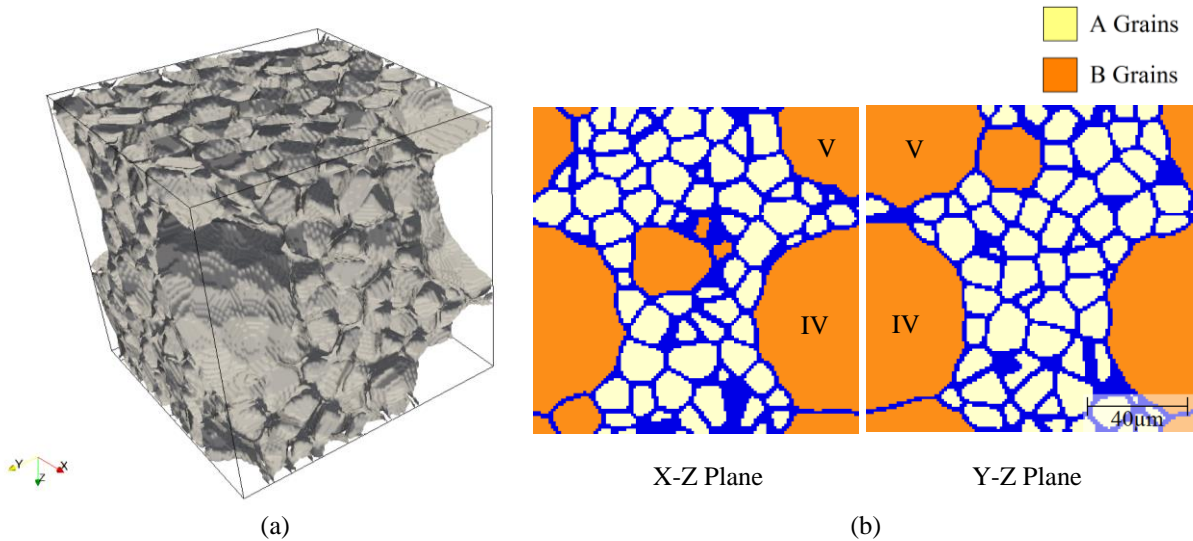


**Figure 5.17** The 3D grain structure (a) and the cross section (b) when growing B% = 1% and  $\mu_2/\mu_1 = 1000$ .

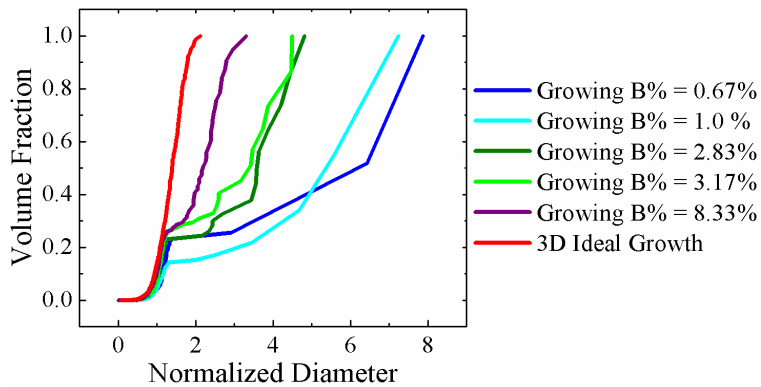


**Figure 5.18** Widest volume distribution curves of 3D A-B systems to investigate the influence of growing B grain percentage when  $\mu_2/\mu_1 = 1000$ .

In the two grain component systems, most (and for sufficiently small fractions all) growing B grains are surrounded by highly mobile A-B grain boundaries. As a result, these grains can grow rapidly in a regular, equiaxed fashion that leads to an unrealistic circular or spherical grain shape during AGG stages in 2D and 3D simulations, respectively. In contrast, often much more irregular abnormal grains are observed in experimental observations of AGG, including bulk grain growth and thin-film grain growth.

### **5.3 Mobility advantages in three grain type systems**

To add complexity into the simulations, a third grain type C is introduced as a result of which growing B grains will have a mixture of fast A-B boundaries and slow B-C boundaries. Fig. 5.19 shows a typical example of the grain structure obtained in the three grain type simulations with a mobility ratio of 1000. Here the red grains represent the B grains; orange and white grains are defined as A and C grains, respectively. Initially all grains have a similar size and 1% B grains are randomly distributed in the A-C grain matrix. Similar to the two grain type systems, some B grains with a smaller size will shrink and disappear quickly. The second group of B grains with a hexagonal structure will neither shrink nor grow and only those B grains with a size advantage over their neighbors will grow. A few of these growing B grains show clear signs of abnormal grains, i.e. complex grain morphologies including the formation of island grains.

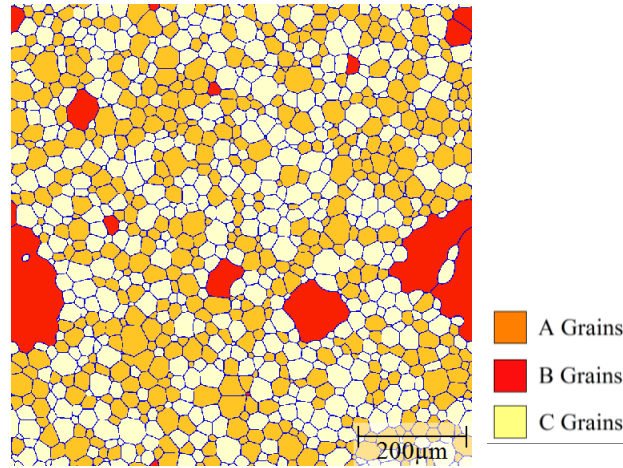


**Figure 5.19** Typical grain structure in a three grain type system with an initial composition of B% = 1%, A% = C% = 49.5% and a mobility ratio of 1000.

For computational efficiency, subsequent simulations were performed in a smaller domain to focus on the behavior of one candidate growing B grain and a mobility ratio of 1000. The percentage of A grains will influence the fraction of the highly mobile A-B boundaries that will change with time depending on the local environment of the growing B grain. Fig. 5.20 illustrates examples of the obtained grain morphologies of the B grain for different A grain percentages in the initial microstructure. When there are 30% A grains in the matrix, the B grain grows in a regular, equiaxed fashion with a polygonal shape that is more realistic than the circular shapes in the two grain type systems. Because some of the grain boundaries are fast A-B boundaries the B grain becomes the largest grain in the structure but its size advantage is rather modest such that the overall grain structure appearance is close to that for normal grain growth. Increasing the percentage of A grains leads to a higher fraction of fast A-B boundaries thereby promoting the growth of the B grain into an abnormally large grain. For an A grain percentage of 50%, the B grain evolves into an abnormally large grain with a more complex shape. Increasing the A grain percentage to 70%, the B grains becomes an even more prominent abnormal grain that also includes island grains that belong to grain type C. These island grains form when the growing B

grain locally reaches a situation where A grains completely surround a C grain. As the B grain can consume these A grains rapidly an island grain will result within the B grain. These island grains are unstable but will remain for some time as they can only be eliminated by migration of the low mobility B-C boundaries. The probability of the island formation hinges on a combination of a sufficiently high percentage of A grains with a still sizeable percentage of C grains. Increasing the A grain percentage to 90%, the B grain approaches a more equiaxed, circular shape but with some local inlet type features due to pinning by some small C grains. When increasing the A percentage further the evolution of the B grain becomes increasingly similar to the situation of the two grain type system discussed above in Section 5.2.2.

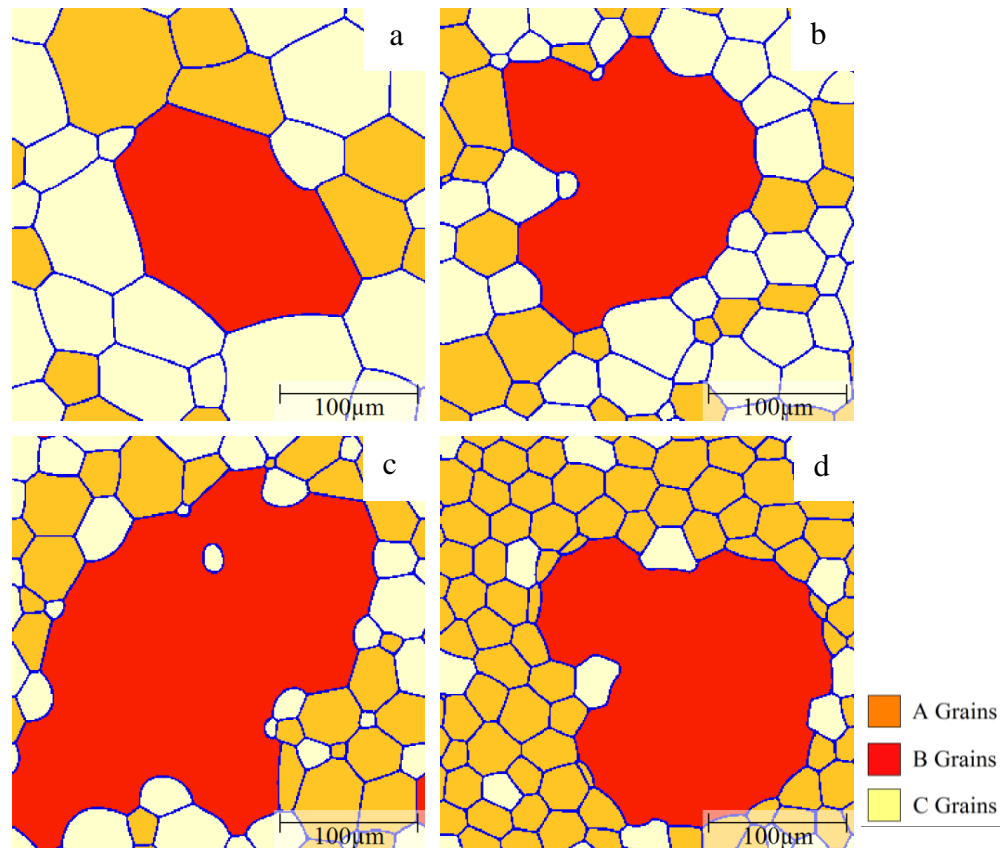


**Figure 5.20** Structure of rapidly growing B grain in three grain type systems with a mobility ratio of 1000 when (a) A=30%; (b) A=50%; (c) A=70%; (d) A=90%.

Since in the small box simulations, only one B grain is simulated each time, so one issue is that to what extent this B grain can represent the overall grain growth path. Fig. 5.21 compares the simulation results starting from different initial structures with otherwise the same simulation conditions, e.g. same initial fraction of A grains and same mobility ratio of 1000. Comparing Figs.5.21 (a) and (b) with 50% A grains in the initial structure, after 135 s, both abnormal B grains show an irregular structure with “arms”. Island grain 1 is formed in Fig. 5.21(c) with 70% A grains in the initial structure after 108 s. In Fig. 5.21(d), despite no island formed is yet after 108 s, grain 2 in Fig. 5.21(d) has shown a great potential to be an island grain. Although there are a few small differences, the overall growth feature of B grain is of the same tendency. Therefore, the grain growth paths in Fig 5.20 are representative.

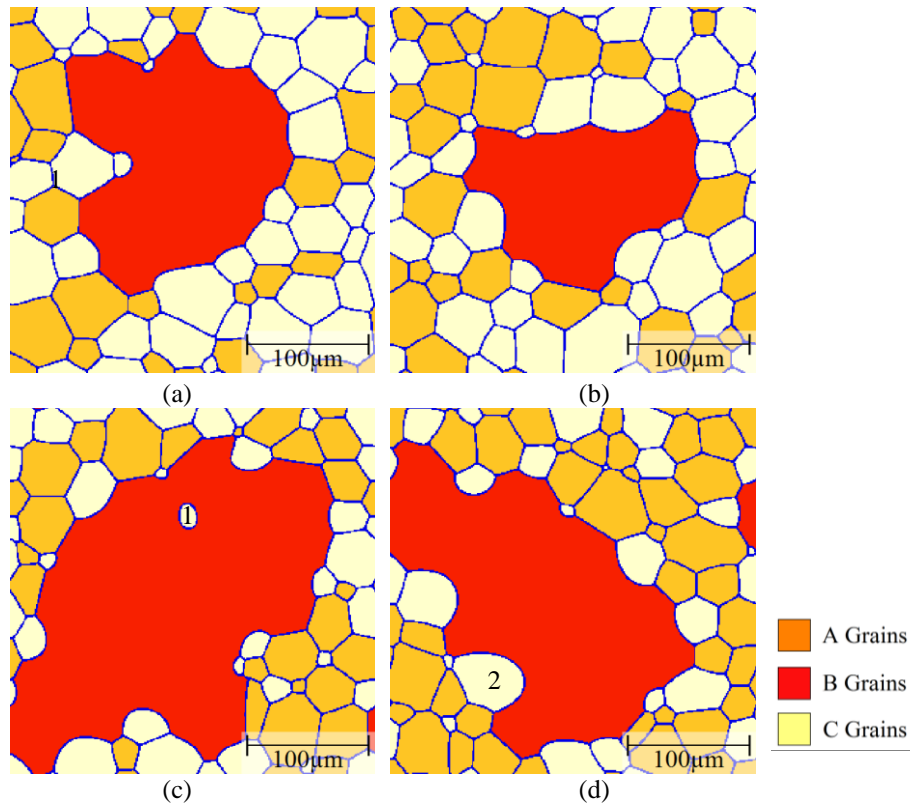


**Figure 5.21** The rapidly growing B grain starting from different initial structure with a mobility ratio of 1000 when (a,b) A=50%, t = 135 s; (c,d) A=70%, t = 108 s.

#### 5.4 Comparison with Monte Carlo simulation

Both PFM and MC simulations are effective and versatile methods to study AGG. However, whether the simulation methods will influence the simulation results is of great interest. Fig. 5.22 compares results of PFM and MC simulations. Both simulations start from the same initial structure with 68% A grains, as shown in Fig. 5.22(a) and (d) [56], and the mobility ratio is set to be 1000. In PFM, the B grain is in red while A and C grains are shown in white and orange, respectively. In the MC method [56], the white grain represents the B grain; red and blue grains are defined as A and C grains, respectively. Comparing Fig 5.22 (b) and (e), a small island grain is found in Fig. 5.22(e) [56] while at the same position, this small C grain has already been consumed in the PFM simulation. After running the simulation for a longer time, some island grains also start to form in PFM simulation, as shown in Fig. 5.22(c). However, in the MC model, there are much more island grains found as presented in Fig. 5.22(f). [56] The difference may be caused by the straightening effect of grain boundaries in PFM. In PFM, in order to reduce the total free energy, the grain boundaries tend to be straight lines thus losing the driving pressure due to curvature. Meanwhile, in the MC simulation, there is no such straighten effect. Nevertheless, apart from these minor differences, the overall coarsening mode of the abnormal grain in both simulations is very close to each other.

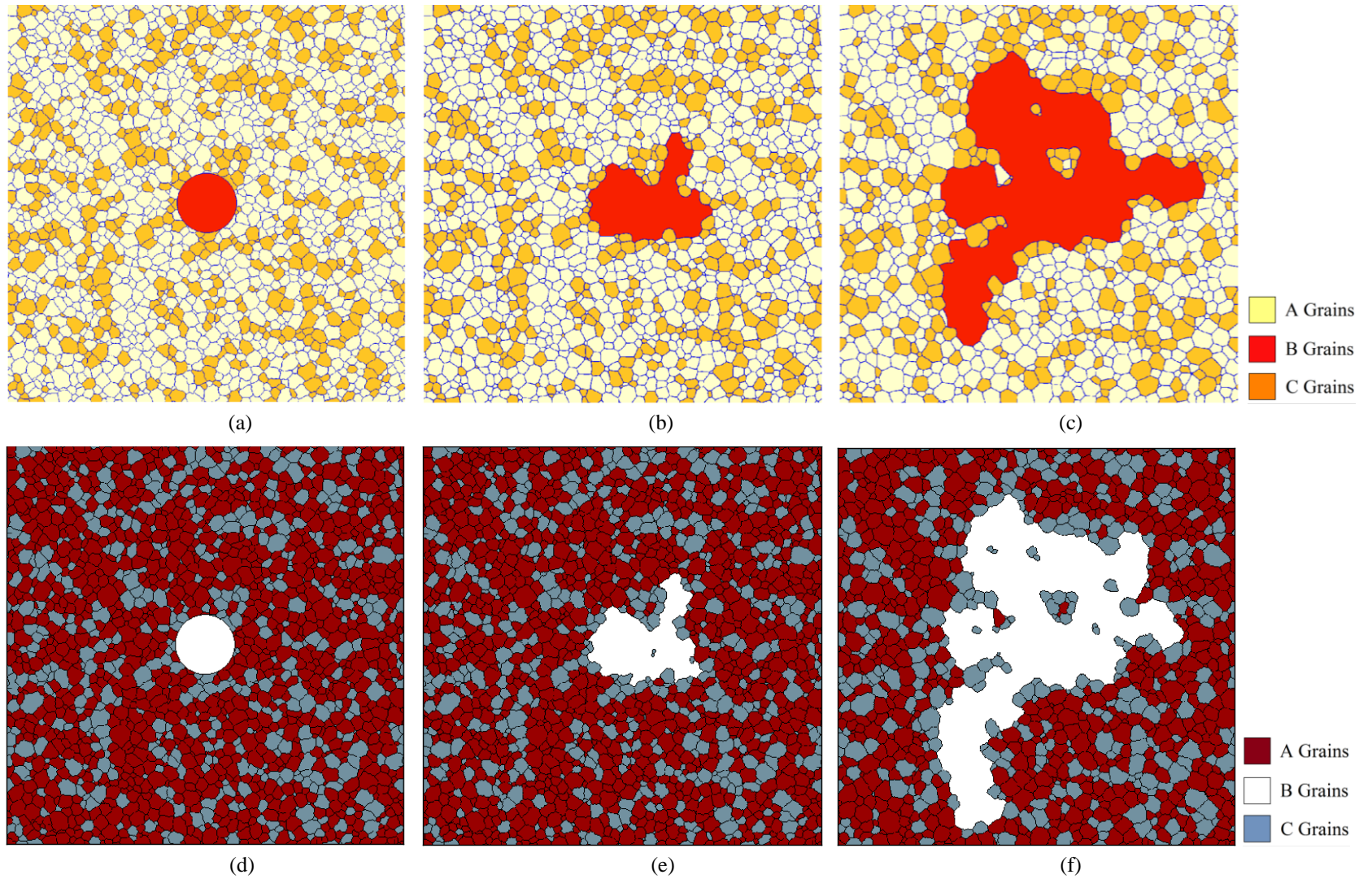


**Figure 5.22** Comparison between PFM and MC model. Both simulations start from the same initial microstructure.

Since the time scale in PFM and MC model are different, another interesting topic is how to match the two time scales and develop a more quantitative way to analyze the consistency of the two computational methods. In PFM, the simulation time is the real phase field time (PFT), and the unit is second. In the MC simulation, the time scale is measured by the Monte Carlo step. To match the two time scale, a constant parameter  $\kappa$  is introduced, where

$$t(MCS) = \kappa \cdot t(PFT) \quad (5.1)$$

Here  $\kappa = 5.1$  is obtained to best match the two simulation results in terms of the size evolution of the abnormal grain. The increase of the candidate grain area is plotted in Fig. 5.23 as a function of simulation time. From this graph, despite of little fluctuations, the overall grain growth paths are almost the same in both simulations.

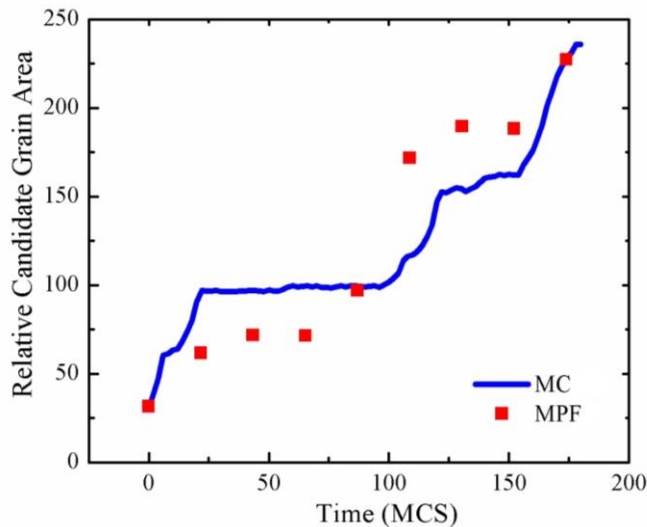


**Figure 5.23** Comparison of the size evolution of the abnormal grain obtained in PFM and MC simulations. Both simulations start from the same initial microstructure.

## Chapter 6: Conclusions and future work

For AGG to occur some of the grain boundaries must have a mobility advantage compared to other boundaries. 2D MPMF simulations have been conducted using three different ways to introduce highly mobile grain boundaries, i.e. a critical disorientation angle above which the boundaries are highly mobile as well as systems with two (A-B) texture components where the A-B or A-A boundaries being highly mobile and three (A-B-C) texture components where the A-B boundaries are assumed to be fast boundaries. Systematic parametric studies have been performed for these systems by changing the fraction of the highly mobile boundaries and the mobility ratio between high and low mobility boundaries to identify conditions for AGG. In the disorientation angle approach, modest AGG scenarios with maximum grain sizes of 5-6 times larger than the mean grain size are obtained for a narrow range of threshold angles near  $40^\circ$  and mobility ratios of at least 100. In two (A-B) texture components approach with A-B boundaries fast, AGG with a well-developed bimodal grain structure can readily occur for mobility ratios as low as 10 in the two grain types system when the fraction of growing B grains is sufficiently small. The maximum grain size depends primarily on the distance between the growing grains. In the present simulations, a maximum grain size of 14 times larger than the apparent mean grain size has been obtained when 0.4% of the initial grains can grow abnormally. Meanwhile in two (A-B) texture components approach with A-A boundaries fast, modest AGG scenarios with maximum EQAD slightly larger than 5 are obtained for approximately 50% of A grains in the initial microstructure and mobility ratios of at least 100. The situation with A-A boundaries fast in two texture component system is in many ways similar to the threshold angle scenario.

The 2D simulation results provide guidance for future 3D simulations to specify in more detail AGG conditions for bulk materials. The corresponding 3D simulations have been conducted for both threshold angle approach with a threshold of  $45^\circ$  as well as two (A-B) texture component approach with 2% B grains in the initial system when A-B boundaries are defined as fast mobile boundaries and 50% A grains in the initial microstructure when A-A boundaries are assumed to be highly mobile. In 3D simulation with a mobility ratio of 1000 and a threshold angle of  $45^\circ$ , the maximum grain sizes is only 4 times larger than the mean grain size. In two texture component approach, with A-B boundaries fast and small fraction of 2% B grains in the initial structure, AGG occurs with an obvious bimodal grain structure, coincident with previous 2D results. The 3D simulation results shows some abnormality when A-A boundaries are highly mobile with 50% A grains in the initial system.

The two grain type simulations with A-B boundary fast lead, however, to rather unrealistic circular shapes of the abnormal grains. This aspect can be mitigated when introducing a third grain type in the system where the growing grains are not completely surrounded by highly mobile boundaries. The 2D simulation results show realistic shapes of abnormally growing grains including the formation of island grains for a range of conditions with a sufficiently high fraction of highly mobile boundaries while maintaining a critical amount of the third grain type. Further, a comparison with Monte Carlo simulation done by DeCost et al. [56] has shown that the simulation results from multi-phase field model and Monte Carlo model are quantitatively very similar for AGG. However, a systematic parameter study (fraction of A grains, mobility ratio) has yet to be conducted for the three texture components systems.

So far in this research, 3D simulations were conducted only for some selected situations in threshold angle approach and two texture components approach, and no 3D simulations were conducted in three texture component approach since it is very time consuming. The 3D results have not yet been presented in a systematic way, and thus more 3D simulations would be required for a more quantitative analysis. Further, the above studies apply to pure systems, and can be further extended to include the role of precipitate pinning as well as solute drag which will add complexity to the analysis.

## Bibliography

- [1] A. Morawiec, "On abnormal growth of Goss grains in grain-oriented silicon steel," *Scripta Materialia*, vol. 64, no. 5, pp. 466-469, 2011.
- [2] W. Mao, Y. Li, P. Yang and W. Guo, "Abnormal growth mechanisms of Goss grains in grain-oriented electrical steels," *Materials Science Forum*, vols. 702-703, pp. 585-590, 2012.
- [3] W. Mao, W. Guo and Y. Li, "Growth process of Goss grains during secondary recrystallization of grain-oriented electrical steels," *steel research international*, vol. 81, no. 12, pp. 1117-1120, 2010.
- [4] W. Guo and W. Mao, "Abnormal growth of Goss grains in grain-oriented electrical steels," *Journal of Materials Science and Technology*, vol. 26, no. 8, pp. 759-762, 2010.
- [5] N. Maazi, N. Rouag, A. L. Etter, R. Penelle and T. Baudin, "Influence of neighborhood on abnormal Goss grain growth in Fe-3% Si steels: Formation of island grains in the large growing grain," *Scripta Materialia*, vol. 55, no. 7, pp. 641-644, 2006.
- [6] N. Rajmohan, J. A. Szpunar and Y. Hayakawa, "Importance of fractions of highly mobile boundaries in abnormal growth of Goss grains," *Materials Science and Engineering A*, vol. 259, no. 1, pp. 8-16, 1999.
- [7] A. L. Etter, T. Baudin, R. Penelle, "Influence of the Goss grain environment during secondary recrystallization of conventional grain oriented Fe-3% Si steels," *Scripta Materialia*, vol. 47, no. 11, pp. 725-730, 2002.
- [8] J. Harase, R. Shimizu, and D. J. Dingley, "Texture evolution in the presence of precipitates in Fe-3% Si alloy," *Acta Metallurgica et Materialia*, vol. 39, no. 5, pp. 763-770, 1991.
- [9] A. Morawiec, "Grain misorientations in theories of abnormal grain growth in silicon steel," *Scripta Materialia*, vol. 43, no. 3, pp. 275-278, 2000.
- [10] M. Matsuo, "Texture control in the production of grain oriented silicon steels," *ISIJ International*, vol. 29, no. 10, pp. 809-827, 1989.
- [11] H. Park, D. Y. Kim, N. M. Hwang, Y. C. Joo, C. H. Han and J. K. Kim, "Microstructure evidence of abnormal grain growth by solid-state wetting in Fe-3% Si steel," *Journal of Applied Physics*, vol. 95, no. 10, pp. 5515-5521, 2004.

- [12] A. K. Giunelli, M. Militzer and E. B. Hawbolt, "Analysis of the austenite grain size distribution in plain carbon steels," *ISIJ International*, vol. 39, no. 3, pp. 271-280, 1999.
- [13] J. S. Choi and D. Y. Yoon, "The temperature dependence of abnormal grain growth and grain boundary faceting in 316L stainless steel," *ISIJ International*, vol. 41, no. 5, pp. 478-483, 2001.
- [14] S. B. Lee, N. M. Hwang, D. Y. Yoon, and M. F. Henry, "Grain boundary faceting and abnormal grain growth in Nickel," *Metallurgical and Materials Transactions A*, vol. 31, no. 3, pp. 985-994, 2000.
- [15] S. B. Lee, D. Y. Yoon and M. F. Henry, "Abnormal grain growth and grain boundary faceting in a model Ni-based superalloy," *Acta Materialia*, vol. 48, no. 12, pp. 3071-3080, 2000.
- [16] J. Dennis, P. S. Bate, F. J. Humphreys, "Abnormal grain growth in Al-3.5Cu," *Acta Materialia*, vol. 57, no. 15, pp. 4539-4547, 2009.
- [17] S. Jana, R. S. Mishra, J. A. Baumann, G. Grant, "Effect of process parameters on abnormal grain growth during friction stir processing of a cast Al alloy," *Materials Science and Engineering A*, vol. 528, no. 1, pp. 189-199, 2010.
- [18] T. Garcin, J. H. Schmitt, M. Militzer, "In-situ laser ultrasonic grain size measurement in superalloy Inconel 718," *Journal of Alloys and Compounds*, vol. 670, pp. 329-336, 2016.
- [19] S. J. Dillon and M. P. Harmer, "Diffusion controlled abnormal grain growth in ceramics," *Materials Science Forum*, vols. 558-559, pp. 1227-1236, 2007.
- [20] S. I. Bae and S. Baik, "Determination of critical concentration of silica and/or calcia for abnormal grain growth in alumina," *Journal of the American Ceramic Society*, vol. 76, no. 4, pp. 1065-1067, 1993.
- [21] I. J. Bae and S. Baik, "Abnormal grain growth of alumina," *Journal of the American Ceramic Society*, vol. 80, no. 5, pp. 1149-1156, 1997.
- [22] W. Dressler, H. J. Kleebe, M. J. Hoffmann, M. Ruhle and G. Petzow, "Model experiments concerning abnormal grain growth in silicon nitride," *Journal of the European Ceramics Society*, vol. 16, no.1, pp. 3-14, 1996.
- [23] H. Emoto and M. Mitomo, "Control and characterization of abnormal grown grains in silicon nitride ceramics," *Journal of the European Ceramics Society*, vol. 17, no. 6, pp. 797-804, 1997.

- [24] B. Lee, S. Chung and S. L. Kang “Grain boundary faceting and abnormal grain growth in BaTiO<sub>3</sub>,” *Acta Materialia*, vol. 48, no. 7, pp. 1575-1580, 2000.
- [25] A. D. Rollett, W. W. Mullins, “On the growth of abnormal grains,” *Scripta Materialia*, vol. 36, No. 9, pp. 975-980, 1997.
- [26] G. S. Grest, M. P. Anderson, D. J. Srolovitz, A. D. Rollett, “Abnormal grain growth in three dimensions,” *Acta Metallurgica et Materialia*, vol. 24, no. 4, pp. 661-665, 1990.
- [27] P. R. Rios, “Abnormal Grain growth development from uniform grain size distributions,” *Acta Materialia*, vol. 45, no. 4, pp. 1785-1789, 1997.
- [28] S. G. Kim, Y. B. Park, “Grain boundary segregation, solute drag and abnormal grain growth,” *Acta Materialia*, vol. 56, no. 15, pp. 3739-3753, 2008.
- [29] M. Hillert, “On the theory of normal and abnormal grain growth,” *Acta Metallurgica*, vol. 13, no. 3, pp. 227-238, 1965.
- [30] G. C. Abbruzzese and C. Forzanti, “Homogeneous abnormal grain growth in polycrystalline materials,” *Materials Science Forum*, vols. 706-709, pp. 1355-1360, 2012.
- [31] V. Y. Novikov, “Secondary recrystallization evolution and pinning force behaviour,” *Scripta Materialia*, vol. 37, no. 4, pp. 463-469, 1997.
- [32] I. Andersen, Ø. Grong and N. Ryum, “Analytical modelling of grain growth in metals and alloys in the presence of growing and dissolving precipitates – II. Abnormal grain growth,” *Acta Metallurgica et Materialia*, vol. 43, no. 7, pp. 2689-2700, 1995.
- [33] M. A. Razzak, M. Perez, T. Sourmail, S. Cazottes, M. Frotey, “A simple model for abnormal grain growth,” *ISIJ International*, vol. 52, no. 12, pp. 2278-2282, 2012.
- [34] N. Moelans, B. Blanpain and P. Wollants, “An introduction to phase-field modeling of microstructure evolution,” *Computer Coupling of Phase Diagrams and Thermochemistry*, vol. 32, no. 2, pp. 268-294, 2008.
- [35] P. R. Cha, D. H. Yeoh, J. K. Yoon, “Phase-field model for multicomponent alloy solidification,” *Journal of Crystal Growth*, vol. 274, no. 1-2, pp. 281-293, 2005.
- [36] N. Ofori-Opoku, N. Provatas, “A quantitative multi-phase field model of polycrystalline alloy solidification,” *Acta Materialia*, vol. 58, no. 6, pp. 2155-2164, 2010.

- [37] B. Zhu, M. Militzer, "3D phase field modelling of recrystallization in a low-carbon steel," *Modelling and Simulation in Materials Science and Engineering*, vol. 20, no. 8, 085011, 2012.
- [38] T. Takaki, T. Hirouchi, Y. Hisakuni, A. Yamanaka, Y. Tomita, "Multi-phase-field model to simulate microstructure evolutions during dynamic recrystallization," *Materials Transactions*, vol. 49, no. 11, pp. 2559-2565, 2008.
- [39] B. Zhu, H. Chen, M. Militzer, "Phase-field modeling of cyclic phase transformations in low-carbon steels," *Computational Materials Science*, vol. 108, pp. 333-341, 2015.
- [40] M. Militzer, M. G. Meozzi, J. Sietsma, S. van der Zwaag, "Three-dimensional phase field modelling of the austenite-to-ferrite transformation," *Acta Materialia*, vol. 54, no. 15, pp. 3961-3972, 2006.
- [41] N. Moelans, F. Wendler, B. Nestler, "Comparative study of two phase-field models for grain growth," *Computational Materials Science*, vol. 46, no. 2, pp. 479-490, 2009.
- [42] N. Moelans, B. Blanpain and P. Wollants, "Phase field simulations of grain growth in two-dimensional system containing finely dispersed second-phase particles," *Acta Materialia*, vol. 54, no. 4, pp. 1175-1184, 2006.
- [43] A. Mallick, "Effect of second phase mobile particles on polycrystalline grain growth," *Computer Materials Science*, vol. 67, pp. 27-34, 2013.
- [44] S. Vedantam, A. Mallick, "Phase-field theory of grain growth in the presence of mobile second-phase particles," *Acta Materialia*, vol. 58, no. 1, pp. 272-281, 2010.
- [45] M. Greenwood, C. Sinclair, M. Militzer, "Phase field crystal model of solute drag," *Acta Materialia*, vol. 60, no. 16, pp. 5752-5761, 2012.
- [46] S. Shahandeh, M. Greenwood, M. Militzer, "Friction pressure method for simulating solute drag and particle pinning in a multiphase-field model," *Modelling and Simulation in Materials Science and Engineering*, vol. 20, no. 6, 065008, 2012.
- [47] Y. Suwa, Y. Saito, H. Onodera, "Phase-field simulation of abnormal grain growth due to inverse pinning," *Acta Materialia*, vol. 55, no. 20, pp. 6881-6894, 2007.
- [48] P. Blikstein, A. P. Tschiptschin, "Monte Carlo simulation of grain growth," *Materials Research*, vol. 2, no. 3, pp. 133-137, 1999.

- [49] N. Maazi and R. Penelle, "Introduction of preferential Zener drag effect in Monte Carlo simulation of abnormal Goss grain growth in the Fe-3%Si magnetic alloys," *Materials Science and Engineering: A*, vol. 504, no. 1-2, pp. 135-140, 2009.
- [50] C. S. Park, T. W. Na, H. K. Park, B. J. Lee, C. H. Han and N. M. Hwang, "Three-dimensional Monte Carlo simulation for the effect of precipitates and sub-boundaries on abnormal grain growth," *Scripta Materialia*, vol. 66, no. 6, pp. 398-401, 2012.
- [51] K. J. Ko, A. D. Rollett, N. M. Hwang, "Abnormal grain growth of Goss grains in Fe-3% Si steel driven by sub-boundary-enhanced solid-state wetting: Analysis by Monte Carlo simulation," *Acta Materialia*, vol. 58, no. 13, pp. 4414-4423, 2010.
- [52] A. D. Rollett, D. J. Srolovitz and M. P. Anderson, "Simulation and theory of abnormal grain growth – anisotropic grain boundary energies and mobilities," *Acta Metallurgica*, vol. 37, no. 4, pp. 1227-1240, 1989.
- [53] H. N. Lee, H. S. Ryoo, S. K. Hwang, "Monte Carlo simulation of microstructure evolution based on grain boundary character distribution," *Materials Science and Engineering A*, vol. 281, no. 1, pp. 176-188, 2000.
- [54] N. M. Hwang, "Simulation of the effect of anisotropic grain boundary mobility and energy on abnormal grain growth," *Journal of Materials Science*, vol. 33, no. 23, pp. 5625-5629, 1998.
- [55] B. L. DeCost, E. A. Holm, "Phenomenology of abnormal grain growth in system with non-uniform grain boundary mobility," *Metallurgical and Materials transactions A*, vol. 48, no. 6, pp. 2771-2780, 2017.
- [56] D. J. Srolovitz, G. S. Grest and M. P. Anderson, "Computer simulation of grain growth – V. Abnormal grain growth," *Acta Metallurgica*, vol. 33, no. 12, pp. 2233-2247, 1985.
- [57] R. Messina, M. Soucail, L. Kubin, "Monte Carlo simulation of abnormal grain growth in two dimensions," *Materials Science and Engineering A*, vol. 308, no. 1-2, pp. 258-267, 2001.
- [58] G. S. Grest, D. J. Srolovitz and M. P. Anderson, "Computer simulation of grain growth – IV. Anisotropic grain boundary energies," *Acta Metallurgica*, vol. 33, no. 3, pp. 509-520, 1985.
- [59] U. Kunaver and D. Kolar, "Three-dimensional computer simulation of anisotropic grain growth in ceramics," *Acta Materialia*, vol. 46, no. 13, pp. 4629-4640, 1998.
- [60] S. Shahandeh, "Phase field modelling of grain growth with particle pinning and solute drag," PhD thesis, The University of British Columbia, 2013.

- [61] J. Eiken, B. Böttger, I. Steinbach, "Multiphase-field approach for multicomponent alloys with extrapolation scheme for numerical application," *Physical Review E*, vol. 73, 066122, 2006.
- [62] J. Burke and D. Turnbull, "Recrystallization and grain growth," *Progress in Metal Physics*, vol. 3, pp. 220-292, 1952.

# Appendices

## Appendix A

### A.1 Input script of threshold angle approach

```
#
# Automatic 'Driving File' written out by MICRESS.
#
#
# MICRESS binary
# =====
# version number: 6.200 (Linux)
# compiled: 11/27/2014
# compiler version: Intel 1400 20140120
# executable architecture: x64
# Thermo-Calc coupling: disabled
# OpenMP: enabled
# shell: /bin/tcsh
# ('double precision' binary)
# permanent license
#
#
# Language settings
# =====
# Please select a language: 'English', 'Deutsch' or 'Francais'
English
#
#
# Flags and settings
# =====
#
# Geometry
# -----
# Grid size?
# (for 2D calculations: CellsY=1, for 1D calculations: CellsX=1, CellsY=1)
# Cells in X-direction (CellsX):
800
# Cells in Y-direction (CellsY):
1
# Cells in Z-direction (CellsZ):
800
# Cell dimension (grid spacing in micrometers):
# (optionally followed by rescaling factor for the output in the form of '3/4')
1.0
#
# Flags
# -----
# Type of coupling?
# Options: phase concentration temperature temp_cyl_coord
# [stress] [stress_coupled] [flow] [flow_coarse] [dislocation]
phase
# Type of potential?
# Options: double_obstacle multi_obstacle [fd_correction]
multi_obstacle fd_correction
#
# Phase field data structure
# -----
# Coefficient for initial dimension of field iFace
# [minimum usage] [target usage]
0.1
# Coefficient for initial dimension of field nTupel
# [minimum usage] [target usage]
```

```

0.1
#
# Restart options
# =====
# Restart using old results?
# Options:      new          restart [reset_time | structure_only]
new
#
# Name of output files
# =====
# Name of result files?
2D_disorientation40
# Overwrite files with the same name?
# Options:      overwrite    write_protected    append
#               [zipped|not_zipped|vtk]
#               [unix|windows|non_native]
overwrite
#
# Selection of the outputs
# =====
# [legacy|verbose|terse]
# Restart data output?
# Options:      out_restart    no_out_restart    ('rest')
#               [wallclock time, h.]
out_restart
# Grain number output?
# Options:      out_grains     no_out_grains     ('korn')
out_grains
# Phase number output?
# Options:      out_phases     no_out_phases     ('phas')
#               [no_interfaces]
out_phases
# Fraction output?
# Options:      out_fraction   no_out_fraction   ('frac')
#               [phase number]
no_out_fraction
# Average fraction table?
# Options:      tab_fractions  no_tab_fractions  ('TabF')
#               [front_temp] [TabL_steps]
tab_fractions
# Interface output?
# Options:      out_interface  no_out_interface  ('intf')
#               [sharp]
out_interface
# Driving-force output?
# Options:      out_driv_force no_out_driv_force ('driv')
out_driv_force
# Interface mobility output?
# Options:      out_mobility   no_out_mobility   ('mues')
out_mobility
# Curvature output?
# Options:      out_curvature  no_out_curvature  ('krum')
no_out_curvature
# Interface velocity output?
# Options:      out_velocity   no_out_velocity   ('vel')
no_out_velocity
# Should the grain-time file be written out?
# Options:      tab_grains     no_tab_grains     ('TabK')
#               [extra|standard]
tab_grains
# Should the 'von Neumann Mullins' output be written out?
# Options:      tab_vnm        no_tab_vnm         ('TabN')
no_tab_vnm
# Should the 'grain data output' be written out?
# Options:      tab_grain_data no_tab_grain_data  ('TabGD')
tab_grain_data
# Temperature output?
# Options:      out_temp       no_out_temp        ('temp')
no_out_temp
# Recrystallisation energy output?
# Options:      out_recry stall no_out_recry stall ('rex')
no_out_recry stall
# Recrystallised fraction output?
# Options:      tab_recry stall no_tab_recry stall ('TabR')
no_tab_recry stall

```

```

# Dislocation density output?                                ('rhoD')
# Options:    out_disloc          no_out_disloc
no_out_disloc
# Miller-Indices output?                                    ('mill')
# Options:    out_miller          no_out_miller
no_out_miller
# Orientation output?                                      ('orie')
# Options:    out_orientation     no_out_orientation
out_orientation
# Should the orientation-time file be written?             ('TabO')
# Options:    tab_orientation     no_tab_orientation     [rotmat]
tab_orientation
# Should monitoring outputs be written out?               ('TabL')
# Options:    tab_log [simulation time, s] [wallclock time, min] no_tab_log
tab_log 0.25
#
#
# Time input data
# =====
# Finish input of output times (in seconds) with 'end_of_simulation'
# 'regularly-spaced' outputs can be set with 'linear_step'
# or 'logarithmic_step' and then specifying the increment
# and end value
# ('automatic_outputs' optionally followed by the number
# of outputs can be used in conjunction with 'linear_from_file')
# 'first'          : additional output for first time-step
# 'end_at_temperature' : additional output and end of simulation
#                   at given temperature
linear_step 5.0 400.0
end_of_simulation
# Time-step?
# Options:    fix ...[s]    automatic    automatic_limited
automatic
# Coefficient for phase-field criterion 1.00
# Number of steps to adjust profiles of initially sharp interfaces [exclude_inactive]?
8
#
#
# Phase data
# =====
# Number of distinct solid phases?
1
#
# Data for phase 1:
# -----
# Simulation of recrystallisation in phase 1?
# Options:    recrystall      no_recrystall    [verbose|no_verbose]
no_recrystall
# Is phase 1 anisotropic?
# Options:    isotropic      anisotropic      faceted      antifaceted
anisotropic
# Crystal symmetry of the phase?
# Options:    none          cubic          hexagonal    tetragonal    orthorhombic
cubic
# Should grains of phase 1 be reduced to categories?
# Options:    categorize     no_categorize
no_categorize
#
# Orientation
# -----
# How shall grain orientations be defined?
# Options:    angle_2d      euler_zxz    angle_axis    miller_indices    quaternion
euler_zxz
#
#
# Grain input
# =====
# Type of grain positioning?
# Options:    deterministic  random [deterministic_infile]    from_file

```

```

random
# Integer for randomization?
110
# Number of different types of grains?
1
# Number of grains of type 1?
1800
# Input for grain type 1
# -----
# Geometry of grain type 1
# Options: round    rectangular    elliptic
round
# Minimal value of x-coordinates? [micrometers]
0.00000
# Maximal value of x-coordinates? [micrometers]
800.000
# Minimal value of z-coordinates? [micrometers]
0.00000
# Maximal value of z-coordinates? [micrometers]
800.000
# Minimum grain radius? [micrometers]
20.0000
# Maximum grain radius? [micrometers]
20.0000
# Shall grain type 1 be stabilized or shall
# an analytical curvature description be applied?
# Options: stabilisation    analytical_curvature
stabilisation
# Should the Voronoi criterion for grains of type 1 be applied?
# Options: voronoi    no_voronoi
voronoi
# Phase number for grain type 1? (int)
1
# Determination of grain orientations?
# Options: random    fix    fix_direction
random
# Minimal distance between grains (real) [micrometers]?
15.000
#
#
# Data for further nucleation
# =====
# Enable further nucleation?
# Options: nucleation    nucleation_symm    no_nucleation    [verbose|no_verbose]
no_nucleation
#
#
# Phase interaction data
# =====
#
# Data for phase interaction 0 / 1:
# -----
# Simulation of interaction between phase 0 and 1?
# Options: phase_interaction    no_phase_interaction
# [standard|particle_pinning[_temperature]|solute_drag]
# |[no_junction_force|junction_force]
no_phase_interaction
#
# Data for phase interaction 1 / 1:
# -----
# Simulation of interaction between phase 1 and 1?
# Options: phase_interaction    no_phase_interaction    identical    phases    nb
# [standard|particle_pinning[_temperature]|solute_drag]
# |[no_junction_force|junction_force]
phase_interaction
# Type of surface energy definition between phases 1 and 1?
# Options: constant    temp_dependent
constant
# Surface energy between phases 1 and 1? [J/cm**2]

```

```

# [max. value for num. interface stabilisation [J/cm**2]]
1.0E-5
# Type of mobility definition between phases 1 and 1?
# Options: constant temp_dependent dg_dependent thin_interface_correction
[fixed_minimum]
constant thin_interface_correction
# Kinetic coefficient mu between phases 1 and 1 [ min. value ] [cm**4/(Js)] ?
5.0E-2
# Shall misorientation be considered?
# Options: misorientation no_misorientation [transition LAB/HAB in degree]
misorientation 40
# Input of the misorientation coefficients:
# Modification of surface energy for low angle boundaries
# Options: factor Read-Shockley
factor
# prefactor of surface energy:
1.0000
# Modification of the mobility for low angle boundaries
# Options: factor Humphreys [min_reduction + parameters B and N (default: min_red=0.
B=5.0 N=4.0)]
factor
# prefactor of the mobility for low angle boundaries
1.00000E-03
#
#
# Phase diagram - input data
# =====
#
#
# Boundary conditions
# =====
# Type of temperature trend?
# Options: linear linear_from_file profiles_from_file
linear
# Number of connecting points? (integer)
0
# Initial temperature at the bottom? (real) [K]
1000.000
# Temperature gradient in z-direction? [K/cm]
0.0000
# Cooling rate? [K/s]
0.0000
# Moving-frame system in z-direction?
# Options: moving_frame no_moving_frame
no_moving_frame
#
# Boundary conditions for phase field in each direction
# Options: i (insulation) s (symmetric) p (periodic/wrap-around)
# g (gradient) f (fixed) w (wetting)
# Sequence: w E (S N, if 3D) B T borders
pppp
# Unit-cell model symmetric with respect to the x/y diagonal plane?
# Options: unit_cell_symm no_unit_cell_symm
no_unit_cell_symm
#
#
# Other numerical parameters
# =====
# Phase minimum?
1.0E-4
# Interface thickness (in cells)?
4.00
#
#
#
# Number of parallel threads?
# =====
1
# Number of parallel threads: 1

```

## A.2 Input script of two texture components approach with A-A boundary fast

```
#
# Automatic 'Driving File' written out by MICRESS.
#
#
# MICRESS binary
# =====
# version number: 6.200 (Linux)
# compiled: 11/27/2014
# compiler version: Intel 1400 20140120
# executable architecture: x64
# Thermo-Calc coupling: disabled
# OpenMP: disabled
# shell: /bin/tcsh
# ('double precision' binary)
# permanent license
#
#
# Language settings
# =====
# Please select a language: 'English', 'Deutsch' or 'Francais'
English
#
#
# Flags and settings
# =====
#
# Geometry
# -----
# Grid size?
# (for 2D calculations: CellsY=1, for 1D calculations: CellsX=1, CellsY=1)
# Cells in X-direction (CellsX):
850
# Cells in Y-direction (CellsY):
1
# Cells in Z-direction (CellsZ):
850
# Cell dimension (grid spacing in micrometers):
# (optionally followed by rescaling factor for the output in the form of '3/4')
1.0
#
# Flags
# -----
# Type of coupling?
# Options: phase concentration temperature temp_cyl_coord
# [stress] [stress_coupled] [flow] [flow_coarse] [dislocation]
phase
# Type of potential?
# Options: double_obstacle multi_obstacle [fd_correction]
multi_obstacle fd_correction
#
# Phase field data structure
# -----
# Coefficient for initial dimension of field iFace
# [minimum usage] [target usage]
0.1
# Coefficient for initial dimension of field nTupel
# [minimum usage] [target usage]
0.1
#
#
# Restart options
# =====
# Restart using old results?
# Options: new restart [reset_time | structure_only]
restart reset_time
```

```

# Name of restart file?
2D_AA_20%
#
#
# Name of output files
# =====
# Name of result files?
2D_AA_20%
# Overwrite files with the same name?
# Options:      overwrite      write_protected      append
#               [zipped|not_zipped|vtk]
#               [unix|windows|non_native]
append
#
#
# Selection of the outputs
# =====
# [legacy|verbose|terse]
# Restart data output?          ('rest')
# Options:      out_restart      no_out_restart      [wallclock time, h.]
out_restart
# Grain number output?          ('korn')
# Options:      out_grains      no_out_grains
out_grains
# Phase number output?          ('phas')
# Options:      out_phases      no_out_phases      [no_interfaces]
out_phases
# Fraction output?              ('frac')
# Options:      out_fraction      no_out_fraction      [phase number]
out_fraction
# Average fraction table?        ('TabF')
# Options:      tab_fractions      no_tab_fractions      [front_temp] [TabL_steps]
tab_fractions
# Interface output?              ('intf')
# Options:      out_interface      no_out_interface      [sharp]
out_interface
# Driving-force output?          ('driv')
# Options:      out_driv_force      no_out_driv_force
out_driv_force
# Interface mobility output?      ('mues')
# Options:      out_mobility      no_out_mobility
out_mobility
# Curvature output?              ('krum')
# Options:      out_curvature      no_out_curvature
out_curvature
# Interface velocity output?      ('vel')
# Options:      out_velocity      no_out_velocity
out_velocity
# Should the grain-time file be written out? ('TabK')
# Options:      tab_grains      no_tab_grains      [extra|standard]
tab_grains
# Should the 'von Neumann Mullins' output be written out? ('TabN')
# Options:      tab_vnm      no_tab_vnm
tab_vnm
# Should the 'grain data output' be written out? ('TabGD')
# Options:      tab_grain_data      no_tab_grain_data
tab_grain_data
# Temperature output?            ('temp')
# Options:      out_temp      no_out_temp
no_out_temp
# Recrystallisation energy output? ('rex')
# Options:      out_recrySTALL      no_out_recrySTALL
no_out_recrySTALL
# Recrystallised fraction output? ('TabR')
# Options:      tab_recrySTALL      no_tab_recrySTALL
no_tab_recrySTALL
# Dislocation density output?      ('rhoD')
# Options:      out_disloc      no_out_disloc
no_out_disloc

```

```

# Miller-Indices output?                                ('mill')
# Options:      out_miller      no_out_miller
no_out_miller
# Orientation output?                                  ('orie')
# Options:      out_orientation no_out_orientation
out_orientation
# Should the orientation-time file be written?         ('Tab0')
# Options:      tab_orientation no_tab_orientation    [rotmat]
tab_orientation
# Should monitoring outputs be written out?           ('TabL')
# Options:      tab_log [simulation time, s] [wallclock time, min] no_tab_log
tab_log 0.25
#
#
# Time input data
# =====
# Finish input of output times (in seconds) with 'end_of_simulation'
# 'regularly-spaced' outputs can be set with 'linear_step'
# or 'logarithmic_step' and then specifying the increment
# and end value
# ('automatic_outputs' optionally followed by the number
# of outputs can be used in conjunction with 'linear_from_file')
# 'first'          : additional output for first time-step
# 'end_at_temperature' : additional output and end of simulation
#                   at given temperature
linear_step 5.0 200.0
end_of_simulation
# Time-step?
# Options:      fix ...[s]      automatic      automatic_limited
automatic
# Coefficient for phase-field criterion 1.00
# Number of steps to adjust profiles of initially sharp interfaces [exclude_inactive]?
8
#
#
# Phase data
# =====
# Number of distinct solid phases?
2
#
# Data for phase 1:
# -----
# Simulation of recrystallisation in phase 1?
# Options:      recrystall      no_recrystall    [verbose|no_verbose]
no_recrystall
# Is phase 1 anisotropic?
# Options:      isotropic      anisotropic      faceted      antifaceted
anisotropic
# Crystal symmetry of the phase?
# Options:      none cubic hexagonal tetragonal orthorhombic
cubic
# Should grains of phase 1 be reduced to categories?
# Options:      categorize no_categorize
no_categorize
#
# Data for phase 2:
# -----
# [identical phase number]
# Simulation of recrystallisation in phase 2?
# Options:      recrystall      no_recrystall    [verbose|no_verbose]
no_recrystall
# Is phase 2 anisotropic?
# Options:      isotropic      anisotropic      faceted      antifaceted
anisotropic
# Crystal symmetry of the phase?
# Options:      none cubic hexagonal tetragonal orthorhombic
cubic
# Should grains of phase 2 be reduced to categories?
# Options:      categorize no_categorize

```

```

no_categorize
#
# Orientation
# -----
# How shall grain orientations be defined?
# Options: angle_2d euler_zxz angle_axis miller_indices quaternion
euler_zxz
#
#
# Grain input
# =====
# Type of grain positioning?
# Options: deterministic random [deterministic_infile] from_file
random
# Integer for randomization?
125
# Number of different types of grains?
2
# Number of grains of type 1?
360
# Number of grains of type 2?
1440
# Input for grain type 1
# -----
# Geometry of grain type 1
# Options: round rectangular elliptic
round
# Minimal value of x-coordinates? [micrometers]
0.00000
# Maximal value of x-coordinates? [micrometers]
850.000
# Minimal value of z-coordinates? [micrometers]
0.00000
# Maximal value of z-coordinates? [micrometers]
850.000
# Minimum grain radius? [micrometers]
29.2800
# Maximum grain radius? [micrometers]
29.2800
# Shall grain type 1 be stabilized or shall
# an analytical curvature description be applied?
# Options: stabilisation analytical_curvature
stabilisation
# Should the Voronoi criterion for grains of type 1 be applied?
# Options: voronoi no_voronoi
voronoi
# Phase number for grain type 1? (int)
1
# Determination of grain orientations?
# Options: random fix fix_direction
random
# Minimal distance between grains (real) [micrometers]?
38.50
# Input for grain type 2
# -----
# Geometry of grain type 2
# Options: round rectangular elliptic
round
# Minimal value of x-coordinates? [micrometers]
0.00000
# Maximal value of x-coordinates? [micrometers]
850.000
# Minimal value of z-coordinates? [micrometers]
0.00000
# Maximal value of z-coordinates? [micrometers]
850.000
# Minimum grain radius? [micrometers]
24.0000
# Maximum grain radius? [micrometers]

```

```

24.0000
# Shall grain type 2 be stabilized or shall
# an analytical curvature description be applied?
# Options:  stabilisation  analytical_curvature
stabilisation
# Should the Voronoi criterion for grains of type 2 be applied?
# Options:  voronoi  no_voronoi
voronoi
# Phase number for grain type 2? (int)
2
# Determination of grain orientations?
# Options:  random  fix  fix_direction
random
# Minimal distance between grains (real) [micrometers]?
18.50
#
#
# Data for further nucleation
# =====
# Enable further nucleation?
# Options:  nucleation  nucleation_symm  no_nucleation  [verbose|no_verbose]
no_nucleation
#
#
# Phase interaction data
# =====
#
# Data for phase interaction 0 / 1:
# -----
# Simulation of interaction between phase 0 and 1?
# Options: phase_interaction  no_phase_interaction
# [standard|particle_pinning[_temperature]|solute_drag]
# |[no_junction_force|junction_force]
no_phase_interaction
#
# Data for phase interaction 0 / 2:
# -----
# Simulation of interaction between phase 0 and 2?
# Options: phase_interaction  no_phase_interaction  identical_phases_nb
# [standard|particle_pinning[_temperature]|solute_drag]
# |[no_junction_force|junction_force]
no_phase_interaction
#
# Data for phase interaction 1 / 1:
# -----
# Simulation of interaction between phase 1 and 1?
# Options: phase_interaction  no_phase_interaction  identical_phases_nb
# [standard|particle_pinning[_temperature]|solute_drag]
# |[no_junction_force|junction_force]
phase_interaction
# Type of surface energy definition between phases 1 and 1?
# Options:  constant  temp_dependent
constant
# Surface energy between phases 1 and 1? [J/cm**2]
# [max. value for num. interface stabilisation [J/cm**2]]
1.00E-5
# Type of mobility definition between phases 1 and 1?
# Options: constant temp_dependent dg_dependent thin_interface_correction
[fixed_minimum]
constant thin_interface_correction
# Kinetic coefficient mu between phases 1 and 1 [ min. value ] [cm**4/(Js)] ?
5.0E-1
# Shall misorientation be considered?
# Options:  misorientation  no_misorientation [transition LAB/HAB in degree]
misorientation
# Input of the misorientation coefficients:
# Modification of surface energy for low angle boundaries
# Options:  factor  Read-Shockley
factor

```

```

# prefactor of surface energy:
1.0000
# Modification of the mobility for low angle boundaries
# Options: factor Humphreys [min_reduction + parameters B and N (default: min_red=0.
B=5.0 N=4.0)]
factor
# prefactor of the mobility for low angle boundaries
1.0000
#
# Data for phase interaction 1 / 2:
# -----
# Simulation of interaction between phase 1 and 2?
# Options: phase_interaction no_phase_interaction identical phases nb
# [standard|particle_pinning[_temperature]|solute_drag]
# | [no_junction_force|junction_force]
phase_interaction
# Type of surface energy definition between phases 1 and 2?
# Options: constant temp_dependent
constant
# Surface energy between phases 1 and 2? [J/cm**2]
# [max. value for num. interface stabilisation [J/cm**2]]
1.00E-5
# Type of mobility definition between phases 1 and 2?
# Options: constant temp_dependent dg_dependent thin_interface_correction
[fixed_minimum]
constant thin_interface_correction
# Kinetic coefficient mu between phases 1 and 2 [ min. value ] [cm**4/(Js)] ?
5.0E-3
# Shall misorientation be considered?
# Options: misorientation no_misorientation [transition LAB/HAB in degree]
misorientation
# Input of the misorientation coefficients:
# Modification of surface energy for low angle boundaries
# Options: factor Read-Shockley
factor
# prefactor of surface energy:
1.0000
# Modification of the mobility for low angle boundaries
# Options: factor Humphreys [min_reduction + parameters B and N (default: min_red=0.
B=5.0 N=4.0)]
factor
# prefactor of the mobility for low angle boundaries
1.0000
# Is interaction isotropic?
# Optionen: isotropic anisotropic [harmonic_expansion]
isotropic
#
# Data for phase interaction 2 / 2:
# -----
# Simulation of interaction between phase 2 and 2?
# Options: phase_interaction no_phase_interaction identical phases nb
# [standard|particle_pinning[_temperature]|solute_drag]
# | [no_junction_force|junction_force]
phase_interaction
# Type of surface energy definition between phases 2 and 2?
# Options: constant temp_dependent
constant
# Surface energy between phases 2 and 2? [J/cm**2]
# [max. value for num. interface stabilisation [J/cm**2]]
1.00E-5
# Type of mobility definition between phases 2 and 2?
# Options: constant temp_dependent dg_dependent thin_interface_correction
[fixed_minimum]
constant thin_interface_correction
# Kinetic coefficient mu between phases 2 and 2 [ min. value ] [cm**4/(Js)] ?
5.0E-3
# Shall misorientation be considered?
# Options: misorientation no_misorientation [transition LAB/HAB in degree]
misorientation

```

```

# Input of the misorientation coefficients:
# Modification of surface energy for low angle boundaries
# Options: factor Read-Shockley
factor
# prefactor of surface energy:
1.0000
# Modification of the mobility for low angle boundaries
# Options: factor Humphreys [min_reduction + parameters B and N (default: min_red=0.
B=5.0 N=4.0)]
factor
# prefactor of the mobility for low angle boundaries
1.0000
#
#
# Phase diagram - input data
# =====
# Equilibrium temperature [K] between 1 and 2
1000.000000000000
# Entropy of fusion between phase 1 and 2 ? [J/(cm**3 K)]
1.0000000000000000E-007
#
#
# Boundary conditions
# =====
# Type of temperature trend?
# Options: linear linear_from_file profiles_from_file
linear
# Number of connecting points? (integer)
0
# Initial temperature at the bottom? (real) [K]
1000.000
# Temperature gradient in z-direction? [K/cm]
0.0000
# Cooling rate? [K/s]
0.0000
# Moving-frame system in z-direction?
# Options: moving_frame no_moving_frame
no_moving_frame
#
# Boundary conditions for phase field in each direction
# Options: i (insulation) s (symmetric) p (periodic/wrap-around)
# g (gradient) f (fixed) w (wetting)
# Sequence: w E (S N, if 3D) B T borders
pppp
# Unit-cell model symmetric with respect to the x/y diagonal plane?
# Options: unit_cell_symm no_unit_cell_symm
no_unit_cell_symm
#
#
# Other numerical parameters
# =====
# Phase minimum?
1.0E-4
# Interface thickness (in cells)?
4.00
#
#
# Number of parallel threads?
# =====
1
# Number of parallel threads: 1
#
#

```

### A.3 Input script of two texture components approach with A-B boundary fast

```
#
# Automatic 'Driving File' written out by MICRESS.
#
#
# MICRESS binary
# =====
# version number: 6.200 (Linux)
# compiled: 11/27/2014
# compiler version: Intel 1400 20140120
# executable architecture: x64
# Thermo-Calc coupling: disabled
# OpenMP: enabled
# shell: /bin/tcsh
# ('double precision' binary)
# permanent license
#
#
# Language settings
# =====
# Please select a language: 'English', 'Deutsch' or 'Francais'
English
#
#
# Flags and settings
# =====
#
# Geometry
# -----
# Grid size?
# (for 2D calculations: CellsY=1, for 1D calculations: CellsX=1, CellsY=1)
# Cells in X-direction (CellsX):
850
# Cells in Y-direction (CellsY):
1
# Cells in Z-direction (CellsZ):
850
# Cell dimension (grid spacing in micrometers):
# (optionally followed by rescaling factor for the output in the form of '3/4')
1.0
#
# Flags
# -----
# Type of coupling?
# Options: phase concentration temperature temp_cyl_coord
# [stress] [stress_coupled] [flow] [flow_coarse] [dislocation]
phase
# Type of potential?
# Options: double_obstacle multi_obstacle [fd_correction]
multi_obstacle fd_correction
#
# Phase field data structure
# -----
# Coefficient for initial dimension of field iFace
# [minimum usage] [target usage]
0.1
# Coefficient for initial dimension of field nTupel
# [minimum usage] [target usage]
0.1
#
#
# Restart options
# =====
# Restart using old results?
# Options: new restart [reset_time | structure_only]
restart reset_time
```

```

#
# Name of restart file?
ABfast_2%
#
# Name of output files
# =====
# Name of result files?
ABfast_2%
#
# Overwrite files with the same name?
# Options:      overwrite      write_protected      append
#              [zipped|not_zipped|vtk]
#              [unix|windows|non_native]
append
#
#
# Selection of the outputs
# =====
# [legacy|verbose|terse]
# Restart data output?                                ('rest')
# Options:      out_restart      no_out_restart      [wallclock time, h.]
out_restart
# Grain number output?                                ('korn')
# Options:      out_grains      no_out_grains
out_grains
# Phase number output?                                ('phas')
# Options:      out_phases      no_out_phases      [no_interfaces]
out_phases
# Fraction output?                                    ('frac')
# Options:      out_fraction      no_out_fraction      [phase number]
out_fraction
# Average fraction table?                              ('TabF')
# Options:      tab_fractions      no_tab_fractions      [front_temp] [TabL_steps]
tab_fractions
# Interface output?                                    ('intf')
# Options:      out_interface      no_out_interface      [sharp]
out_interface
# Driving-force output?                                ('driv')
# Options:      out_driv_force      no_out_driv_force
out_driv_force
# Interface mobility output?                            ('mues')
# Options:      out_mobility      no_out_mobility
out_mobility
# Curvature output?                                    ('krum')
# Options:      out_curvature      no_out_curvature
out_curvature
# Interface velocity output?                            ('vel')
# Options:      out_velocity      no_out_velocity
no_out_velocity
# Should the grain-time file be written out?          ('TabK')
# Options:      tab_grains      no_tab_grains      [extra|standard]
tab_grains
# Should the 'von Neumann Mullins' output be written out? ('TabN')
# Options:      tab_vnm      no_tab_vnm
tab_vnm
# Should the 'grain data output' be written out?      ('TabGD')
# Options:      tab_grain_data      no_tab_grain_data
tab_grain_data
# Temperature output?                                  ('temp')
# Options:      out_temp      no_out_temp
no_out_temp
# Recrystallisation energy output?                    ('rex')
# Options:      out_recrySTALL      no_out_recrySTALL
no_out_recrySTALL
# Recrystallised fraction output?                    ('TabR')
# Options:      tab_recrySTALL      no_tab_recrySTALL
no_tab_recrySTALL
# Dislocation density output?                        ('rhoD')
# Options:      out_disloc      no_out_disloc

```

```

no_out_disloc
# Miller-Indices output? ('mill')
# Options: out_miller no_out_miller
no_out_miller
# Orientation output? ('orie')
# Options: out_orientation no_out_orientation
out_orientation
# Should the orientation-time file be written? ('Tab0')
# Options: tab_orientation no_tab_orientation [rotmat]
tab_orientation
# Should monitoring outputs be written out? ('TabL')
# Options: tab_log [simulation time, s] [wallclock time, min] no_tab_log
tab_log 0.25
#
#
# Time input data
# =====
# Finish input of output times (in seconds) with 'end_of_simulation'
# 'regularly-spaced' outputs can be set with 'linear_step'
# or 'logarithmic_step' and then specifying the increment
# and end value
# ('automatic_outputs' optionally followed by the number
# of outputs can be used in conjunction with 'linear_from_file')
# 'first' : additional output for first time-step
# 'end_at_temperature' : additional output and end of simulation
# at given temperature
linear_step 1.0 150.0
end_of_simulation
# Time-step?
# Options: fix ...[s] automatic automatic_limited
automatic
# Coefficient for phase-field criterion 1.00
# Number of steps to adjust profiles of initially sharp interfaces [exclude_inactive]?
8
#
#
# Phase data
# =====
# Number of distinct solid phases?
2
#
# Data for phase 1:
# -----
# Simulation of recrystallisation in phase 1?
# Options: recrystall no_recrystall [verbose|no_verbose]
no_recrystall
# Is phase 1 anisotropic?
# Options: isotropic anisotropic faceted antifaceted
anisotropic
# Crystal symmetry of the phase?
# Options: none cubic hexagonal tetragonal orthorhombic
cubic
# Should grains of phase 1 be reduced to categories?
# Options: categorize no_categorize
no_categorize
#
# Data for phase 2:
# -----
# [identical phase number]
# Simulation of recrystallisation in phase 2?
# Options: recrystall no_recrystall [verbose|no_verbose]
no_recrystall
# Is phase 2 anisotropic?
# Options: isotropic anisotropic faceted antifaceted
anisotropic
# Crystal symmetry of the phase?
# Options: none cubic hexagonal tetragonal orthorhombic
cubic
# Should grains of phase 2 be reduced to categories?

```

```

# Options:  categorize no_categorize
no_categorize
#
# Orientation
# -----
# How shall grain orientations be defined?
# Options: angle_2d euler_zxz angle_axis miller_indices quaternion
euler_zxz
#
# Grain input
# =====
# Type of grain positioning?
# Options: deterministic random [deterministic_infile] from_file
random
# Integer for randomization?
1
# Number of different types of grains?
2
# Number of grains of type 1?
36
# Number of grains of type 2?
1764
# Input for grain type 1
# -----
# Geometry of grain type 1
# Options: round rectangular elliptic
round
# Minimal value of x-coordinates? [micrometers]
0.00000
# Maximal value of x-coordinates? [micrometers]
850.000
# Minimal value of z-coordinates? [micrometers]
0.00000
# Maximal value of z-coordinates? [micrometers]
850.000
# Minimum grain radius? [micrometers]
26.6000
# Maximum grain radius? [micrometers]
26.6000
# Shall grain type 1 be stabilized or shall
# an analytical curvature description be applied?
# Options: stabilisation analytical_curvature
stabilisation
# Should the Voronoi criterion for grains of type 1 be applied?
# Options: voronoi no_voronoi
voronoi
# Phase number for grain type 1? (int)
1
# Determination of grain orientations?
# Options: random fix fix_direction
random
# Minimal distance between grains (real) [micrometers]?
100.00
# Input for grain type 2
# -----
# Geometry of grain type 2
# Options: round rectangular elliptic
round
# Minimal value of x-coordinates? [micrometers]
0.00000
# Maximal value of x-coordinates? [micrometers]
850.000
# Minimal value of z-coordinates? [micrometers]
0.00000
# Maximal value of z-coordinates? [micrometers]
850.000
# Minimum grain radius? [micrometers]
20.0000

```

```

# Maximum grain radius? [micrometers]
20.0000
# Shall grain type 2 be stabilized or shall
# an analytical curvature description be applied?
# Options:  stabilisation  analytical_curvature
stabilisation
# Should the Voronoi criterion for grains of type 2 be applied?
# Options:  voronoi  no_voronoi
voronoi
# Phase number for grain type 2? (int)
2
# Determination of grain orientations?
# Options:  random  fix  fix_direction
random
# Minimal distance between grains (real) [micrometers]?
16.600
#
#
# Data for further nucleation
# =====
# Enable further nucleation?
# Options:  nucleation  nucleation_symm  no_nucleation  [verbose|no_verbose]
no_nucleation
#
#
# Phase interaction data
# =====
#
# Data for phase interaction 0 / 1:
# -----
# Simulation of interaction between phase 0 and 1?
# Options: phase_interaction  no_phase_interaction
# [standard|particle_pinning[_temperature]|solute_drag]
# |[no_junction_force|junction_force]
no_phase_interaction
#
# Data for phase interaction 0 / 2:
# -----
# Simulation of interaction between phase 0 and 2?
# Options: phase_interaction  no_phase_interaction  identical phases nb
# [standard|particle_pinning[_temperature]|solute_drag]
# |[no_junction_force|junction_force]
no_phase_interaction
#
# Data for phase interaction 1 / 1:
# -----
# Simulation of interaction between phase 1 and 1?
# Options: phase_interaction  no_phase_interaction  identical phases nb
# [standard|particle_pinning[_temperature]|solute_drag]
# |[no_junction_force|junction_force]
phase_interaction
# Type of surface energy definition between phases 1 and 1?
# Options:  constant  temp_dependent
constant
# Surface energy between phases 1 and 1? [J/cm**2]
# [max. value for num. interface stabilisation [J/cm**2]]
1.00E-5
# Type of mobility definition between phases 1 and 1?
# Options: constant temp_dependent dg_dependent thin_interface_correction
[fixed_minimum]
constant thin_interface_correction
# Kinetic coefficient mu between phases 1 and 1 [ min. value ] [cm**4/(Js)] ?
5.0E-5
# Shall misorientation be considered?
# Options:  misorientation  no_misorientation [transition LAB/HAB in degree]
misorientation
# Input of the misorientation coefficients:
# Modification of surface energy for low angle boundaries
# Options:  factor  Read-Shockley

```

```

factor
# prefactor of surface energy:
1.0000
# Modification of the mobility for low angle boundaries
# Options: factor Humphreys [min_reduction + parameters B and N (default: min_red=0.
B=5.0 N=4.0)]
factor
# prefactor of the mobility for low angle boundaries
1.0000
#
# Data for phase interaction 1 / 2:
# -----
# Simulation of interaction between phase 1 and 2?
# Options: phase_interaction no_phase_interaction identical phases nb
# [standard|particle_pinning[_temperature]|solute_drag]
# |[no_junction_force|junction_force]
phase_interaction
# Type of surface energy definition between phases 1 and 2?
# Options: constant temp_dependent
constant
# Surface energy between phases 1 and 2? [J/cm**2]
# [max. value for num. interface stabilisation [J/cm**2]]
1.00E-5
# Type of mobility definition between phases 1 and 2?
# Options: constant temp_dependent dg_dependent thin_interface_correction
[fixed_minimum]
constant thin_interface_correction
# Kinetic coefficient mu between phases 1 and 2 [ min. value ] [cm**4/(Js)] ?
5.0E-2
# Shall misorientation be considered?
# Options: misorientation no_misorientation [transition LAB/HAB in degree]
misorientation
# Input of the misorientation coefficients:
# Modification of surface energy for low angle boundaries
# Options: factor Read-Shockley
factor
# prefactor of surface energy:
1.0000
# Modification of the mobility for low angle boundaries
# Options: factor Humphreys [min_reduction + parameters B and N (default: min_red=0.
B=5.0 N=4.0)]
factor
# prefactor of the mobility for low angle boundaries
1.0000
# Is interaction isotropic?
# Optionen: isotropic anisotropic [harmonic_expansion]
isotropic
#
# Data for phase interaction 2 / 2:
# -----
# Simulation of interaction between phase 2 and 2?
# Options: phase_interaction no_phase_interaction identical phases nb
# [standard|particle_pinning[_temperature]|solute_drag]
# |[no_junction_force|junction_force]
phase_interaction
# Type of surface energy definition between phases 2 and 2?
# Options: constant temp_dependent
constant
# Surface energy between phases 2 and 2? [J/cm**2]
# [max. value for num. interface stabilisation [J/cm**2]]
1.00E-5
# Type of mobility definition between phases 2 and 2?
# Options: constant temp_dependent dg_dependent thin_interface_correction
[fixed_minimum]
constant thin_interface_correction
# Kinetic coefficient mu between phases 2 and 2 [ min. value ] [cm**4/(Js)] ?
5.0E-5
# Shall misorientation be considered?
# Options: misorientation no_misorientation [transition LAB/HAB in degree]

```

```

misorientation
# Input of the misorientation coefficients:
# Modification of surface energy for low angle boundaries
# Options: factor Read-Shockley
factor
# prefactor of surface energy:
1.0000
# Modification of the mobility for low angle boundaries
# Options: factor Humphreys [min_reduction + parameters B and N (default: min_red=0.
B=5.0 N=4.0)]
factor
# prefactor of the mobility for low angle boundaries
1.0000
#
#
# Phase diagram - input data
# =====
# Equilibrium temperature [K] between 1 and 2
1000.000000000000
# Entropy of fusion between phase 1 and 2 ? [J/(cm**3 K)]
1.0000000000000000E-007
#
#
# Boundary conditions
# =====
# Type of temperature trend?
# Options: linear linear_from_file profiles_from_file
linear
# Number of connecting points? (integer)
0
# Initial temperature at the bottom? (real) [K]
1000.000
# Temperature gradient in z-direction? [K/cm]
0.0000
# Cooling rate? [K/s]
0.0000
# Moving-frame system in z-direction?
# Options: moving_frame no_moving_frame
no_moving_frame
#
# Boundary conditions for phase field in each direction
# Options: i (insulation) s (symmetric) p (periodic/wrap-around)
# g (gradient) f (fixed) w (wetting)
# Sequence: w E (S N, if 3D) B T borders
pppp
# Unit-cell model symmetric with respect to the x/y diagonal plane?
# Options: unit_cell_symm no_unit_cell_symm
no_unit_cell_symm
#
#
# Other numerical parameters
# =====
# Phase minimum?
1.00E-4
# Interface thickness (in cells)?
4.00
#
#
#
# Number of parallel threads?
# =====
1
# Number of parallel threads: 1
#

```

## A.4 Input script of three texture component approach

```
#
# Automatic 'Driving File' written out by MICRESS.
#
#
# MICRESS binary
# =====
# version number: 6.200 (Linux)
# compiled: 11/27/2014
# compiler version: Intel 1400 20140120
# executable architecture: x64
# Thermo-Calc coupling: disabled
# OpenMP: enabled
# shell: /bin/tcsh
# ('double precision' binary)
# permanent license
#
#
# Language settings
# =====
# Please select a language: 'English', 'Deutsch' or 'Francais'
English
#
#
# Flags and settings
# =====
#
# Geometry
# -----
# Grid size?
# (for 2D calculations: CellsY=1, for 1D calculations: CellsX=1, CellsY=1)
# Cells in X-direction (CellsX):
300
# Cells in Y-direction (CellsY):
1
# Cells in Z-direction (CellsZ):
300
# Cell dimension (grid spacing in micrometers):
# (optionally followed by rescaling factor for the output in the form of '3/4')
1.0
#
# Flags
# -----
# Type of coupling?
# Options: phase concentration temperature temp_cyl_coord
# [stress] [stress_coupled] [flow] [flow_coarse] [dislocation]
phase
# Type of potential?
# Options: double_obstacle multi_obstacle [fd_correction]
multi_obstacle fd_correction
#
# Phase field data structure
# -----
# Coefficient for initial dimension of field iFace
# [minimum usage] [target usage]
0.1
# Coefficient for initial dimension of field nTupel
# [minimum usage] [target usage]
0.1
#
#
# Restart options
# =====
# Restart using old results?
# Options: new restart [reset_time | structure_only]
```

```

restart
# Name of restart file?
ABC_50%
#
#
# Name of output files
# =====
# Name of result files?
ABC_50%
# Overwrite files with the same name?
# Options:      overwrite      write_protected      append
#               [zipped|not_zipped|vtk]
#               [unix|windows|non_native]
append
#
#
# Selection of the outputs
# =====
# [legacy|verbose|terse]
# Restart data output?                ('rest')
# Options:      out_restart          no_out_restart        [wallclock time, h.]
out_restart
# Grain number output?                ('korn')
# Options:      out_grains           no_out_grains
out_grains
# Phase number output?                ('phas')
# Options:      out_phases           no_out_phases         [no_interfaces]
out_phases
# Fraction output?                    ('frac')
# Options:      out_fraction         no_out_fraction      [phase number]
out_fraction
# Average fraction table?              ('TabF')
# Options:      tab_fractions         no_tab_fractions     [front_temp] [TabL_steps]
tab_fractions
# Interface output?                    ('intf')
# Options:      out_interface         no_out_interface     [sharp]
out_interface
# Driving-force output?                ('driv')
# Options:      out_driv_force        no_out_driv_force
out_driv_force
# Interface mobility output?           ('mues')
# Options:      out_mobility          no_out_mobility
out_mobility
# Curvature output?                    ('krum')
# Options:      out_curvature         no_out_curvature
no_out_curvature
# Interface velocity output?           ('vel')
# Options:      out_velocity          no_out_velocity
out_velocity
# Should the grain-time file be written out? ('TabK')
# Options:      tab_grains            no_tab_grains        [extra|standard]
tab_grains
# Should the 'von Neumann Mullins' output be written out? ('TabN')
# Options:      tab_vnm               no_tab_vnm
tab_vnm
# Should the 'grain data output' be written out? ('TabGD')
# Options:      tab_grain_data         no_tab_grain_data
tab_grain_data
# Temperature output?                  ('temp')
# Options:      out_temp              no_out_temp
no_out_temp
# Recrystallisation energy output?     ('rex')
# Options:      out_recrystall         no_out_recrystall
no_out_recrystall
# Recrystallised fraction output?     ('TabR')
# Options:      tab_recrystall         no_tab_recrystall
no_tab_recrystall
# Dislocation density output?         ('rhoD')
# Options:      out_disloc             no_out_disloc

```

```

no_out_disloc
# Miller-Indices output?                                ('mill')
# Options:      out_miller      no_out_miller
no_out_miller
# Orientation output?                                    ('orie')
# Options:      out_orientation no_out_orientation
no_out_orientation
# Should the orientation-time file be written?           ('Tab0')
# Options:      tab_orientation no_tab_orientation      [rotmat]
no_tab_orientation
# Should monitoring outputs be written out?             ('TabL')
# Options:      tab_log [simulation time, s] [wallclock time, min] no_tab_log
tab_log 0.25
#
#
# Time input data
# =====
# Finish input of output times (in seconds) with 'end_of_simulation'
# 'regularly-spaced' outputs can be set with 'linear_step'
# or 'logarithmic_step' and then specifying the increment
# and end value
# ('automatic_outputs' optionally followed by the number
# of outputs can be used in conjunction with 'linear_from_file')
# 'first'           : additional output for first time-step
# 'end_at_temperature' : additional output and end of simulation
#                   at given temperature
linear_step 5.0 600.0
end_of_simulation
# Time-step?
# Options:      fix ...[s]      automatic      automatic_limited
automatic
# Coefficient for phase-field criterion 1.00
# Number of steps to adjust profiles of initially sharp interfaces [exclude_inactive]?
8.0
#
#
# Phase data
# =====
# Number of distinct solid phases?
3
#
# Data for phase 1:
# -----
# Simulation of recrystallisation in phase 1?
# Options:      recrystall      no_recrystall      [verbose|no_verbose]
no_recrystall
# Is phase 1 anisotropic?
# Options:      isotropic      anisotropic      faceted      antifaceted
isotropic
# Should grains of phase 1 be reduced to categories?
# Options:      categorize no_categorize
no_categorize
#
# Data for phase 2:
# -----
# [identical phase number]
# Simulation of recrystallisation in phase 2?
# Options:      recrystall      no_recrystall      [verbose|no_verbose]
no_recrystall
# Is phase 2 anisotropic?
# Options:      isotropic      anisotropic      faceted      antifaceted
isotropic
# Should grains of phase 2 be reduced to categories?
# Options:      categorize no_categorize
no_categorize
#
# Data for phase 3:
# -----
# [identical phase number]

```

```

# Simulation of recrystallisation in phase 3?
# Options:  recrystall    no_recrySTALL    [verbose|no_verbose]
no_recrySTALL
# Is phase 3 anisotrop?
# Options:  isotropic    anisotropic    faceted    antifaceted
isotropic
# Should grains of phase 3 be reduced to categories?
# Options:  categorize    no_categorize
no_categorize
#
#
# Grain input
# =====
# Type of grain positioning?
# Options:  deterministic    random    [deterministic_infile]    from_file
random
# Integer for randomization?
12
# Number of different types of grains?
3
# Number of grains of type 1?
1
# Number of grains of type 2?
60
# Number of grains of type 3?
60
# Input for grain type 1
# -----
# Geometry of grain type 1
# Options:  round    rectangular    elliptic
round
# Minimal value of x-coordinates? [micrometers]
146.000
# Maximal value of x-coordinates? [micrometers]
154.000
# Minimal value of z-coordinates? [micrometers]
146.000
# Maximal value of z-coordinates? [micrometers]
154.000
# Minimum grain radius? [micrometers]
39.0000
# Maximum grain radius? [micrometers]
43.0000
# Shall grain type 1 be stabilized or shall
# an analytical curvature description be applied?
# Options:  stabilisation    analytical_curvature
stabilisation
# Should the Voronoi criterion for grains of type 1 be applied?
# Options:  voronoi    no_voronoi
voronoi
# Phase number for grain type 1? (int)
1
# Input for grain type 2
# -----
# Geometry of grain type 2
# Options:  round    rectangular    elliptic
round
# Minimal value of x-coordinates? [micrometers]
0.00000
# Maximal value of x-coordinates? [micrometers]
300.000
# Minimal value of z-coordinates? [micrometers]
0.00000
# Maximal value of z-coordinates? [micrometers]
300.000
# Minimum grain radius? [micrometers]
30.0000
# Maximum grain radius? [micrometers]
34.0000

```

```

# Shall grain type 2 be stabilized or shall
# an analytical curvature description be applied?
# Options:  stabilisation  analytical_curvature
stabilisation
# Should the Voronoi criterion for grains of type 2 be applied?
# Options:  voronoi  no_voronoi
voronoi
# Phase number for grain type 2? (int)
2
# Minimal distance between grains (real) [micrometers]?
35.000
# Input for grain type 3
# -----
# Geometry of grain type 3
# Options:  round  rectangular  elliptic
round
# Minimal value of x-coordinates? [micrometers]
0.00000
# Maximal value of x-coordinates? [micrometers]
300.000
# Minimal value of z-coordinates? [micrometers]
0.00000
# Maximal value of z-coordinates? [micrometers]
300.000
# Minimum grain radius? [micrometers]
30.1800
# Maximum grain radius? [micrometers]
34.1800
# Shall grain type 3 be stabilized or shall
# an analytical curvature description be applied?
# Options:  stabilisation  analytical_curvature
stabilisation
# Should the Voronoi criterion for grains of type 3 be applied?
# Options:  voronoi  no_voronoi
voronoi
# Phase number for grain type 3? (int)
3
# Minimal distance between grains (real) [micrometers]?
35.000
#
#
# Data for further nucleation
# =====
# Enable further nucleation?
# Options:  nucleation  nucleation_symm  no_nucleation  [verbose|no_verbose]
no_nucleation
#
#
# Phase interaction data
# =====
#
# Data for phase interaction 0 / 1:
# -----
# Simulation of interaction between phase 0 and 1?
# Options:  phase_interaction  no_phase_interaction
# [standard|particle_pinning[_temperature]|solute_drag]
# |[no_junction_force|junction_force]
no_phase_interaction
#
# Data for phase interaction 0 / 2:
# -----
# Simulation of interaction between phase 0 and 2?
# Options:  phase_interaction  no_phase_interaction  identical_phases  nb
# [standard|particle_pinning[_temperature]|solute_drag]
# |[no_junction_force|junction_force]
no_phase_interaction
#
# Data for phase interaction 0 / 3:
# -----

```

```

# Simulation of interaction between phase 0 and 3?
# Options: phase_interaction no_phase_interaction identical phases nb
# [standard|particle_pinning[_temperature]|solute_drag]
# |[no_junction_force|junction_force]
no_phase_interaction
#
# Data for phase interaction 1 / 1:
# -----
# Simulation of interaction between phase 1 and 1?
# Options: phase_interaction no_phase_interaction identical phases nb
# [standard|particle_pinning[_temperature]|solute_drag]
# |[no_junction_force|junction_force]
phase_interaction
# Type of surface energy definition between phases 1 and 1?
# Options: constant temp_dependent
constant
# Surface energy between phases 1 and 1? [J/cm**2]
# [max. value for num. interface stabilisation [J/cm**2]]
1.0E-5
# Type of mobility definition between phases 1 and 1?
# Options: constant temp_dependent dg_dependent thin_interface_correction
[fixed_minimum]
constant thin_interface_correction
# Kinetic coefficient mu between phases 1 and 1 [ min. value ] [cm**4/(Js)] ?
5.0E-3
#
# Data for phase interaction 1 / 2:
# -----
# Simulation of interaction between phase 1 and 2?
# Options: phase_interaction no_phase_interaction identical phases nb
# [standard|particle_pinning[_temperature]|solute_drag]
# |[no_junction_force|junction_force]
phase_interaction
# Type of surface energy definition between phases 1 and 2?
# Options: constant temp_dependent
constant
# Surface energy between phases 1 and 2? [J/cm**2]
# [max. value for num. interface stabilisation [J/cm**2]]
1.0E-5
# Type of mobility definition between phases 1 and 2?
# Options: constant temp_dependent dg_dependent thin_interface_correction
[fixed_minimum]
constant thin_interface_correction
# Kinetic coefficient mu between phases 1 and 2 [ min. value ] [cm**4/(Js)] ?
5.0
#
# Data for phase interaction 1 / 3:
# -----
# Simulation of interaction between phase 1 and 3?
# Options: phase_interaction no_phase_interaction identical phases nb
# [standard|particle_pinning[_temperature]|solute_drag]
# |[no_junction_force|junction_force]
phase_interaction
# Type of surface energy definition between phases 1 and 3?
# Options: constant temp_dependent
constant
# Surface energy between phases 1 and 3? [J/cm**2]
# [max. value for num. interface stabilisation [J/cm**2]]
1.0E-5
# Type of mobility definition between phases 1 and 3?
# Options: constant temp_dependent dg_dependent thin_interface_correction
[fixed_minimum]
constant thin_interface_correction
# Kinetic coefficient mu between phases 1 and 3 [ min. value ] [cm**4/(Js)] ?
5.0E-3
#
# Data for phase interaction 2 / 2:
# -----
# Simulation of interaction between phase 2 and 2?

```

```

# Options: phase_interaction no_phase_interaction identical phases nb
# [standard|particle_pinning[_temperature]|solute_drag]
# | [no_junction_force|junction_force]
phase_interaction
# Type of surface energy definition between phases 2 and 2?
# Options: constant temp_dependent
constant
# Surface energy between phases 2 and 2? [J/cm**2]
# [max. value for num. interface stabilisation [J/cm**2]]
1.0E-5
# Type of mobility definition between phases 2 and 2?
# Options: constant temp_dependent dg_dependent thin_interface_correction
[fixed_minimum]
constant thin_interface_correction
# Kinetic coefficient mu between phases 2 and 2 [ min. value ] [cm**4/(Js)] ?
5.0E-3
#
# Data for phase interaction 2 / 3:
# -----
# Simulation of interaction between phase 2 and 3?
# Options: phase_interaction no_phase_interaction identical phases nb
# [standard|particle_pinning[_temperature]|solute_drag]
# | [no_junction_force|junction_force]
phase_interaction
# Type of surface energy definition between phases 2 and 3?
# Options: constant temp_dependent
constant
# Surface energy between phases 2 and 3? [J/cm**2]
# [max. value for num. interface stabilisation [J/cm**2]]
1.0E-5
# Type of mobility definition between phases 2 and 3?
# Options: constant temp_dependent dg_dependent thin_interface_correction
[fixed_minimum]
constant thin_interface_correction
# Kinetic coefficient mu between phases 2 and 3 [ min. value ] [cm**4/(Js)] ?
5.0E-3
#
# Data for phase interaction 3 / 3:
# -----
# Simulation of interaction between phase 3 and 3?
# Options: phase_interaction no_phase_interaction identical phases nb
# [standard|particle_pinning[_temperature]|solute_drag]
# | [no_junction_force|junction_force]
phase_interaction
# Type of surface energy definition between phases 3 and 3?
# Options: constant temp_dependent
constant
# Surface energy between phases 3 and 3? [J/cm**2]
# [max. value for num. interface stabilisation [J/cm**2]]
1.0E-5
# Type of mobility definition between phases 3 and 3?
# Options: constant temp_dependent dg_dependent thin_interface_correction
[fixed_minimum]
constant thin_interface_correction
# Kinetic coefficient mu between phases 3 and 3 [ min. value ] [cm**4/(Js)] ?
5.0E-3
#
#
# Phase diagram - input data
# =====
# Equilibrium temperature [K] between 1 and 2
1000.000000000000
# Entropy of fusion between phase 1 and 2 ? [J/(cm**3 K)]
1.0000000000000000E-007
# Equilibrium temperature [K] between 1 and 3
1000.000000000000
# Entropy of fusion between phase 1 and 3 ? [J/(cm**3 K)]
1.0000000000000000E-007
# Equilibrium temperature [K] between 2 and 3

```

```

1000.000000000000
# Entropy of fusion between phase 2 and 3 ? [J/(cm**3 K)]
1.000000000000000E-007
#
#
# Boundary conditions
# =====
# Type of temperature trend?
# Options:  linear      linear_from_file      profiles_from_file
linear
# Number of connecting points?      (integer)
0
# Initial temperature at the bottom? (real) [K]
1000.000
# Temperature gradient in z-direction? [K/cm]
0.0000
# Cooling rate? [K/s]
0.0000
# Moving-frame system in z-direction?
# Options:  moving_frame      no_moving_frame
no_moving_frame
#
# Boundary conditions for phase field in each direction
# Options:  i (insulation) s (symmetric) p (periodic/wrap-around)
#           g (gradient)  f (fixed)      w (wetting)
# Sequence: w E (S N, if 3D) B T borders
pppp
# Unit-cell model symmetric with respect to the x/y diagonal plane?
# Options:  unit_cell_symm  no_unit_cell_symm
no_unit_cell_symm
#
#
# Other numerical parameters
# =====
# Phase minimum?
1.0E-4
# Interface thickness (in cells)?
4.00
#
#
# Number of parallel threads?
# =====
1
# Number of parallel threads: 1
#
#

```

## Appendix B

### B.1 Sensitivity analysis of minimal distance between grains

For the construction of the initial grain structure, the minimal distance between grains  $d$  will change accordingly. For instance, when the percentage of B grains changed, the minimal distance between B grains will change correspondingly. This value also changes when the simulation is extended from 2D to 3D. Therefore, whether this value will influence the simulation results is of great importance. Simulations to examine the influence of  $d$  are performed for both the critical disorientation angle scenario and the A-B texture components scenario.

In critical disorientation angle scenario, all grains are positioned in a limited domain area, therefore  $d$  has a maximal value, since it is impossible to put so many grains in a limited domain if the distance between grains is too large. However, if grains are too close to each other, some liquid phase may appear. Therefore,  $d$  has a minimal value. When 1800 grains are placed in an  $800 \times 800$  domain and  $d$  is changing from  $14.0 \mu\text{m}$  to  $15.5 \mu\text{m}$ , the variation of grain area and the grain size distribution is illustrated in Fig B.1 (a) and (b), respectively. When  $d$  is changing between  $14.0 \mu\text{m}$  and  $15.5 \mu\text{m}$  in Fig. B.1(a) the grain area is hardly changed while in Fig. B.1(b) the grain size distributions are almost the same. This means the effect of  $d$  on the microstructure of critical disorientation angle case is not prominent.

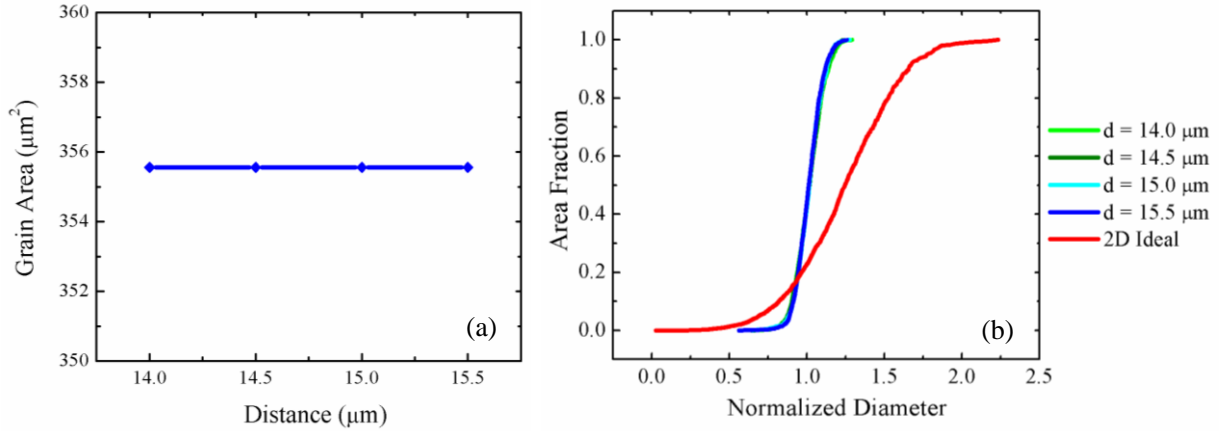


**Figure B.1** (a) Grain area variation; (b) Grain size distribution of disorientation scenario when the minimal distance between grains changing from 14.0μm to 15.5μm

A similar study has been done to explore the influence of minimal distance between grains  $d$  in the two texture components system. When 98% A grains and 2% B grains are in the system, the changeable interval of minimal distance between A grains  $d_A$  is very small. The maximal value of  $d_A$  is 17.3μm while liquid phase appears when  $d_A$  is 16.3μm. Therefore, the attention is given to the influence of minimal distance between B grains  $d_B$ . The maximal value of  $d_B$  is 55.5μm. When  $d_B$  is changing between 45.5μm and 55.5μm, the variation of grain area and grain size distribution is shown in Fig B.2(a) and (b), respectively. As shown in Fig. B.2(a), the grain area of A grains is fluctuating in a small interval while the small fluctuation of B grain area (less than 1%) can be neglected. The curves of grain size distribution almost overlap as shown in Fig. B.2(b). All these prove that the effect of  $d_B$  is not significant.

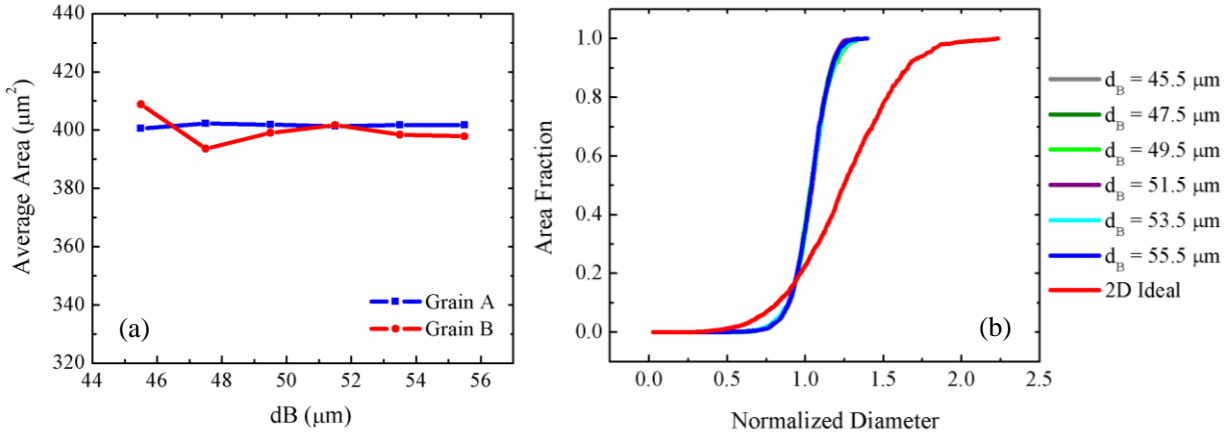


**Figure B.2** (a) Grain area variation; (b) Grain size distribution of two texture components when the minimal distance between grains changing from 45.5 $\mu\text{m}$  to 55.5 $\mu\text{m}$

## B.2 Sensitivity analysis of radius distribution range

When defining the geometry of grains, the maximal grain radius  $r_{max}$  and the minimal grain radius  $r_{min}$  are two important factors. The range of grain radius  $r$  is the difference between  $r_{max}$  and  $r_{min}$ . In critical disorientation angle scenario, there is only one type of grains. A series of simulations are performed with grain radius range  $r$  changing between 0.0 $\mu\text{m}$  and 10.0 $\mu\text{m}$  while all the other simulation settings are the same. As presented in Fig. B.3 (a), the variation of grain area is not significant. From Fig. B.3(b), one can find that the grain size distributions are very close to each other. This means the influence of radius range  $r$  can be neglected in the simulation of critical disorientation angle scenario.

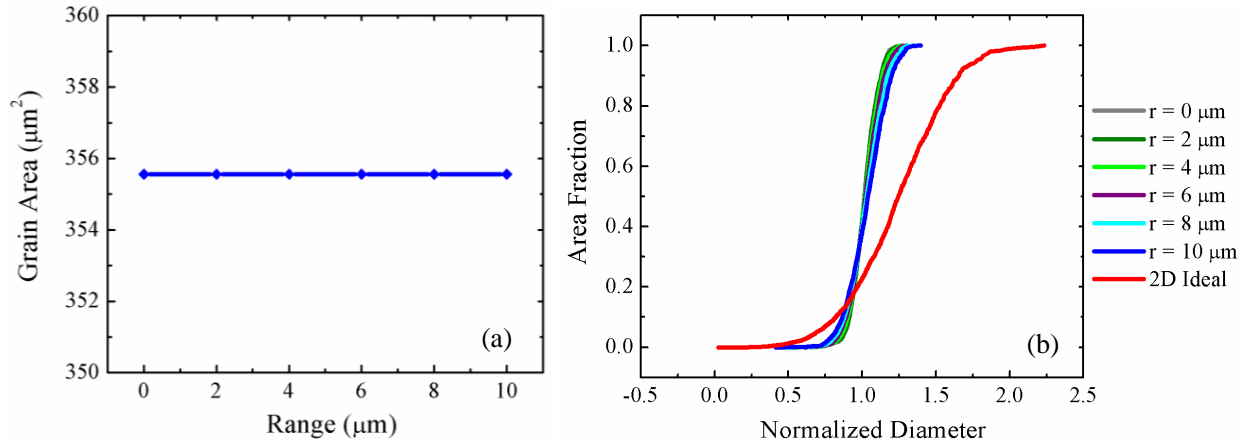


**Figure B.3** (a) Grain area variation; (b) Grain size distribution of disorientation scenario when the radius range changing from 0.0 $\mu\text{m}$  to 10.0 $\mu\text{m}$

A similar parameter study is implemented in the scenario of two texture components. When 98% A grains and 2% B grain are in the system, the maximal and minimal radius of A and B grains are listed in Tab. B.1. The average value of grain radius keeps the same while the radius range is changing between 0.0 $\mu\text{m}$  and 10.0 $\mu\text{m}$ . While keeping all the other simulation settings the same, the result of grain area change is shown in Fig. B.4(a) and there is no significant fluctuation in grain area for both A and B grains. The grain size distribution is shown in Fig. B.4(b) and all distribution curves are close to one another. All these results verify that there is no remarkable consequence of radius range variation in the simulation of two texture components.

**Table B.1** The radius value of grain A and B

Max grain A radius	Min grain A radius / $\mu\text{m}$	Max grain B radius / $\mu\text{m}$	Min grain B radius / $\mu\text{m}$	Range / $\mu\text{m}$
20.0	20.0	25.15	25.15	0.0
21.0	19.0	26.15	24.15	2.0
22.0	18.0	27.15	23.15	4.0
23.0	17.0	28.15	22.15	6.0
24.0	16.0	29.15	21.15	8.0
25.0	15.0	30.15	20.15	10.0

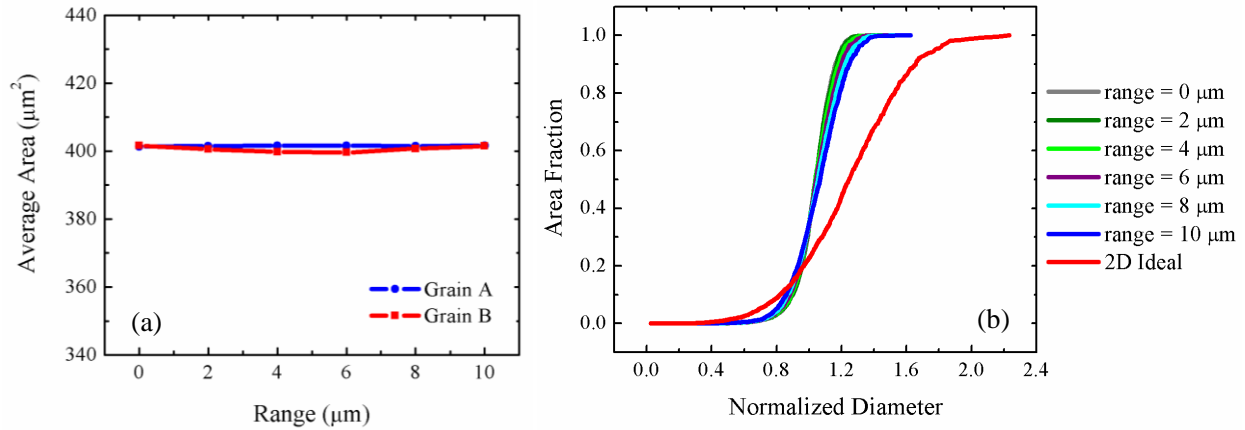


**Figure B.4** (a) Grain area variation; (b) Grain size distribution of two texture components when the radius range changing from 0.0 $\mu\text{m}$  to 10.0 $\mu\text{m}$

### B.3 Sensitivity of the radius ratio $r_A$ vs. $r_B$

When there are two texture components in the system, the output grain size is determined by the  $r_A$  and  $r_B$  values. As shown in Section 4.2.3 when  $r_A = r_B$  (radius ratio  $r_B/r_A = 1$ ) is taken, the B grains are smaller than A grains for small fractions of B grains (e.g. 2%). Again, this appears to be a specific feature of assigning the texture component in the initial microstructure with the MICRESS software. In order to obtain the same grain size for both texture components, a larger  $r_B$  value and a smaller  $r_A$  value ( $r_B/r_A = 1.33$ ) has to be assigned, i.e. there is a significant of the radius ratio ( $r_B/r_A$ ) on the grain size ratio (average B grain area/average A grain area). Fig. B.5 illustrates the variation of grain size ratio due to the change of radius ratio. In Fig. B.5, the radius ratio is roughly inversely proportional to the grain size ratio, and increase the radius ratio is an effective way to reduce the grain size ratio.

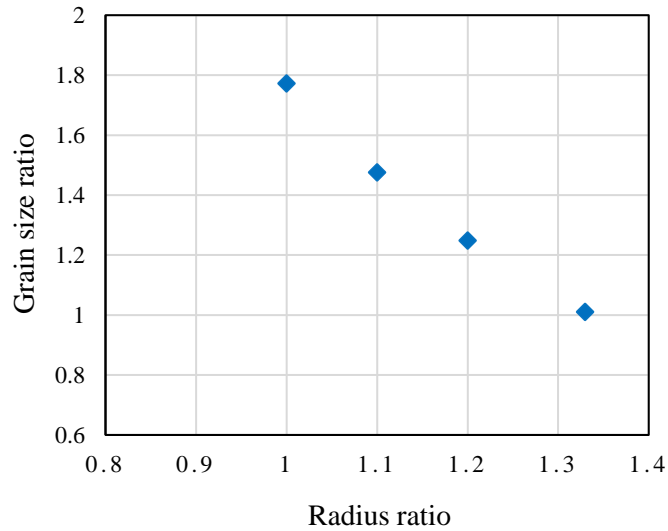


**Figure B.5** The variation of the initial grain size ratio due to the change of the radius ratio for a two texture component system with 2%B grains.

#### **B.4 Sensitivity analysis of initial structure**

In simulations of the critical threshold angle approach (and similarly for the different rain type approaches), all initial structures are obtained from Voronoi tessellation with a very narrow grain size distribution. As illustrated for the ideal grain growth analysis (see Section 4.3.1) this distribution evolves into the much wider scaling grain size distribution with marginal effects on the overall grain growth behavior. It is however, important to test the sensitivity of the selection of the initial microstructures on subsequent grain growth behavior with mobility advantages. Thus, two groups of simulations were conducted starting from different initial structures: one is starting from Voronoi tessellation while the other simulation is starting from a scaling grain size distribution. The latter was obtained from Voronoi tessellation with a subsequent brief grain growth period where all boundaries have the same mobility to attain the scaling distribution. The grain growth simulations with mobility advantage were conducted for a threshold angle of  $40^\circ$  and a mobility ratio of 10. The time evolution of the accumulative grain area distribution curves are

compared in Fig. B.6. For both simulations similar grain size distributions are obtained that are wider than the scaling distribution. Starting from Voronoi tessellation the maximum EQAD is about 3.0 while it is approximately 2.75 when starting from the scaling distribution.

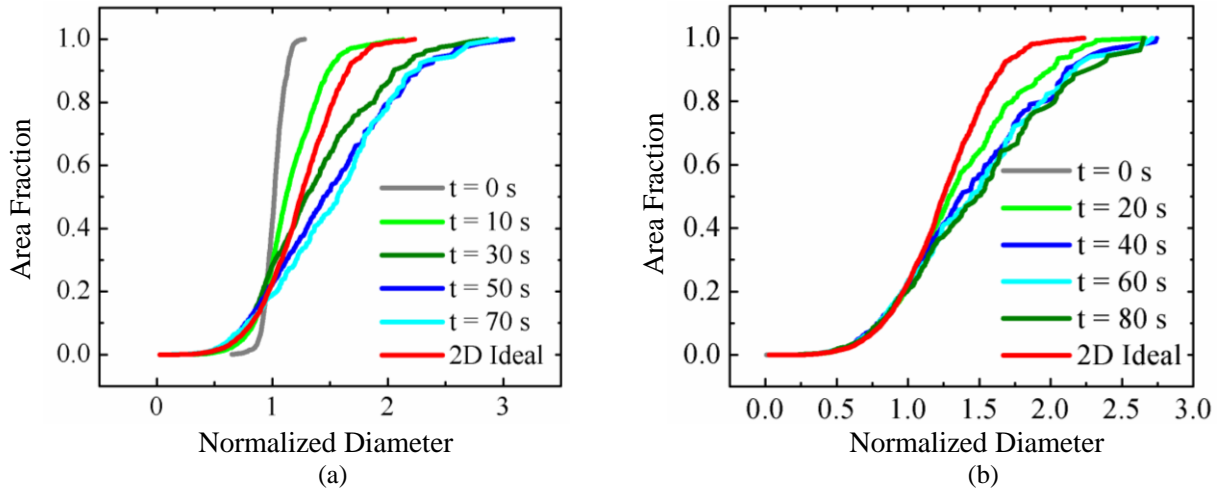


**Figure B.6** Time evolution of cumulative grain size distribution: (a) starting from Voronoi tessellation; (b) starting from scaling distribution.